TKK Dissertations 128
Espoo 2008

FRACTURE MECHANICS AND SUBCRITICAL CRACK GROWTH APPROACH TO MODEL TIME-DEPENDENT FAILURE IN BRITTLE ROCK

Doctoral Dissertation

Mikael Rinne

Helsinki University of Technology
Faculty of Engineering and Architecture
Department of Civil and Environmental Engineering

TKK Dissertations 128
Espoo 2008

FRACTURE MECHANICS AND SUBCRITICAL CRACK GROWTH APPROACH TO MODEL TIME-DEPENDENT FAILURE IN BRITTLE ROCK

Doctoral Dissertation

Mikael Rinne

Dissertation for the degree of Doctor of Science in Technology to be presented with due permission of the Faculty of Engineering and Architecture for public examination and debate in Auditorium V1 at Helsinki University of Technology (Espoo, Finland) on the 7th of August, 2008, at 12 noon.

Helsinki University of Technology
Faculty of Engineering and Architecture
Department of Civil and Environmental Engineering

Teknillinen korkeakoulu
Insinööritieteiden ja arkkitehtuurin tiedekunta
Yhdyskunta- ja ympäristötekniikan laitos

Distribution:
Helsinki University of Technology
Faculty of Engineering and Architecture
Department of Civil and Environmental Engineering
P.O. Box 6200 (Vuorimiehentie 2)
FI - 02015 TKK
FINLAND
URL: http://www.tkk.fi/Yksikot/Rakennus/Kallio/
Tel. +358-9-4511
Fax +358-9-451 2812
E-mail: mikael.rinne@fracom.fi

ISBN 978-951-22-9434-3
ISBN 978-951-22-9435-0 (PDF)
ISSN 1795-2239
ISSN 1795-4584 (PDF)
URL: http://lib.tkk.fi/Diss/2008/isbn9789512294350/

TKK-DISS-2490

Picaset Oy
Helsinki 2008

ABSTRACT OF DOCTORAL DISSERTATION

HELSINKI UNIVERSITY OF TECHNOLOGY
P.O. BOX 1000, FI-02015 TKK
http://www.tkk.fi

Author Olli Mikael Rinne

Name of the dissertation
Fracture mechanics and subcritical crack growth approach to model time-dependent failure in brittle rock

Manuscript submitted 12.06.2007
Manuscript revised 26.05.2008
Date of the defence 07.08.2008

(X) Monograph
( ) Article dissertation (summary + original articles)

Faculty Faculty of Engineering and Architecture
Department Department of Civil and Environmental Engineering
Field of research Rock mechanics / Fracture mechanics of brittle rocks
Opponent(s) Prof. Charlie C. Li
Supervisor Prof. Pekka Särkkä

Abstract

Subcritical crack growth (SCG) takes place when a crack is stressed below its short-term strength. This slow fracturing process may lead to an accelerating crack velocity and to a sudden unstable failure event. SCG is thought to play an important role in long-term rock stability at all scales, ranging from laboratory samples to earthquake-generating faults. SCG can be detected as rock loosening or as sudden rock movements around excavations.

A time-dependent crack growth model is developed to evaluate the delayed failure of a loaded rock. It is based on brittle fracture mechanics principles and the theory of subcritical crack growth (stress corrosion). The SCG model was incorporated in the Boundary Element (DDM) software FRACOD. The fracture mechanics code with the SCG model provides a reasonable description of the failure process. New crack formation, slow and fast fracture propagation, stress relaxation and time-dependent failure are considered both in tensional and compressive loading conditions.

For brittle rock material the model suggests that stable wing-crack propagation takes place under an increasing uniaxial load prior to crack coalescence and extensive unstable fracture propagation. The rupture of a rock specimen is dominated by the formation of large shear fractures. Fracture dilation occurs in the late post-peak phase of failure. The modelled post-peak axial stress-strain response of brittle rocks shows Class II behaviour and it is explained by the Griffith locus.

The effect of time on the load-bearing capacity of the Äspö diorite has been investigated in the laboratory by slow-rate loading experiments (SRS tests). Modelled time-dependent failure behaviour agrees well with laboratory findings. The modelling suggests that negligible amounts of SCG are involved in standard uniaxial and triaxial compressive strength tests, while for the SRS tests the time-dependent effects are significant. The modelled long-term load-bearing capacity is not decreased severely when the applied load is below 80% of the short-term peak strength. The confinement increases the required stress/strain level for failure but do not affect the shape of the time-to-failure curve.

Keywords Fracture mechanics, delayed brittle failure, subcritical crack growth, DDM modelling

ISBN 978-951-22-9434-3 (printed)
ISSN 1795-2239 (printed)
ISBN 978-951-22-9435-0 (pdf)
ISSN 1795-4584 (pdf)
Language English
Number of pages 155
Publisher Helsinki University of Technology, Rock Engineering
Print distribution Helsinki University of Technology, Rock Engineering
(X) The dissertation can be read at URL: http://lib.tkk.fi/Diss/2008/isbn9789512294350/

VÄITÖSKIRJAN TIIVISTELMÄ	TEKNILLINEN KORKEAKOULU PL 1000, 02015 TKK http://www.tkk.fi

Tekijä Olli Mikael Rinne

Väitöskirjan nimi

Fracture mechanics and subcritical crack growth approach to model time-dependent failure in brittle rock

Käsikirjoituksen päivämäärä 12.06.2007	Korjatun käsikirjoituksen päivämäärä 26.5.2008

Väitöstilaisuuden ajankohta 07.08.2008

(X) Monografia	( ) Yhdistelmäväitöskirja (yhteenveto + erillisartikkelit)

Tiedekunta	Insinööritieteiden ja arkkitehtuurin tiedekunta
Laitos	Yhdyskunta- ja ympäristötekniikan laitos
Tutkimusala	Kalliomekaniikka / Hauraan materiaalin rakomekaniikka
Vastaväittäjä(t)	Prof. Charlie C. Li
Työn valvoja	Prof. Pekka Särkkä

Tiivistelmä

Kun hauraan materiaalin rakoa kuormitetaan raon lyhytkestoista lujuutta pienemmällä kuormalla, rako kasvaa alikriittisesti. Ajan myötä raon kasvunopeus kiihtyy ja rakoa ympäröivä rakenne saattaa murtua äkillisesti. Kuormitettujen rakojen on todettu kasvavan alikriittisesti laboratorio-olosuhteissa ja hidasta raonkasvua oletetaan tapahtuvan myös maanalaisten tilojen kuormitetuissa kalliorakenteissa ja maankuoren tektonisissa prosesseissa. Alikriittisen raonkasvun seuraukset voivat ilmetä kalliorakenteiden löyhtymisenä, kallioräiskeenä tai maanjäristyksinä.

Tässä väitöstyössä kehitetyllä mallilla arvioidaan raon kasvunopeutta ja viiveellä tapahtuvaa materiaalin murtumista. Malli perustuu rakomekaniikkaan sekä alikriittisen raonkasvun teoriaan (jännityskorroosio). Alikriittinen rakomalli on liitetty kaksiulotteiseen FRACOD-reunaelementtimenetelmään. Mallin avulla kuvataan rakojen syntyä, hidasta ja kiihtyvää raonkasvua, rakoilun aiheuttamaa materiaalin löyhtymistä ja murtumista veto- ja puristusjännitys olosuhteissa.

Laskelmien perusteella hauraan kivimateriaalin rikkoutuminen yksiaksiaalisessa puristusmurtokokeessa alkaa siipirakojen stabiilina kasvuna kohti suurinta pääjännitystä. Kun raot ovat kasvaneet liki suurimman pääjännityksen suuntaiseksi ja rakojen keskinäinen vuorovaikutus on lisääntynyt merkittävästi, kappale murtuu äkillisesti leikkausjännityksen suuntaisesti. Mallin mukaan leikkausraot aukeavat murtumisen loppuvaiheessa. Huippukuorman jälkeinen jännitys-venymäkäyttäytyminen todettiin muistuttavan nk. Class II -tyypin materiaalikäyttäytymistä. Class II käyttäytyminen on perusteltu nk. Griffithin murtokäyrän avulla.

Äspö-dioriitin ajasta riippuvaa lujuutta tutkittiin laboratoriossa SRS -kokeilla, joissa puristuskuormitusta lisätään hitaasti askeltaen. Laskelmien tulokset ovat yhtenäisiä laboratoriohavaintojen kanssa. Mallinnuksen perusteella vakiintuneissa yksi- ja kolmiaksiaalikokeissa alikriittisen raonkasvun vaikutus on vähäinen, mutta SRS-kokeissa sen merkitys on puolestaan huomattava. Mallin perusteella Äspö-dioriitin lujuus ei ajan myötä merkittävästi alene, jos vakiokuorma on alle 80% lyhytkestoisesta lujuudesta. Sivupaineen lisääminen lisää materiaalin lujuutta mutta ei merkittävästi vaikuta aikamurtumakäyrän muotoon.

Asiasanat: Rakomekaniikka, hauraan materiaalin murtuminen, alikriittinen raonkasvu, mallinnus, BEM/DDM.

ISBN 978-951-22-9434-3 (painettu)	ISSN 1795-2239 (painettu)
ISBN 978-951-22-9435-0 (pdf)	ISSN 1795-4584 (pdf)
Kieli Englanti	Sivumäärä 155

Julkaisija Teknillinen Korkeakoulu, Kalliorakentaminen

Painetun väitöskirjan jakelu Teknillinen Korkeakoulu, Kalliorakentaminen

(X) Luettavissa verkossa osoitteessa URL: http://lib.tkk.fi/Diss/2008/isbn9789512294350/

I SUMMARY

When a brittle rock specimen is loaded close to its short-term strength, inherent cracks start to extend slowly, i.e. subcritically. These subcritically growing cracks may reach a critical length for unstable, fast fracture propagation, resulting in a sudden failure of the specimen. A conceptual model for time-dependent crack growth is developed to evaluate the mechanical effects including delayed failure and stress relaxation of loaded rock. This model is based on brittle fracture mechanics principles and the subcritical crack growth (SCG) theory. A combination of these approaches allows the assessment of the time-dependent length of a subcritically growing crack and the calculation of the time it takes for an accelerating crack to grow subcritically to its critical length. Both tensional and compressive loadings are considered.

This SCG concept was incorporated in the fracture mechanics software FRACOD (FRActure propagation CODe). The method provides a reasonable description of the failure process in terms of new crack formation, fracture propagation, time-dependent failure and the stress-strain response of brittle rocks. Models using average material parameters of the Äspö diorite suggest that fractures propagate both in the direction of major principal compressive stress and in the shear stress direction under a uniaxial compressive load. Stable wing-crack propagation takes place under an increasing uniaxial load prior to crack coalescence and extensive unstable fracture propagation. The rupture of a rock specimen is dominated by the formation of large shear fractures. Dilation of these large fractures occurs in the late post-peak phase of failure, especially for those models subjected to low confinement. Modelled Class II post-peak behaviour is a powerful verification that the model captures the mechanisms involved in brittle rock failure. Class II post-peak behaviour as modelled by FRACOD is explained by the Griffith locus.

The effect of time on the load-bearing capacity of the Äspö diorite has been investigated by slow-rate loading experiments (Strain Rate Stepping (SRS) test). These experiments were modelled by using the SCG model implemented in the FRACOD software. Modelled time-dependent failure behaviour agrees well with laboratory findings and mirrors the underlying failure mechanisms. The modelling suggests that negligible amounts of SCG are involved in standard uniaxial and triaxial compressive strength tests, while for the slow-loading SRS tests the time-dependent effects are significant.

According to the predictive modelling, the long-term load-bearing capacity is not decreased severely when the applied load is below a certain level of the short-term peak strength. With the applied load corresponding to a stress of less than 80% of the peak strength, both 2 MPa and 7 MPa confined models suggest only slight SCG when the predictions were extended over 1 Ma. The effect of confinement increased the required stress/strain level for failure but do not affect the shape of the time-to-failure curve.

II PREFACE AND ACKNOWLEDGEMENTS

This thesis deals with modelling the subcritical crack growth (SCG) and time-dependent failure of brittle rocks. It was carried at the Laboratory of Rock Engineering, Helsinki University of Technology (HUT, Finland). This work follows on from my licentiate thesis (Rinne 2000) at the Royal Institute of Technology (KTH, Sweden) which focused on the stability of a given rock fracture system for different loading conditions.

The frame of this thesis is the CREEP-project that aims to develop a numerical tool to assess time-dependent behaviour of a fractured rock mass (Rinne 2003, Rasilainen 2006). The CREEP-project was integrated into the international collaboration DECOVALEX THMC project (D-THMC) subtask, Task B, dealing with ‘Understanding and characterizing of the Excavation Disturbed Zone’ (Hudson and Jing 2007, Hudson et al. 2007). The CREEP/ DECOVALEX project involved laboratory experiments at HUT and at GeoFrames GmbH (Germany). Numerical modelling and code development were carried out at Fracom Ltd (Finland/Australia). Besides the CREEP/DECOVALEX project, this study employs data provided by the APSE pillar project at the Äspö Hard Rock Laboratory (ÄHRL), Sweden (Andersson 2007).

I am very grateful to Dr Baotang Shen (Australia) who carried out major work to incorporate the SCG function into the FRACOD software. Baotang is always very innovative and he always found practical and efficient solutions for even the most complicated suggestions from my side. Innovative laboratory procedures were needed to be able to determine the parameters required for numerical modelling and to establish laboratory test cases to verify the numerical models. My sincere thanks go to Dr Juha Antikainen and Mr Pekka Eloranta and all my colleagues at the Laboratory of Rock Engineering at HUT for the successful laboratory experiments. A special thank you is addressed to Dr Tobias Backers at GeoFrames GmbH for doing great work in the laboratory to determine fracture properties.

During my stay in Stockholm in the mid-1990s I was introduced to the fascinating world of fracture mechanics by my contemporary chief Doc. Kennert Röshoff (BBK AB). It initiated my postgraduate studies at KTH under the supervision of Prof. Ove Stephansson. I am very thankful to both Kennert and Ove who are always inspiring me and have been very co-operative in relation to my research over all the years.

Special thanks are extended to my supervisor, Prof. Pekka Särkkä (HUT) for his support and encouragement to continue the doctoral course after my return from Stockholm back to Finland and for reviewing this thesis. Thanks are also directed to Mr Rolf Christiansson (SKB) for always being co-operative and for supplying the research team with rock samples and data from ÄHRL. Prof. Finn Ouchterlony (Swebrec at Luleå University of Technology) and Dr Flavio Lanaro (Berg Bygg Konsult AB, Sweden) are greatly acknowledged for going deep into my work, for discussions and for good comments while pre-reviewing my thesis.

The Ministry of Trade and Industry through the Nuclear Waste Research Fund (KYT) and the Posiva have been the major funding organisations of the CREEP/DECOVALEX project. Financial support to complete this thesis has been received from HUT and from the Academy of Finland (grant no. 213848), which are all gratefully acknowledged. The Hazama Corporation (Japan) and The Finnish Funding Agency for Technology and Innovation (TEKES) are acknowledged for their co-operative attitude and support in the code development.

Finally, I would like to thank Susanne, Caroline and Rasmus for their love, patience and understanding.

III AUTHOR’S CONTRIBUTION

The author’s main contribution in this thesis is the development of the time-dependent failure model. Although the time-dependent modelling is the main topic, many non-time-dependent models were set up to improve rock failure modelling and to advance the credibility of the time-dependent modelling. The theoretical studies (Chapter 3), models and results (Chapters 6 and 7), and analyses and conclusions (Chapters 8, 9 and 10) presented here are exclusively those of the author, if not otherwise stated.

The FRACOD software has been used as a platform for the time-dependent failure model. Dr Baotang Shen (CSIRO and Fracom, Australia) is the architect of this code. Dr Shen undertook all the software engineering and he is also responsible for implementation of the time-dependent model into FRACOD, as presented in Chapter 4.

The laboratory work related to the modelling is presented to the extent that the reader can form an idea about the material parameters that the model makes use of and to give background information of the modelled test cases. Intact rock laboratory experiments at Helsinki University of Technology (Section 5.2) were performed by Dr Juha Antikainen (result reporting and management) and by Mr Pekka Eloranta and Mr Panu Kaukinen (sample preparation, test performing and photographs). The fracture parameter testing and reporting of results were carried out by Dr Tobias Backers at GeoFrames GmbH, Germany (Section 5.3).

Some of the investigations presented in this thesis are accessible in technical reports of the APSE project (Rinne et al. 2003a, 2004), in progress reports of the CREEP-project (Rinne 2003, 2005, 2006), in the DECOVALEX research reports (Rinne and Shen 2007; Rinne et al. 2007a), and in symposium and conference proceedings (Rinne et al. 2003b, 2003c, 2005, 2006, 2007b). This thesis is a summary and an extension of the author’s investigations and findings presented in the aforementioned references.

To fair rules, fail rules and failures

Contents

LIST OF NOTATIONS AND ABBREVIATIONS

Symbols

A, B, C, D	Constants
A_{ini}	Initial fracture aperture
A_{res}	Residual fracture aperture
a	Half-crack length
a_{cr}	Critical half-crack length for fracture initiation
a_0	Initial half-crack length
Δa	Crack increment
c_i	Cohesion, intact rock
c_f	Cohesion, fracture
dn	Displacement in the normal direction
ds	Displacement in the shear direction
dx	Displacement in the x direction
dy	Displacement in the y direction
E	Young's modulus
E'	Effective Young's modulus
e	Strain
e_b	Element length, boundary
e_c	Element length, crack
G	Strain energy release rate
$G_{I,\ II,\ III}$	Strain energy release rate for Mode I, Mode II and Mode III
G_C	Critical strain energy release rate
$G_{IC,\ IIC,\ IIIC}$	Critical strain energy release rate for Mode I, Mode II and Mode III
K	Stress intensity factor
$K_{I,\ II,\ III}$	Stress intensity factor for Mode I, Mode II and Mode III
K_C	Critical stress intensity factor
$K_{IC,\ IIC,\ IIIC}$	Fracture toughness for Mode I, Mode II and Mode III
K_0	Subcritical crack growth limit, or stress corrosion limit
K_N	Fracture normal stiffness
K_S	Fracture shear stiffness
l	Sample length
Δl	Length of subcritical crack growth
N	Number of elements
n	Subcritical crack growth index
n_1	Subcritical crack growth index for Model I
n_2	Subcritical crack growth index for Model II
P	Applied load
p	Probability of fracture initiation
r	Sample radius
T	Temperature
T_{tot}	Total time
t	Time
Δt	Time step
U	Total energy
U_c	Total elastic strain energy release caused by a crack
U_s	Surface energy due to the formation of the new crack surfaces
U_t	Total initial elastic strain
V	Volume of the body
u	Displacement
v	Crack growth velocity

v_1	Crack growth velocity for Mode I
v_2	Crack growth velocity for Mode II
W	Strain energy, work
x, y, z	Co-ordinate axes

Greek Symbols

α	Crack inclination angle with respect to the applied load
β	Stress/strength ratio for new crack formation
ε	Strain
ε_n	Critical inelastic strain
ϕ_d	Dilation angle (crack)
ϕ_i	Friction angle (intact rock)
ϕ_f	Friction angle (fracture)
γ_s	Specific surface energy
φ	Angle
ν	Poisson’s ratio
θ_{it}	Direction of new crack formation in tension
θ_{is}	Direction new crack formation in shear
σ	Stress
σ_A	Applied stress
σ_{ci}	Crack initiation stress
σ_{ci}(AE)	Crack initiation stress interpreted from AE
σ_H	Homologous stress ratio
σ_i	Instant breaking stress
σ_n	Normal stress on plane
σ_m	Intact rock strength
σ_s	Shear stress on plane
σ_{shear}	Critical stress of new crack formation in shear
σ_t	Tensile strength
$\sigma_{tensile}$	Critical stress of new crack formation in tension
σ_{Ti}	Failure stress
σ_x	Stress in the x-axis direction
σ_y	Stress in the y-axis direction
τ	Shear stress in the x-y plane
τ_i	In-plane shear stress
τ_o	Out-of-plane shear stress

Abbreviations

AE	Acoustic Emission
APSE	Äspö Pillar Stability Experiment
BEM	Boundary Element Method
CB	Chevron-Bend (CB method)
COD	Clip-gage Opening Displacement
CREEP	Research project ‘Time-dependent fracturing of rock mass and modelling of EDZ of a repository for spent nuclear fuel’
CSIRO	Australian Commonwealth Scientific and Research Organization
DDM	Displacement Discontinuity Method
DECOVALEX	DEvelopment of COupled Models and their VALidation against Experiments (International research project related to deep geological radioactive waste deposing)
EDZ	Excavation Damage Zone
FPZ	Fracture Process Zone
FRACOD	FRActure propagation CODe
HUT	Helsinki University of Technology
ISRM	International Society for Rock Mechanics
KYT	Kansallinen Ydinjätehuollon Tutkimusohjelma Finnish Research Programme on Nuclear Waste Management
LEFM	Linear Elastic Fracture Mechanics
NEFM	Non-Linear Elastic Fracture Mechanics
Posiva	Finnish organisation responsible for the final disposal of spent nuclear fuel
PTS	Punch-Through-Shear (PTS test)
SCG	Subcritical Crack Growth
SKB	Svensk Kärnbränslehantering AB Swedish Nuclear Fuel and Waste Management Co
SKI	Svensk Kärnkraftinspektion, The Swedish Nuclear Power Inspectorate
SRS	Strain Rate Stepping Tests (SRS tests)
SSY	Small-Scale Yielding
Triax	Triaxial Compressive Strength Test (Triax test)
TTF	Time To Failure
UCS	Uniaxial Compressive Strength (UCS test)
ÄHRL	Äspö Hard Rock Laboratory
3PB	Three-Point Bending (3PB test)

1 INTRODUCTION

1.1 Aim of this study

Rock mass is utilised to an increasing extent as the host medium for different kinds of human activities. Facilities such as tunnels, storage areas, underground power stations, etc., are located in a variety of rock mechanical conditions, where hydro-thermo-mechanical and chemical processes are of importance. A common requirement for all these facilities is the excavation stability, both in the short- and the long-term. Understanding of long-term behaviour is particularly important for safety and performance assessments of geological disposal of radioactive waste.

Failure of brittle rock is often associated with a rapid and violent event as detected in short-term loading strength tests in the laboratory. When rock is stressed close to its short-term strength, slow crack growth, called subcritical crack propagation, takes place. This slow fracturing process may generate, with time, critical stress concentrations that lead to a sudden unstable failure event. Slow subcritical crack growth (SCG) is thought to play an important role in long-term rock stability at all scales, ranging from laboratory samples to earthquake-generating faults. Delayed failure can be detected as sudden rock movements around excavations and the consequences can be serious.

The ability to reproduce realistically the rock mass behaviour using a numerical model could provide an application tool for many rock-engineering issues. This study aims to improve understanding of time-dependent failure through laboratory experiments and numerical modelling. Laboratory experiments can provide us with fundamental data to develop a conceptual model of the failure process. Numerical modelling can improve our understanding of the complicated failure processes and help us to consider the coupled factors that affect the behaviour of fractured rock. The better our models manage to capture the fundamental failure mechanisms observed in the laboratory, the better chances we have of constructing reliable large-scale models and predicting the long-term behaviour of rock masses in situ. The ability to model time-dependent behaviour of rock also helps to identify those conditions where time may be of importance for the stability of the rock structure.

At the time that this study was initiated, there was no numerical model available that could explicitly simulate the time-dependent failure (delayed failure) of stressed rock by using SCG principles. This study aims to improve the fracture mechanics code FRACOD to have the capacity to assess the long-term behaviour of a fractured volume of brittle rock under various loading conditions.

1.2 Thesis structure

This thesis deals with the modelling of brittle rock failure and associated time-dependent effects. A conceptual model using the SCG theory is developed and implemented in the fracture mechanics software FRACOD. The laboratory work related to parameter determination and the modelled laboratory tests is presented.

Chapters 1 and 2 form an introduction to the main disciplines used in this thesis by summarising the cornerstones of classical fracture mechanics principles and SCG theory. The reader is introduced to the terminology and some key references are given.

Chapter 3 describes the concept developed in this study to model time-dependent effects of loaded brittle rocks. The model utilises principles presented in the previous chapters and the model is demonstrated by a simple analytical example.

Chapter 4 is a method description and gives an introduction to the Displacement Discontinuity Method (DDM), to the fracture criterion (F-criterion) and to the FRACOD software. The implementation of the SCG model into the FRACOD is also presented.

Chapter 5 describes the Äspö diorite that is used throughout this study as a reference rock material. Two laboratory investigation programs related to the CREEP-project are highlighted. The first program describes the Strain Rate Stepping tests (SRS tests) and aims to provide well-documented laboratory test cases for later comparison with numerical models. The second set of investigations presents newly developed testing methods that were used to determine subcritical fracture growth parameters under Mode I and II loading conditions.

Chapter 6 presents the results from FRACOD modelling. It introduces the reader to the failure mechanisms as suggested by the model and aims to simulate the failure of the Äspö diorite as observed in short-term strength tests including the pre- and post-peak failure behaviour. Factors affecting the failure are presented by examples.

Chapter 7 presents the results from time-dependent failure modelling. The models aim to reproduce the triaxial compression strength tests and SRS tests by using the SCG model. The effect of the loading rate on failure as found in the laboratory is compared with model results.

Chapter 8 discusses the models presented in the previous chapters and states the accuracy and reservations related to the FRACOD modelling. The sensitivity of results related to the material parameters is also discussed.

Chapters 9 and 10 summarise the results and make conclusions of the findings in this thesis and outline future work.

2 FRACTURE MECHANICS AND SUBCRITICAL CRACK GROWTH

In rock mechanics, the failure mechanisms generally refer to the overall processes of failure in a continuum sense by which a rock or rock mass suffers permanent damage which affects its ability to sustain a load. The failure criteria, such as the well-known Mohr-Coulomb or Hoek & Brown criteria, predict the failure conditions by applying the ultimate strength value of the matrix but do not take into account the localised stresses caused by discontinuities that are always inherent in the rock matrix.

Bieniawski (1967) distinguishes between a phenomenological failure criterion and a genetic failure mechanism. A phenomenological failure criterion simply provides a formula enabling the prediction of the strength values for all states of a multi-axial stress from a critical quantity that may be determined in one type of test, e.g. the uniaxial tensile or compression test. A genetic failure mechanism describes the processes taking place in the material in the course of loading and eventually leading to failure.

The failure of most rock materials is essentially a process of crack initiation and propagation. Therefore the phenomenological failure criteria, although widely used as a good approximation of overall rock behaviour, may not be adequate to describe the failure in detail. The Griffith theory (Griffith 1920), which led to the evolution of modern fracture mechanics, assumes that the propagation of the inherent flaws in the fabric is the source of failure of loaded brittle material. This approach provides a description of the transformation of an unbroken structural component into a fractured one by crack growth. Fracture mechanics assesses the strength of a stressed structure through the relationship between the loading condition, the geometry of the crack and the resistance to crack propagation in terms of critical stress energy release rate (G_C). Modification of the Griffith theory was later proposed by Irwin (1957), who described the stress distribution around the crack tip and introduced the concept of the stress intensity factor (K). Irwin could also show the equivalence of strain energy release rate (G) and stress intensity factor (K).

Irwin's concept assumes that a fracture tip that has a stress intensity equal to the material's fracture toughness (K_C – critical stress intensity factor) will accelerate to speeds approaching a terminal velocity that is governed by the speed of the elastic waves in the brittle medium. If the fracture propagation criterion is not met, that is if $K < K_C$, the fracture remains stable. In terms of the Griffith approach, a crack is stable when $G < G_C$, where G_C is the critical strain energy release rate. It was found in experiments on a wide range of materials that crack growth with significant rates can occur at values of K or G often far below the critical values of these parameters. This phenomenon is called subcritical crack growth (SCG), which is one of the key factors in the time-dependent failure behaviour of rocks (Atkinson 1984).

This chapter summarises the central concepts of classical fracture mechanics and the SCG theory. The reader is introduced to the terminology and some key references will be given.

2.1 Definitions

According to Bieniawski (1967), ‘crack initiation’ is the failure process by which one or more cracks are formed in a material hitherto free from any other cracks. Sometimes the crack initiation is referred to as the threshold stress value of the registered acoustic emission (AE) events σ_{ci}(AE) for a structure under increasing load. Some authors term the stress level where the volume of a test specimen in compression starts to increase after initial compaction the ‘crack initiation stress’ (σ_{ci}) (Martin and Chandler 1994). Bieniawski (1967) defines ‘fracture initiation’ as the failure process by which the pre-existing single crack or cracks in a material start to extend or grow, whilst ‘fracture propagation’ is defined as the failure process by which the pre-existing single crack or cracks are extending or growing subsequent to fracture initiation. A distinction can be made between two types of fracture propagation, namely ‘stable’ and ‘unstable’. Stable fracture propagation is the failure process of fracture propagation in which the crack extension is a function of the loading and can be controlled accordingly. Unstable fracture propagation is the failure process of fracture propagation in which the crack extension is also governed by factors other than the loading, thus it can become uncontrollable. A ‘rupture’ is the failure process by which a structure (e.g. rock specimen) disintegrates into two or more pieces. A ‘brittle fracture’ is defined as a fracture that exhibits little or no permanent (plastic) deformation.

In this thesis crack initiation indicates new crack formation through micro-mechanical processes. Fracture initiation indicates the onset of crack propagation and is confined to the vicinity of a pre-existent crack or fracture tip. Fracture propagation represents the process of crack extension from the crack tips to a new position, which eventually may lead to the catastrophic failure of the stressed material. Therefore the catastrophic failure is referred to as a global failure process.

Under tension, fracture initiation, unstable fracture propagation and crack coalescence take place almost simultaneously. In compression, the failure process is more complex, as will be discussed in Chapter 6. The rupture (failure) of the material results primarily from stable and unstable fracture propagation and crack coalescence rather than directly from fracture initiation. Rock materials are discontinuous at all scales. At the micro-scale, defects causing stress concentrations are micro-cracks, grain boundaries, pores, bedding planes, etc., while at the macro-scale geology fractures are referred to as joints (opening) and faults (shearing) based on their genesis (Pollard and Aydin 1988).

Since confusion might be caused by the use of various terms in different contexts in the literature dealing with fractures, definitions of certain terms used in this thesis are given. From the point of view of modelling, all the above-mentioned features are synonyms representing a discontinuity in the elastic material and a source for stress disturbance. In Chapter 4, cracks, fractures, joints, etc., are described mathematically using displacement discontinuity elements. The term ‘crack’ is reserved for short discontinuities of the grain size. The ‘fracture’ has a length several times the grain size and is used to refer to a crack that has extended into the matrix. A fracture usually shows a more irregular trace compared with a short crack. The distinction between cracks and fractures is not apparent and from the point of view of modelling they are equivalent. In Section 4.4, the mathematical treatment for modelling ‘newly formed cracks’ is described.

For conventional rock mechanics tests, only so-called ‘intact rock’ specimens are considered for testing. By ‘intact rock’ we refer in this thesis to a rock (specimen) without apparent, visually detectable cracks. In reality, an ‘intact rock’ specimen contains different kinds of micro-scale discontinuities which have a major role in the failure process.

2.2 Griffith flaws and energy balance theory

Based on the fact that the tensile strength of a material is much lower than that theoretically predicted, Griffith (1920) postulated that typical brittle materials inevitably contain numerous submicroscopic flaws, micro-cracks or other discontinuities, which are distributed with random orientation throughout the volume of the material. These discontinuities often referred as Griffith flaws or Griffith cracks serve as stress concentrators. The Griffith approach is based on the stress analysis of Inglis (1913) who showed that the local stresses around an elliptical hole could increase to a level several times that of the applied stresses. Griffith established a relationship between critical stress and the crack size. This approach has since become known as the Griffith energy balance approach, which is the starting point for the development of modern fracture mechanics.

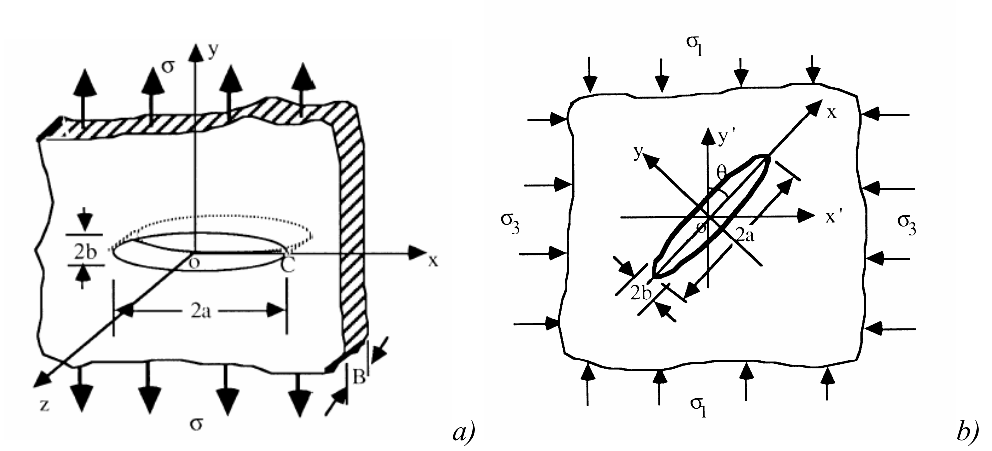

Figure 2-1. A crack subjected to a) uniform tension; and b) biaxial compression (Whittaker et al. 1992).

Griffith explained how failure is caused by the extension of flaws, cracks, etc. The creation of a new crack surface absorbs energy that is supplied from the work done by the external force. Release of the stored strain energy in the solid promotes the failure.

There are two necessary requirements to cause failure: a stress and an energy requirement. The stress requirement states that the local stress must be high enough to overcome the molecular cohesive strength. This can be achieved by the stress concentration due to the presence of discontinuities such as pre-existing micro-cracks. The energy requirement states that sufficient potential energy must be released to overcome the resistance to crack propagation. This can also be achieved through increasing the work done by external forces. The more energy a solid absorbs, the greater its resistance to crack propagation.

In pure tension, the total energy U of an infinite cracked plate (Fig. 2-1a) can be written in the following energy components (Whittaker et al. 1992):

$$U = U_t + U_c - W + U_s \qquad (2\text{-}1)$$

U = Total energy of the infinite cracked plate
U_t = Total initial elastic strain energy of the stressed but un-cracked plate
U_c = Total elastic strain energy release caused by the introduction of a crack of length $2a$ and the relaxation of the material above and below the crack
W = Work done by the external forces
U_s = Change in the elastic surface energy due to the formation of the new crack surfaces (irreversible).

The energy components can be obtained separately from the theory of elasticity:

$$U = \frac{\sigma^2 A}{2E'} \pm \frac{\pi\sigma^2 a^2}{E'} - \frac{\sigma\varepsilon A}{2} + 4a\gamma_s \qquad (2\text{-}2)$$

σ = Tensile stress
a = Half-crack length
E' = Effective Young's modulus: $E' = E$ for plane stress and $E' = E/(1-\nu^2)$ for plane strain
ν = Poisson's ratio
A = The infinite area of the thin plate of unit thickness ($B = 1$)
ε = Average axial strain in the plate
γ_S = The specific surface energy, i.e. the energy required to create a unit area of new crack surface as the crack increases in length.

Two extreme loading conditions can be considered (Fig. 2-2): a) Constant displacement (fixed-gripped loading) – the applied loading system suffers zero displacement as the crack extends; b) Constant load (dead-weight loading) – the applied force remains constant as the crack extends. In the first case there is no work done by the external force P. Therefore, U_c should have a negative sign in Eq. (2-2). In the second case the work done by the applied load P increases the elastic strain energy release and accordingly U_c should be positive. In the real loading situations the boundary conditions are generally between case a) and case b), as explained in Fig. 2-7.

It is noteworthy that W must be subtracted from the reversible energy terms, since it does not form part of the potential energy ($U_p = U_t + U_c - W$) of the plate. The mechanical energy released during incremental crack propagation is independent of the loading configuration (Lawn 1993).

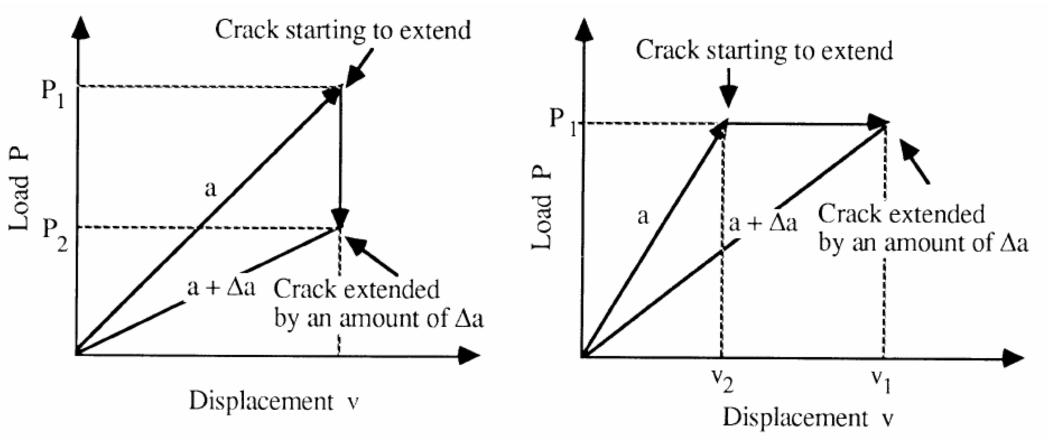

a) *b)*

Figure 2-2. *Load-displacement illustration for crack propagation: a) constant displacement; b) constant load (Whittaker et al. 1992).*

The Griffith's idea implies that the critical equilibrium for fracture initiation occurs when:

$$\frac{\partial U}{\partial a} = 0 \text{, which leads to} \qquad (2\text{-}3)$$

$$\sigma\sqrt{\pi \cdot a} = \sqrt{2E' \cdot \gamma_s} \qquad (2\text{-}4)$$

Equation (2-4) indicates that fracture initiation in ideally brittle solids is governed by the product of an applied far-field stress and the square root of the crack length and by the material properties characterised by Young's modulus *E*, Poisson's ratio ν and the specific surface energy γ_s.

Rearrangement of the term in Eq. (2-4) gives:

$$\frac{\pi\sigma^2 a}{E'} = 2\gamma_s \qquad (2\text{-}5)$$

The left-hand side of the equation represents the elastic energy per unit crack surface. This energy is available for crack propagation and it defines an important parameter called the strain energy release rate, denoted by *G* in honour of Griffith. Thus, an expression for the strain energy release rate *G* can be given by:

$$G = \frac{\pi\sigma^2 a}{E'} \qquad (2\text{-}6)$$

The Griffith theory for the critical condition for fracture initiation becomes:

$$G = G_C \qquad (2\text{-}7)$$

where G_C is the critical strain energy release rate. G_C is defined as the critical value of strain energy released per unit length of crack extension. More generally, *G* is defined as the derivative of the elastic strain energy release with respect to crack area rather than crack length. The above formulation describes a simple case of a flat and open elliptical crack subjected perpendicularly to a uniaxial tensile load and it is assumed that the crack propagates along its own plane. It is indicated that the strain energy release rate is the governing parameter for crack initiation, which is accordingly referred to as the energy balance approach. This approach is applied in section 6.5.6 to explain the Griffith locus and the post-peak failure behaviour of laboratory tests. With his flaw hypothesis and energy balance concept Griffith had laid a solid foundation for a general theory of fracture. He further improved his concept known as the 'fracture stress approach' to consider more complicated stress fields involving compression (Fig.2-1).

Plane crack in uniform tension represents just one application of the energy-balance equation (2-3). Griffith's ideas from different viewpoints have been derived and presented in the literature (e.g. Irwin 1957, Berry 1960, Cook 1965, Whittaker et al. 1992, Lawn 1993, Jaeger et al. 2007).

The energy change of crack formation can be considered as entire crack formation from the initially intact rock body, as presented above, or as an incremental extension of an existing crack. In Fig. 2.1 the boundary conditions were obtained as uniform farfield tensile stresses. In practical applications it is often useful to describe crack extension in terms of an external force (point load P), cross section of new crack surface (dc) and using the elastic compliance (λ), defined as the load-point displacement (u_0) per unit load (e.g. Lawn 1992). Evaluating parameter G can be considered with respect to new crack area rather than the crack length at equilibrium for crack initiation (eq.2-3).

One of the most widely used extensions of Griffith's work is Irwin's stress intensity factor approach, which is presented in section 2.4. The numerical application presented in Chapter 4 basically utilises the concepts of the Griffith energy release rate (G) approach. Irwin's stress intensity approach is presented because the SCG theory is generally described in terms of stress intensity factor K. These two approaches are, however, comparable as discussed in Section 2.5.

2.3 Loading modes and associated displacements

The flat crack tip in an ideally linear elastic brittle material can be subjected to a normal stress σ, an in-plane shear stress τ_i, an out-of-plane (or anti-plane) shear stress τ_o, or any combination of these. Figure 2-3 illustrates the crack tip co-ordinates and stress state in terms of both Cartesian and polar co-ordinates. Different loading configurations at the crack tips lead to different modes of crack tip surface displacements. The three basic loading configurations form the three basic fracture modes of crack tip deformation, Mode I, Mode II and Mode III, which are illustrated in Fig. 2-4.

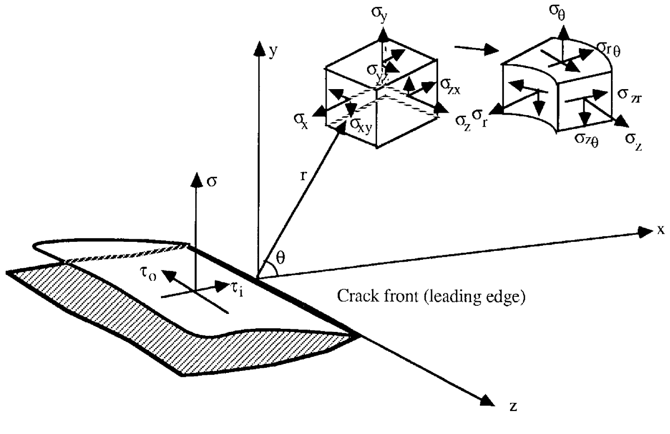

Figure 2-3. *Crack tip co-ordinates and stress state in terms of both Cartesian and polar co-ordinate systems (Whittaker et al. 1992).*

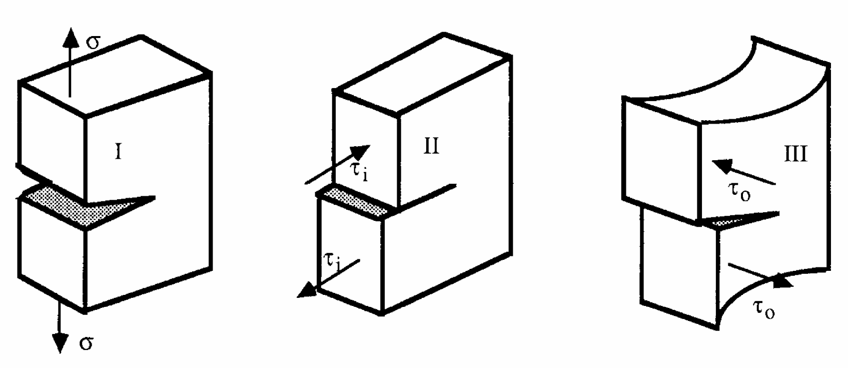

Figure 2-4. *The three basic modes of loading for a crack and the corresponding crack surface displacements (Whittaker et al. 1992).*

Mode I is the opening (or tensional) mode. The crack tip is subjected to a stress σ normal to the crack plane and the crack faces separate at the crack front so that the displacements of the crack surfaces are perpendicular to the crack plane.

Mode II is the edge-sliding mode (or in-plane shearing) where the crack tip is subjected to an in-plane shear stress τ_i and the crack faces slide relative to each other so that the displacements of the crack surfaces are in the crack plane and perpendicular to the crack front.

Mode III is the tearing (or out-of plane) mode. The crack tip is subjected to an anti-plane shear stress τ_o. The crack faces move relative to each other so that the displacements of the crack surfaces are in the crack plane but parallel to the crack front.

Mixed-mode loading is a combination of any of the three loading modes. For example, a combination of Mode I and Mode II loading forms a Mixed-mode I-II loading.

2.4 Stress intensity factor approach

The Griffith 'energy balance approach' has formed a solid basis for Irwin's (1957) widely applied 'stress intensity factor approach'. It is based on the crack tip characteristic parameter, called the stress intensity factor *K*, which uniquely governs the crack tip stress and displacement fields. For a given cracked body under a certain type and magnitude of loading, *K* is known and the stresses and displacements can be determined accordingly.

The three stress intensity factors (K_I, K_{II}, K_{III}) each correspond to a loading mode (Fig. 2-4), and each is associated with a unique stress distribution near the fracture tip. A detailed breakdown of stresses for an infinite plate containing a central crack of length 2*a* under uniaxial tension, σ, as shown in Fig. 2-1a is given below as an example.

$$\begin{bmatrix} \sigma_x \\ \sigma_y \\ \sigma_{xy} \end{bmatrix} = \frac{K_I}{\sqrt{2\pi \cdot r}} \cos\frac{\theta}{2} \begin{bmatrix} 1 - \sin\frac{\theta}{2}\sin\frac{3\theta}{2} \\ 1 + \sin\frac{\theta}{2}\sin\frac{3\theta}{2} \\ \sin\frac{\theta}{2}\cos\frac{3\theta}{2} \end{bmatrix} \qquad (2\text{-}8)$$

where $K_I = \sigma\sqrt{\pi \cdot a}$ (2-9) and r is the distance from crack tip, $\sigma_z = \nu(\sigma_x + \sigma_y)$ for plane strain and $\sigma_z = \sigma_{xz} = \sigma_{yz} = 0$ for plane stress. The crack tip stress components are often expressed in terms of polar co-ordinates in 2D:

$$\begin{bmatrix} \sigma_r \\ \sigma_\theta \\ \sigma_{r\theta} \end{bmatrix} = \frac{K_I}{\sqrt{2\pi \cdot r}} \cos\frac{\theta}{2} \begin{bmatrix} 1 + \sin^2\frac{\theta}{2} \\ \cos^2\frac{\theta}{2} \\ \sin\frac{\theta}{2}\cos\frac{\theta}{2} \end{bmatrix} \qquad (2\text{-}10)$$

where $\sigma_z = \nu(\sigma_r + \sigma_\theta)$ for plane strain and $\sigma_z = \sigma_{rz} = \sigma_{\theta z} = 0$ for plane stress.

Stress fields can be described for loading Modes II and III in a similar manner by equations involving the stress intensity factor K_N (N = II, III) and the geometrical term. The stress intensity factors K for Mode II and Mode III, respectively, can be defined as follows:

$$K_{II} = \tau_i \sqrt{\pi \cdot a} \qquad (2\text{-}11)$$

and

$$K_{III} = \tau_0 \sqrt{\pi \cdot a} \qquad (2\text{-}12)$$

where τ_i is the far-field in-plane shear stress and τ_o is the far-field anti-plane shear stress (Figs 2-4, 2-5).

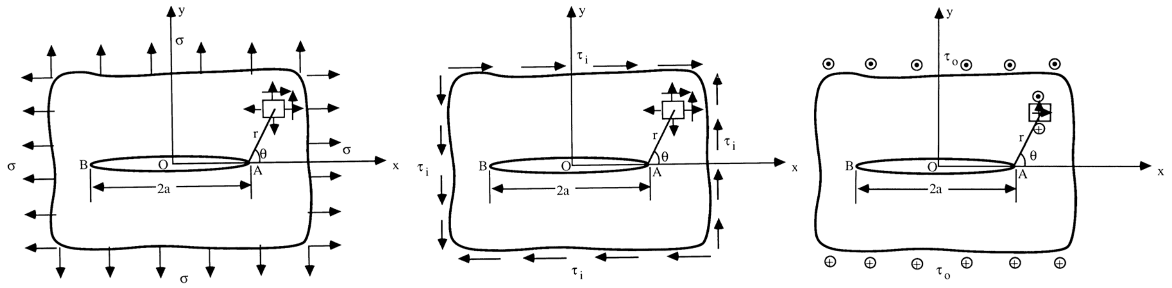

Figure 2-5. *An infinite plate containing a crack under biaxial tension, in-plane shear and anti-plane shear (Whittaker et al. 1992).*

The stress intensity factors ($K_{I,\,II,\,III}$) are dependent on the magnitude of the far-field stress and the crack size. In this sense, stress intensity factors can be physically regarded as fracture parameters reflecting the distribution of the stress in a cracked brittle body. Consequently, for any specific mode, with knowledge of the stress intensity factor, the crack tip stresses and displacements can be uniquely determined. The derivation of crack tip displacements follows the crack tip stresses using Hooke's law. According to the superposition principle the crack tip stress and displacement components for a Mixed-mode I-II loading can be obtained by superimposing those resulting from pure Mode I and pure Mode II loadings.

Closed-form solutions of the stress and displacement functions can be found for simple loading configurations in fracture mechanics handbooks (Whittaker et al. 1992; Lawn 1993; Andreev 1995). In practice, geometries of cracked bodies and loading conditions are usually complicated; therefore closed-form solutions are generally not available. For a cracked body of finite dimensions, numerical methods are usually needed to calculate the stress and displacement distributions. In addition, when the fracture criteria are used to study the crack initiation under compression the problem is more complicated because the crack faces tend to close and frictional forces must be considered.

According to Eqs (2-8) and (2-10), the stress approaches infinity (singular) at the tip of a crack (when $r \rightarrow 0$). This, however, is practically impossible since no material can bear infinity stress. When the stresses near the crack tip exceed the yield strength σ_{ys} the material yields until the stresses drop below σ_{ys}. Accordingly, a small region around the crack tip is formed in which the material behaves plastically rather than elastically as is usually assumed for the treatment of fracture mechanics problems. This small region has many names depending on the material. For brittle rock, this region is called the 'crack tip micro-cracking zone', the 'crack tip inelastic zone' or the 'Fracture Process Zone (FPZ)'. The presence of this inelastic zone ahead of the crack tip affects the fracture behaviour of the material.

The application of an elastic analysis to a real cracked body depends on the extent of the FPZ. If the FPZ is sufficiently small compared with the geometry of the crack and any other characteristic dimensions of the specimen, then it can be assumed that the linear elastic behaviour before failure prevails. If the inelastic zone satisfies the requirement, it is referred to as small-scale yielding (SSY) and the elastic analysis of such a cracked body is termed Linear Elastic Fracture Mechanics (LEFM). In general, SSY can be met for a plane strain fracture of a high-strength metallic material and for a fracture of intrinsically brittle materials, such as rock, glasses, ceramics, etc. (Whittaker et al. 1992).

In contrast, if the non-linear elastic deformation is a dominant preceding failure and the non-linear elastic zone is substantial, i.e. large-scale yielding (LSY), such an analysis is termed Non-Linear Elastic Fracture Mechanics (NEFM). In such an analysis, K can no longer characterise the crack tip stress, strain and displacements, since prior to failure the crack tip has become very blunted due to the formation of a yielded region in metals or micro-cracking in rocks. The R-curve concept, developed from the Griffith energy balance theory, can be used to deal with fracture problems involving the crack tip non-linear region; the J-integral and the crack opening displacement approaches can treat fracture problems involving relative large crack tip non-linear zones (Whittaker et al. 1992).

2.5 The relation between *G* and *K*

Irwin (1957) showed the relation between the global energy parameter, the strain energy release rate *G*, and the local crack tip parameter, the stress intensity factor *K:*

$$G_I = \frac{K_I^2}{E'} \quad (2\text{-}13)$$

$$G_{II} = \frac{K_{II}^2}{E'} \quad (2\text{-}14)$$

$$G_{III} = \frac{K_{III}^2}{2\mu} \quad (2\text{-}15)$$

Where G_I, G_{II} and G_{III} are the strain energy release rates for Mode I, Mode II and Mode III, respectively, and μ is the shear modulus.

$$\mu = \frac{\mathrm{E}}{2(1+\nu)} \quad (2\text{-}16)$$

The above relations between *G* and *K* for different modes of loading are obtained by assuming that the crack extends along its own plane. If a crack extends at an angle with respect to the crack plane, the relation between *G* and *K* is more complex. When a crack is exposed to a Mixed-mode I-II loading, the overall strain energy release rate, *G*, is a summation of the Mode I strain energy release rate, G_I, and that of Mode II, G_{II}, which indicates that the strain energy release rates for various loading modes are additive and that the superposition principle applies not only to the same mode but also for different modes. This is similar to the crack tip stress and displacement fields, but is unlike the stress intensity factors that are additive only for the same mode. The equivalence of *G* and *K* is important and forms the basis for the development of other branches of fracture mechanics involving LEFM, NEFM, dynamic fracture mechanics, statistical fracture mechanics, composite fracture mechanics etc. (Whittaker et al. 1992).

2.6 K and the critical value K_C

If the fracture initiation criterion is expressed for Mode I loading in terms of the stress intensity factor, then it is based on the assumption that crack initiation occurs when the stress intensity factor reaches its critical value called the Mode I plane strain fracture toughness, K_{IC}:

$$K_I = K_{IC} \tag{2-17}$$

Similarly, in Mode II, when the crack tip stress intensity factor, K_{II}, reaches the Mode II plain strain fracture toughness, K_{IIC}, cracking will initiate. The fracture toughness is basically a property of the material reflecting its resistance to physical macroscopic separation through crack propagation. Conceptually, K_C is a constant and should not vary with various factors. Due to the fact that K_C can be obtained by laboratory testing using appropriate specimens whose corresponding stress intensity factor is known, this approach has gained increasing popularity. Analyses related to Mixed-mode loading conditions are common. For example, for an angled crack subjected to a uniform far-field compressive stress, both K_I and K_{II} at the crack tip must be considered (Fig. 2-1b). According to the superposition principle, the crack tip stress and displacement components can be obtained by superimposing those resulting from pure Mode I and pure Mode II loadings.

Crack initiation will occur when a certain combination of K_I and K_{II}, $f(K_I, K_{II})$, reaches a critical value, $f(K_I, K_{II})_C$. The quantity $f(K_I, K_{II})_C$ is known as the Mixed-mode I-II fracture toughness envelope or the K_I-K_{II} envelope. The question is: what is the exact K_I-K_{II} envelope as a criterion for Mixed-mode I-II cracking? The development of a fracture criterion to predict the initiation and propagation of individual cracks in rock subjected to arbitrary loading conditions is of importance for rock engineering. On the basis of the assumption that the crack propagation is governed by a specific parameter, various fracture criteria have been established. The three fundamental fracture criteria of maximum tangential stress, maximum energy release rate and minimum strain energy density appear to be the most frequently referred to approaches in the literature. Common to these criteria is that they aim to predict the initiation and direction of crack initial extension under Mixed-mode I-II loading. Descriptions of a number of Mixed-mode fracture criteria and comparisons of predicted results are presented for example in Whittaker et al. (1992), Shen (1993) and Rao (1999). Shen and Stephansson (1993a) suggested a criterion for fracture propagation under Mixed-mode I-II loading based on the maximum energy release rate. This improved G-criterion is further explained in Section 4.1.

2.7 Subcritical crack growth and stress corrosion

Different aspects of SCG and stress corrosion mechanisms of geological materials are reported comprehensively in the literature (Atkinson and Meredith 1987; Olson 1993; Ngwenya et al. 2001; Nara and Kaneko 2003, 2005a, 2005b). A comprehensive review of the experimental data on SCG in geological materials has been presented in Atkinson (1984). Research on SCG concentrates almost exclusively on Mode I loading conditions.

Subcritical crack growth can be caused by several competing mechanisms, such as stress corrosion, diffusion, dissolution, ion exchange and microplasticity. A particular mechanism will be dominant under specific ranges of environmental and material conditions. It is, however, assumed that stress corrosion is the main mechanism of SCG in shallow crustal conditions (Atkinson 1984).

In its most elementary form, the theory of stress corrosion postulates that for crystalline silicates and for silicate glasses the strained Si-O bonds at crack tips can react more readily with the environmental agents than unstrained bonds, because of a strain-induced reduction in the overlap of atomic orbitals (Michalske and Freiman in Atkinson 1987). The reaction between strained bonds and the environmental agent produces a weakened (an activated) state that can then be broken at lower stresses than the unweakened bonds. For silicate glasses and quartz in water environments, a general expression for weakening has been proposed as follows:

$$\mathrm{H-O-H}+\left[\equiv \mathrm{Si-O-Si}\right]\Leftrightarrow\equiv \mathrm{Si-OH}\bullet\mathrm{HO-Si}\equiv\Leftrightarrow 2\left[\equiv \mathrm{Si-OH}\right] \qquad (2\text{-}18)$$

2.8 Stress intensity factor and crack velocity

The actual time dependency of crack growth is due to rate-controlled processes acting at the tips of cracks where stress concentration exists. The propagation velocities can vary over many orders of magnitude as a function of the stress intensity. Many experimental studies on rocks have been made at crack velocities down to 10^{-9} m/s and K values less than 0.5 K_C (Atkinson and Meredith 1987). Some have even reached crack velocities that were inferred to be as slow as 10^{-12} m/s (Wilkins 1980).

The SCG velocity increases as (G or K) is increased. The exact form of the relationship

$$v = \mathrm{f}(G \text{ or } K) \qquad (2\text{-}19)$$

depends on the crack growth mechanisms, until the critical value $(G \text{ or } K)_c$ is achieved. At this critical level, the crack propagates catastrophically and accelerates rapidly to speeds approaching a terminal velocity that is governed by the speed of the elastic waves.

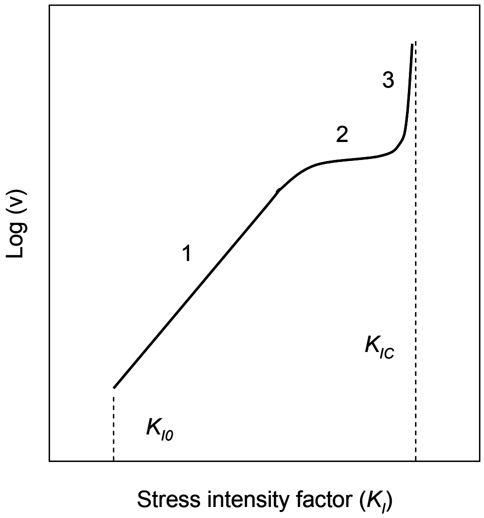

Figure 2-6. *Schematic stress intensity factor/crack velocity diagram for subcritical tensile crack growth (Atkinson 1984).*

Figure 2-6 shows the three regions of behaviour from SCG studies on glass. The SCG mechanisms and the interaction between the environment and the microstructure of the solid will control the details of the stress intensity factor/crack velocity curve. The schematic figure is presented merely as a starting point and its shape varies considerably when the effective factors such as temperature, pore pressure, pH, etc., are changed (Atkinson 1984).

The behaviour in Region 1 is controlled by the rate of stress corrosion reactions at the crack tips. Region 2 is controlled by the rate of transport of reactive species to the crack tips. In Region 3, crack growth is mainly controlled by mechanical rupture and it is relatively insensitive to the chemical environment. Most experimental data on subcritical tensile crack propagation in geological materials appear to be in Region 1 or Region 3 of the schematic stress intensity factor/crack velocity curve. Region 2 is apparently found in tests on black gabbro in water but it is not frequently observed in all types of rocks (Atkinson 1984).

It is assumed that there exists a threshold below which no significant crack propagation can occur through stress corrosion (K_0, stress corrosion limit). The value of this parameter is a function of the material's fracture properties and its environment. It is likely that K_0 is a small fraction of about 10-20% of K_C. However, experiments have certainly not yet confirmed the existence of a stress corrosion limit in ceramics and rocks (Atkinson 1984).

2.9 Charles law

Delayed failure of glass in relation to its sensitivity to atmospheric corrosion was investigated by Charles (1958). In this paper, the rate of corrosion layer formation of lime glass rods treated in saturated water vapour was studied. An analysis of the failure process was presented and it was based on the concept that inherent surface flaws grow by corrosive mechanisms to critical dimensions through a reaction between water vapour in the atmosphere and the components of glass. The rate of this reaction is determined by the local stress conditions and by the temperature, pressure and composition of the surrounding atmosphere. Experimental work shows a close relationship between the temperature dependence of the failure process and that of the self-diffusion of the sodium ion in bulk glass. It is concluded that the alkali content is responsible for the very low long-term strengths of most inorganic glass.

Charles assumed a stress power relationship to describe the crack velocity controlled by the rate of stress corrosion reactions at the crack tip:

$v(T) = k'(\sigma_m)^n + k$, where (2-20)

v = Penetration velocity of crack tip
T = Temperature
σ_m = Tensile stress at crack tip
k = Corrosion rate of the material under zero stress, and
k' and n are constants.

For the stress-activated corrosion, Charles further assumed that the temperature dependence of the flaw growth process takes the form of an Arrhenius-type relationship. Bearing in mind that the stress at the crack tip is related to crack size and geometry, he suggested the following type of crack growth relationship:

$$v \approx C\left(\frac{x}{x_{cr}}\right)^{n/2} e^{-A/RT} \qquad (2\text{-}21)$$

where
C = Constant
x, x_{cr} = Crack size and critical crack size
A = Activation energy term, and
R = Gas constant.

A variety of mathematical functions can be fitted to the laboratory data for describing the stress intensity as a function of subcritical crack velocity, as presented in Atkinson (1984), Lajtai and Bielus (1986), Atkinson and Meredith (1987) and Costin (1987). Subcritical crack growth data have been expressed by power law, exponential and hyperbolic functions. With a database restricted to crack velocities that are obtained in laboratory experiments, it is impossible to distinguish between the several types of mathematical functions for most data sets (Atkinson 1984; Lajtai and Bielus 1986). In other words, different models can be matched with the data. The predictions of these models, however, diverge significantly at slow crack velocities. This dilemma poses an important limitation on extrapolation of laboratory data on SCG to long-term predictions. The form of the equation for low-temperature crack velocity of different rock types is still being discussed (Main 2000; Ngwenya et al. 2001).

2.10 Creep and stress relaxation

There can be confusion concerning the meaning of the terms 'creep', 'stress relaxation' and 'fatigue'. In Fig. 2-7, a rock specimen is illustrated being loaded in compression through an adjacent rock element represented by the spring (Hudson et al. 2007). Creep is defined as increasing strain while the stress is held constant. Stress relaxation is defined as decreasing stress while the strain is held constant. In the laboratory, and especially for the rock around an underground excavation, a rock element will be loaded via the stiffness of an adjacent element and so the time-dependent behaviour will be somewhere between the ideal conditions of creep and stress relaxation, as illustrated in Fig. 2-7. Fatigue refers to an oscillation in the applied stress producing permanent strain (Hudson et al. 2007).

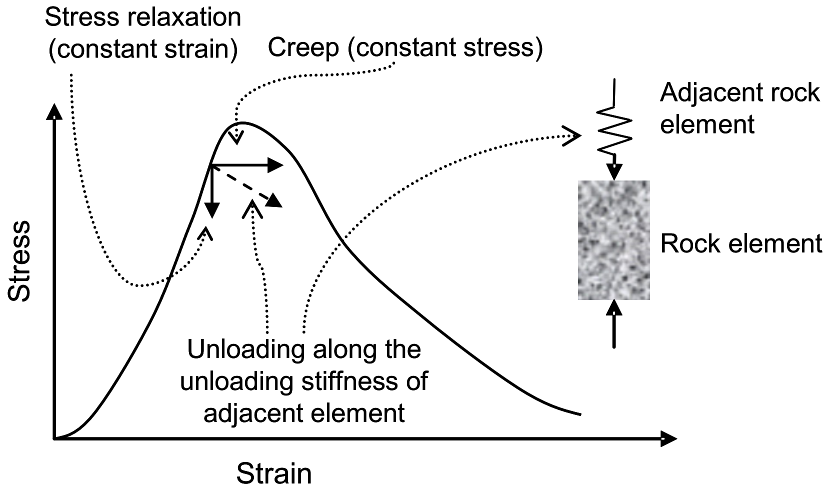

Figure 2-7. *Definitions of creep, stress relaxation and time-dependent unloading along the stiffness of the adjacent element (Hudson et al. 2007).*

The high state of stress around a tunnel results from the concentration of the primary regional stresses. Some failure of the rock may have occurred but the excavation-peripheral rock is subject to high stresses for a long period of time. Each rock element in the excavation periphery is loaded by another rock element and so the time-dependent behaviour for a highly stressed rock element will be along the dashed arrow as shown in Fig. 2-7. The stress will reduce and the strain will increase. Time-dependent failure can occur if the dashed line intersects the failure locus.

3 CONCEPTUAL MODEL FOR TIME-DEPENDENT FAILURE

In this chapter, a conceptual model for time-dependent crack growth is presented. The model was developed to be able to evaluate the time-dependent mechanical effects including the delayed failure of rock loaded below its short-term strength. This model makes use of fracture mechanics principles and SCG theory as presented in Chapter 2. A combination of these approaches allows assessment of the time dependency of the length of a subcritically growing crack, or calculation of the time it takes for an accelerating crack to grow subcritically to its critical length. Both tensional and compressive loading are considered.

In literature, a number of models aiming to predict time-dependent mechanical behaviour of stressed rock have been presented (Lajtai and Bielus 1986; Kemeny 1993, 2002; Fakhimi and Fairhurst 1994; Napier and Malan 1997; Lockner 1998; Napier 1999; Malan and Drescher 2000). Many models are based on the assumption that some strength parameters decline with time. In this study, the SCG theory was chosen to be the platform for the time-dependent model due to its theoretically sound base. This approach also implies the potential to involve environmental variables such as thermal and chemical factors in the model, as characterised by the Arrhenius equation. There are also well-established methods available to define Mode I SCG parameters *n* and *A* in the laboratory (Wilkins 1980, Atkinson 1987). Within the CREEP-project, a method to determine Mode II SCG parameters was developed (Backers 2006). Methods used to determine fracture parameters in this thesis are presented in Section 5.3.

3.1 Subcritical crack growth in uniaxial tension

Charles's (1958) power law dependence, as presented in the previous chapter, is the most commonly used equation to describe stress corrosion in tension at constant temperature. In the literature, the equation is often presented in a form where the relationship between the stress intensity factor and the crack growth velocity (v) is considered as follows:

$$v = v_0^{'} e^{(-H/RT)} K^n \tag{3-1}$$

where H is the activation enthalpy, R is the gas constant, T is the absolute temperature, and $v_0^{'}$ and n are constants. This equation fits a large body of experimental data on many different classes of materials, including rocks and minerals (Atkinson 1984, 1987).

In Region 1 (Fig. 2-6), the crack velocity is controlled by the rate of stress corrosion reactions at the crack tip. Since time-dependent failure in rock is almost totally in Region 1, the behaviour in other regions will not be considered in this analysis. Equation (3-1) is further simplified by assuming a constant temperature. For loading in Mode I, the relationship can be expressed as follows:

$$v_I = A_I \cdot K_I^{n_I} \tag{3-2}$$

where v_I is the Mode I crack velocity, A is a constant, K_I is the stress intensity factor in Mode I loading conditions and n_I is the SCG index or stress corrosion index when this latter mechanism dominates. The stress corrosion index n is a measure of the susceptibility of the material to stress corrosion cracking in the particular environment. Experimentally the factor n has been found to depend on both the fracture growth mechanism and the rock type (Atkinson and Meredith 1987). As n becomes very large then Eq. (3-2) describes the velocity conditions for brittle failure with less time effects. Values of n as low as 9.6 have been found for tensile cracking of quartz in a basic environment and as high as 170 for tensile cracking of basalt in moist air (Atkinson and Meredith 1987).

To compare different materials with different fracture toughness values (K_{IC}), the stress intensity factor is normalised with its critical value by using the relationship:

$$A_I = B_I / K_{IC}^{n_I} \tag{3-3}$$

Implementing this in Eq. (3-2) we get:

$$v_I = B_I \cdot \left(\frac{K_I}{K_{IC}} \right)^{n_I} \tag{3-4}$$

Consider an infinite plate containing a crack of length $2a$ under uniaxial tensile stress as presented in Fig. 2-1a. According to fracture mechanics principles the fracture starts to propagate when the stress intensity at the crack tip reaches its critical value:

$$\frac{K_I}{K_{IC}} = 1 \tag{3-5}$$

where K_{IC} is the fracture toughness.
The stress intensity factor K_I is a function of applied stress (σ) and the half-crack length (a). For a uniaxial tensile crack in an infinite elastic plate, it can be expressed as follows:

$$K_I = \sigma \sqrt{\pi \cdot a} \tag{3-6}$$

If the stress intensity factor is kept constant by controlled loading, the crack velocity in Eq. (3-4) is constant and the time-dependent crack length can be easily calculated by multiplying the velocity by time. In most loading configurations, however, the K_I is not constant as the crack grows. For example, under a constant load (dead-weight loading), as the crack grows subcritically, the stress intensity factor will increase, leading to an accelerating crack velocity. To consider the increasing stress intensity factor, the half-crack length at time (t) must be calculated. Incorporating Eq. (3-6) into Eq. (3-4) yields:

$$v_I = B_I \cdot \left(\frac{\sigma \sqrt{a \cdot \pi}}{K_{IC}} \right)^{n_I} \tag{3-7}$$

Considering the crack velocity as a function of time:

$$v_I = \frac{da}{dt} \tag{3-8}$$

we get:

$$\frac{da}{dt} = B_1 \cdot \frac{\sigma^{n_1} \cdot a^{n_1/2} \cdot \pi^{n_1/2}}{K_{IC}^{n_1}} \tag{3-9}$$

By rearranging terms and by integrating with the initial condition $a = a_0$ when $t = 0$, the half-crack length *a(t)* at a certain time (*t*) can be calculated:

$$\int_{a_0}^{a(t)} a^{-n_1/2} \cdot da = \int_0^t B_1 \cdot \frac{\sigma^{n_1} \cdot \pi^{n_1/2}}{K_{IC}^{n_1}} \cdot dt \quad => \tag{3-10}$$

$$\frac{a(t)^{\left(-n_1/2\right)+1}}{-n_i/2+1} - \frac{a_0^{\left(-n_1/2\right)+1}}{-n_1/2+1} = B_1 \cdot \frac{\sigma^{n_1} \cdot \pi^{n_1/2}}{K_{IC}^{n_1}} \cdot t \qquad n_1 \neq 2\ , => \tag{3-11}$$

$$a(t) = \left\{ a_0^{1-n_1/2} + \left(1-n_1/2\right) \left(B_1 \cdot \left(\frac{\sigma\sqrt{\pi}}{K_{IC}} \right)^{n_1} \cdot t \right) \right\}^{\frac{1}{1-n\ /2}} \qquad n_1 \neq 2 \tag{3-12}$$

Fracture initiation takes place when the half-crack length (*a*) has received a critical length of $a = a_{cr}$. The critical crack length can be calculated by taking into account Eq. (3-5) and Eq. (3-6):

$$\frac{K_I}{K_{IC}} = \frac{\sigma \cdot \sqrt{a_{cr} \cdot \pi}}{K_{IC}} = 1 \quad => \tag{3-13}$$

$$a_{cr} = \frac{K_{IC}^2}{\sigma^2 \cdot \pi} \tag{3-14}$$

The time needed ($t = t_{cr}$) for a crack to extend subcritically from its initial length to its critical length can then be calculated by incorporating Eq. (3-14) into Eq. (3-12) and by solving for time:

$$t_{cr} = \left(\left(\frac{K_{IC}}{\sigma} \right)^{\frac{2}{1-n_1/2}} \cdot \left(\frac{1}{\pi} \right)^{\frac{1}{1-n_1/2}} - a_0^{1-n_1/2} \right) \cdot \frac{1}{1-n_1/2} \cdot \frac{1}{B_1} \cdot \left(\frac{K_{IC}}{\sigma\sqrt{\pi}} \right)^{n_1} \qquad n_1 \neq 2 \tag{3-15}$$

3.2 Subcritical crack growth in shear

In the previous section, the simplest case of a crack under pure Mode I (tensile) loading, when the crack extends along its original plane, was presented. However, in rock masses, tri-dimensional compressive Mixed-mode loading conditions are more common. Atkinson (1984) refers to the literature and he argues that there is no obvious physico-chemical reason that the form of the constitutive equations presented to describe SCG should depend on the displacement mode on the crack tip. In the absence of evidence to the contrary, it is, therefore, assumed that the statements made regarding subcritical tensile crack propagation hold for all three fundamental modes of loading. Based on laboratory observations Kodama et al. (2001) concluded that the behaviour of deformation and micro-fracturing under tension in creep tests is similar to that under compression.

Charles's formulation Eq. (3-2) to describe the $v-K$ dependency of SCG is mainly used for Mode I loading conditions. Its use for Mode II problems is discussed by Atkinson (1984) and Kemeny (1993). The SCG model for a Mode II loading is conducted here in a similar manner as presented for Mode I loading. The crack velocity in Mode II loading condition is defined by:

$$v_2 = B_2 \cdot \left(\frac{K_{II}}{K_{IIC}} \right)^{n_2} \qquad (3\text{-}16)$$

where v_2 is the crack velocity for Mode II SCG, B_2 is the SCG constant, n_2 is the stress corrosion index, K_{II} is the stress intensity factor and K_{IIC} is the Mode II fracture toughness, respectively.

In the presented model, the stress intensity factors are essential parameters for the SCG velocity and time-to-failure (TTF) calculations. In the next section, an example is presented for a horizontal crack under pure Mode I loading conditions. Analytical solutions are available to calculate the stress intensity factors for an inclined crack in some simple loading configurations involving Mixed-mode I-II loading. As described in Chapter 2, the critical combination of stress intensity factors for different loading modes must be defined by a fracture criterion in order to calculate the direction of crack propagation and the magnitude of the applied stress for crack extension. In practice, besides a suitable fracture criterion a numerical approximation is needed to describe the crack stability in Mixed-mode conditions involving shear movement and frictional forces on the fracture surface. In the next chapter, such a criterion and a code are presented. The SCG model is incorporated in the code in Section 4.5 and is used to evaluate the delayed failure of rock specimens (Chapter 7) as observed in low loading rate compression tests in the laboratory (Section 5.2.4).

3.3 An example of application of Charles law in tension

To illustrate the described concept we consider a single crack of $2a_0$ = 10 mm subjected to a far-field tensile stress of 15 MPa as shown in Fig. 2-1a. The fracture toughness is K_{IC} = 2.74 MPam$^{1/2}$, and the applied SCG parameters are n_1 = 48 and $-\log A_1$ = 23.92 (Table 5-2).

Figure 3-1 illustrates the stress intensity factor versus the crack velocity using Eq. (3-2) and the fracture parameters defined for the Äspö diorite (Backers et al. 2006a). The range of velocities that is possible to measure in the laboratory with current techniques are often needed in the analysis. The dotted line in Fig. 3-1 shows the extrapolated curve for the out-of-range velocities and K_{I0} is the unknown stress corrosion limit.

To express the sensitivity to parameters *n* and *A*, two additional curves are presented in Fig. 3-1 for two values of *n* and *A*. When *n* is large, only minor SCG occurs at low levels of the applied load. When *n* is small, crack growth in significant amounts occurs at stress levels far below the short-term theoretical strength. Thus, the lower the value of *n,* the greater is the delayed characteristic of the breakage phenomena. Parameter *A* is a constant locating the curves on the stress intensity axis.

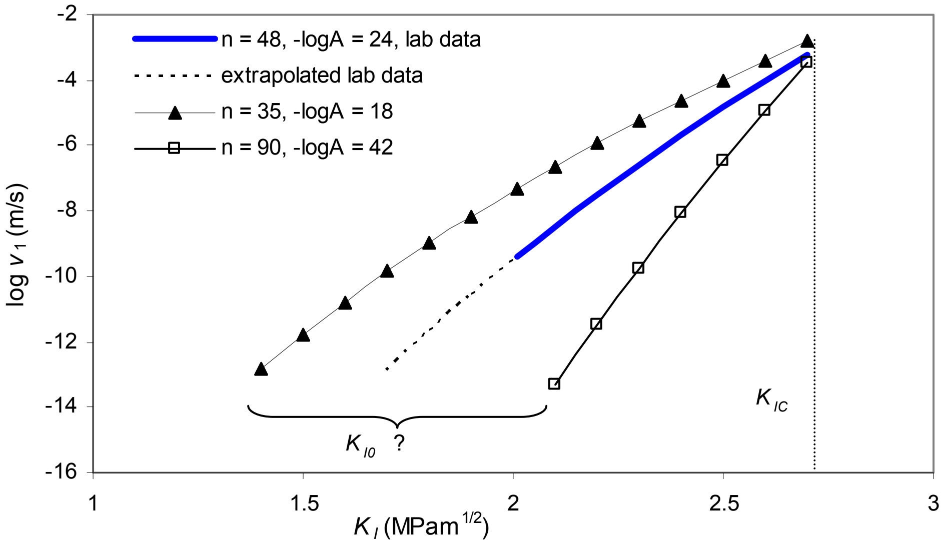

Figure 3-1. *The K_I versus log(v_I) relationship for the Äspö diorite.*

By applying Eq. (3-6) we obtain a stress intensity factor K_I of 1.88 MPam$^{1/2}$. According to Eq. (3-5), no unstable fracture propagation will occur and the crack is expected to extend subcritically.

Equation (3-15) presents the relationship between the initial half-crack length and the time it takes for a crack to grow to its critical length under static far-field stress (Fig. 3-2).

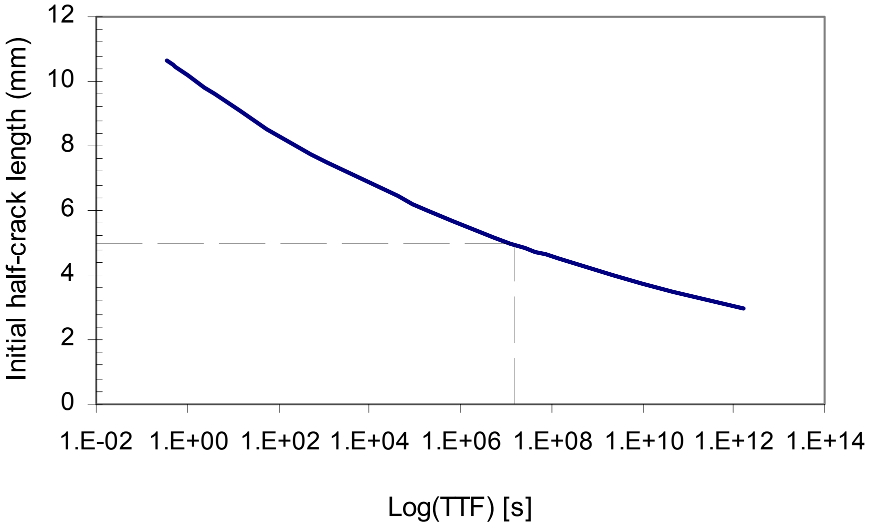

Figure 3-2. *Time to failure versus initial half-crack length. Horizontal cracks with initial half-crack lengths (a_0) between 3 and 11 mm are subjected to a uniaxial tensile stress of 15 MPa.*

Figure 3-3 presents the time-dependent half-crack length for the example crack ($a_0 = 5$ mm). The crack extends very slowly at the start and accelerates as the crack grows and the stress intensity at the crack tip increases. The critical half-crack length for unstable crack propagation can be calculated using Eq. (3-14), resulting in $a_{cr} = 10.6$ mm. The example crack starts to propagate in an unstable manner after 1.5 × 10^7 s (~ 0.48 years).

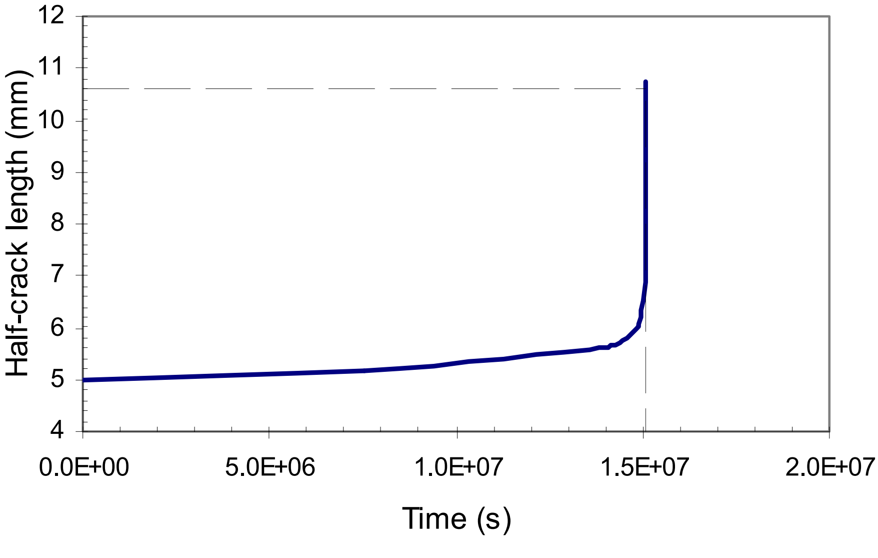

Figure 3-3. *Time versus half-crack length.*

When the stress intensity factor is close to its critical value, as depicted in Fig. 2-6, the crack velocity is a rough estimation. However, the approximation of the time for unstable crack propagation is reasonably accurate as the time spent in Regions 2 and 3 is usually short (Wilkins 1980).

4 FRACTURE PROPAGATION CODE, FRACOD

This chapter aims to describe the basic functions of FRACOD, and how it models the failure process of brittle rocks. FRACOD is a two-dimensional model based on the Displacement Discontinuity Method (DDM) principles. The DDM method belongs to the family of Boundary Element Methods (BEM). The DDM was initially developed by Crouch (1976) and later widely used in rock mechanics (Whittaker et al. 1992; Bobet and Einstein 1998b; Napier and Malan 1997; Napier 1999). A rock discontinuity (grain boundary, crack, joint, fracture, etc.) is simulated by using DDM elements to simulate the opposite surfaces of the discontinuity. The advantage of DDM in simulating fracture propagation, compared with other boundary element techniques, is its direct presentation of the fracture as fracture elements, without considering the separated fracture surfaces. FRACOD, previously named BEMF, was first presented by Shen (1993). Since its first publication, it has been continuously developed to model various fracture mechanics problems. The model predicts the fracturing process, including fracture initiation, fracture sliding/opening and fracture propagation. Both shear and tensile failure of the continuum medium are considered.

The software has been applied to a wide range of analyses including: modelling of fracture propagation observed in laboratory tests (Shen and Stephansson 1993b), rock indentation (Tan 1996), rock stability related to nuclear waste repositories (Shen and Stephansson 1996a, 1996b; Rinne 2000; Stephansson et al. 2003; Rinne et al. 2003b, 2003c; Lee and Jing 2003; Lee et al. 2006), borehole breakouts (Shen et al. 2002, 2004a, 2004b; Backers et al. 2006b) and numerical simulations of the compressive strength test (Rinne et al. 2006; Rinne and Shen 2007). Today, the software has the capacity to simulate acoustic emission (AE) events, change in rock mass permeability, effects of static fluid pressures and multi-regional rock domain analysis. For a more detailed description of these features, the reader is referred to the FRACOD (Ver 2.21) User's Manual (Shen et al. 2006).

4.1 Fracture propagation and the F-criterion

The original G-criterion of Griffith (1920) states that when the strain energy release rate in the direction of the maximum G-value reaches the critical value G_C, the fracture tip will propagate in that direction. The G-criterion does not distinguish between Mode I and Mode II fracture toughness of energy (G_{IC} and G_{IIC}).

Both tensile (Mode I) and shear failure (Mode II) mechanisms are common in rock masses. The G-criterion has been improved and extended by Shen and Stephansson (1993a) to include both Mode I and Mode II fracture propagation. They suggested a fracture propagation criterion, the F-criterion, which states that in an arbitrary direction (θ) at a fracture tip the F-value is calculated as:

$$F(\theta) = \frac{G_I(\theta)}{G_{IC}} + \frac{G_{II}(\theta)}{G_{IIC}} \qquad (4\text{-}1)$$

where G_{IC} and G_{IIC} are the critical strain energy release rates for Mode I and Mode II fracture propagation, respectively. $G_I(\theta)$ and $G_{II}(\theta)$ are the respective strain energy release rates due to the potential Mode I and Mode II fracture growth of a unit length. If the maximum F-value reaches 1.0, fracture propagation will occur.

The direction of fracture propagation will correspond to the direction where F reaches its maximum value. The sum of normalised G-values in the F-criterion is used to determine the failure load and its direction. G_I and G_{II} can be expressed as shown in Fig. 4-1. If a fracture grows a unit length in an arbitrary direction and the new fracture opens without any surface shear dislocation, the strain energy loss in the surrounding body due to the fracture growth is G_I. Similarly, if the new fracture has only a surface shear dislocation and no opening in the normal direction, the strain energy loss is G_{II}.

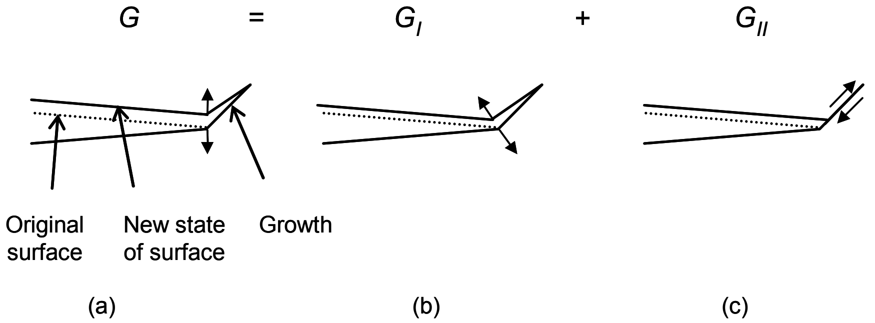

Figure 4-1. *Definition of G_I and G_{II} for fracture growth. (a) G: the growth has both open and shear displacement; (b) G_I: the growth has only normal displacement showing increase in aperture; (c) G_{II}: the growth has only shear displacement (Shen and Stephansson 1993a).*

4.2 Fracture propagation using DDM

The key step in using the F-criterion is to determine the strain energy release rate in Mode I (G_I) and Mode II (G_{II}) at a given fracture tip. As G_I and G_{II} are only the special cases of G, the task is then how to use the DDM to calculate the strain energy release rate G. G is the change of the strain energy in a linear elastic body when the crack has grown one unit of length. Therefore, to obtain G, the strain energy must first be estimated. By definition, the strain energy W in a linear elastic body is:

$$W = \iiint_V \tfrac{1}{2}\sigma_{ij}\varepsilon_{ij}\,dV \tag{4-2}$$

where σ_{ij} and ε_{ij} are the stress and strain components, and V is the volume of the body. The strain energy can also be calculated from the stresses and displacements along the boundary of the body:

$$W = \tfrac{1}{2}\int_S (\sigma_s u_s + \sigma_n u_n)\cdot ds \tag{4-3}$$

where σ_s, σ_n, u_n, u_s are the stresses and displacements in tangential and normal directions along the boundary of the elastic body (Crouch and Starfield 1983). By applying Eq. (4-3) to the crack system in an infinite body with far-field stresses in the shear and normal directions of the crack, $(\sigma_s)_0$ and $(\sigma_n)_0$, the strain energy per unit thickness can be written as:

$$W = \tfrac{1}{2}\int_0^a \left[\left(\sigma_s - (\sigma_s)_0\right)D_s + \left(\sigma_n - (\sigma_n)_0\right)D_n\right]\cdot da \tag{4-4}$$

where a is the crack length, D_s is the shear displacement discontinuity and D_n is the normal displacement discontinuity of the crack. When DDM is used to calculate the stresses and displacements of a series of crack elements, the strain energy can also be written in terms of the element length (a^i) and the stress and displacement at the i^{th} element of the crack where *m* is the total number of the DDM elements:

$$W \approx \frac{1}{2}\sum_{i=1}^{m}\left(\overset{i}{a}\left(\overset{i}{\sigma}_s-\left(\overset{i}{\sigma}_s\right)_0\right)\overset{i}{D}_s+\overset{i}{a}\left(\overset{i}{\sigma}_n-\left(\overset{i}{\sigma}_n\right)_0\right)\overset{i}{D}_n\right) \tag{4-5}$$

Based on the strain energy in an arbitrary direction (θ), *G* can be estimated:

$$G(\theta)=\frac{\partial W}{\partial a}\approx\frac{\left[W(a+\Delta a)-W(a)\right]}{\Delta a} \tag{4-6}$$

where *W(a)* is the strain energy of the original crack while $W(a + \Delta a)$ is the strain energy of the original crack with its small fictitious extension, Δa (Fig. 4-2). Both *W(a)* and $W(a + \Delta a)$ are determined by using DDM and Eq. (4-6).

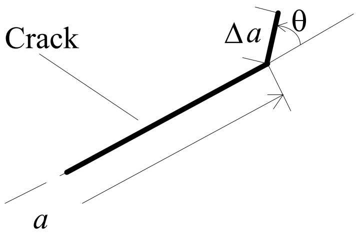

Figure 4-2. *A fictitious element of length Δa in the θ direction is introduced to the tip of the original crack (Shen and Stephansson 1993a).*

If the shear displacement of the fictitious element is restricted numerically to zero, the result obtained using Eq. (4-6) will be $G_I(\theta)$. Similarly, if the normal displacement of the fictitious element is set to zero, the result obtained will be $G_{II}(\theta)$. After obtaining both $G_I(\theta)$ and $G_{II}(\theta)$, the F-value in Eq. (4-1) can be calculated using the given fracture values G_{IC} and G_{IIC} for a given rock type.

The original Griffith G-criterion does not take into account the frictional effect at the fracture tip. In the DDM approximation, friction on the fracture surface is also included in the energy change.

The opposite faces of the discontinuity may or may not be stress free. The state of each discontinuity element is controlled by the Mohr-Coulomb failure criterion as follows:

(1) open discontinuity: $\sigma_n > 0, \sigma_s = 0$ (4-7)
(2) elastic discontinuity: $\sigma_n < 0, |\sigma_s| < c_f + |\sigma_n| \tan\phi_f$ (4-8)
(3) sliding discontinuity: $\sigma_n < 0, |\sigma_s| \geq c_f + |\sigma_n| \tan\phi_f$ (4-9)

where a compressive stress is taken to be negative and c_f is the cohesion and ϕ_f is the friction angle. If the crack has experienced sliding, the cohesion term is set to $c_f = 0$.
When two crack surfaces are in elastic contact, the magnitude of stresses on the crack surface will depend on the crack stiffness (K_S, K_N) and the displacement discontinuities:

$$\overset{i}{\sigma}_s = K_S\,\overset{i}{D}_s \tag{4-10}$$

$$\overset{i}{\sigma}_n = K_N \overset{i}{D}_n \tag{4-11}$$

For an open crack, the stresses on the crack surfaces are zero and the crack stiffness is not accounted. For a sliding crack surface the governing equations take into account the friction and the normal stiffness (K_N), however, the shear stress is no longer related to shear stiffness (K_S).

The normal and shear displacements and fracture aperture is calculated using the given fracture stiffness properties. When the dilation angle of a crack (ϕ_d) is considered, the additional stress caused by the dilation is calculated by:

$$\Delta \overset{i}{\sigma}_n = K_N \overset{i}{D}_s \tan \phi_i \tag{4-12}$$

Increasing the dilation angle will increase the crack normal stress and result in increased friction resistance.

4.3 Iteration process

The Boundary Element Method (including the DDM) is an implicit numerical method. This means that the numerical calculation will only provide the final solution at the given stress or displacement boundary conditions, ignoring the process that reaches the final solution. For elastic problems, the implicit method is an efficient way to obtain the final solution due to the linear stress-strain relationship. In a plasticity problem caused by crack sliding and fracture propagation, however, the implicit method could give false results because the final solution will depend on the loading path. An iteration process is an effective method to consider the stress or displacement path-dependent problems (Shen et al. 2006).

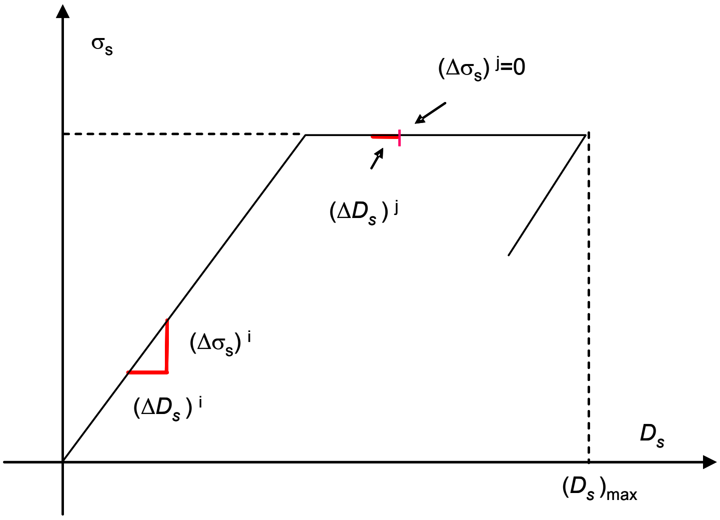

Figure 4-3. *Iteration process to simulate a complex loading path (Shen et al. 2006).*

Consider a joint element simulated by FRACOD (Fig. 4-3). The joint element is initially loaded in shear up to the maximum shear strength $(\sigma_s)_{max}$. It then slides with the same shear stress to a specified maximum displacement $(D_s)_{max}$ and thereafter it is unloaded. We assume that the loading process is displacement controlled. The total maximum shear displacement of a discontinuity is subdivided into small increments such as $(\Delta D_s)^i$ and $(\Delta D_s)^j$. The corresponding increment in shear stress $(\Delta\sigma_s)^i$ and $(\Delta\sigma_s)^j$ can be calculated depending upon the state of the joint element. If the joint element is still elastic such as at increment *i*, the shear stress increment is:

$$(\Delta\sigma_s)^i = K_S(\Delta D_s)^i \tag{4-13}$$

If the joint element is sliding such as at increment *j*, the shear stress increment is:

$$(\Delta\sigma_s)^i = 0 \tag{4-14}$$

The state of the joint element is determined by the total shear stress, which is the sum of the individual stress increments during the previous loading path. For example,

$$(\sigma_s)^i = \sum_{n=1,i} (\Delta\sigma_s)^n \tag{4-15}$$

$$(\sigma_s)^j = \sum_{n=1,j} (\Delta\sigma_s)^n \tag{4-16}$$

If the i^{th} increment $(\sigma_s)^i < (\sigma_s)_{max}$, the joint element is in an elastic condition. If the j^{th} increment $(\sigma_s)^j = (\sigma_s)_{max}$, the joint element is sliding.

In FRACOD modelling, the joint element is assumed to be initially elastic in the first increment. When the resultant total shear stress is greater than the shear strength at any given increment cycle, the joint element is identified to be sliding. In the next incremental cycle, the incremental joint shear stress will be recalculated using the sliding joint conditions.

The incremental shear and normal displacement of each joint and boundary element are recorded and accumulated in each incremental cycle. Their final values will be obtained using the iteration method. After knowing the displacement of the discontinuities, the stresses and displacement at any internal point of the model can be calculated.

During the process of detecting the possibility and the direction of the potential fracture propagation, a fictitious crack element is added to the candidate crack tip in different directions. For each possible fracture propagation direction, a complete iteration process from the beginning of the loading is required to obtain the necessary stress/displacement values of the discontinuity and boundary elements to determine the F-value. This would be time consuming and theoretically incorrect because it assumes that the fictitious element has existed from the beginning of the loading. An alternative approach has been developed to simulate the fracture propagation using an iteration process and by decomposing the problem into two stages as shown in Fig. 4-4.

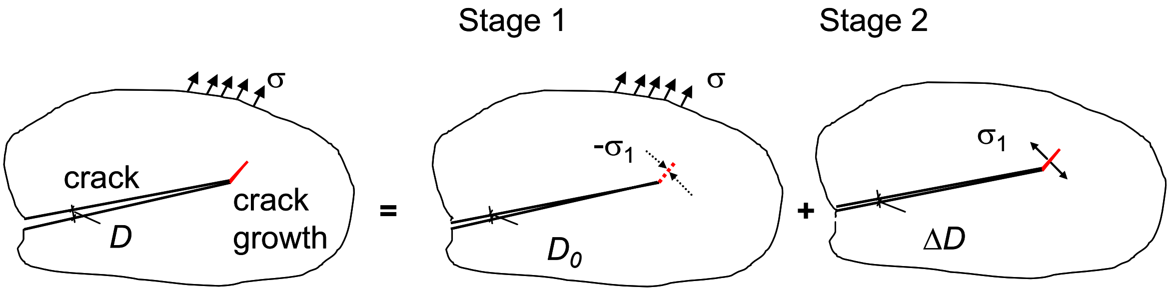

Figure 4-4. *Decomposition of a crack growth problem for modelling using Mode I crack growth iteration (Shen et al. 2006).*

We consider a single crack tip in a finite body under an external stress σ. The crack has grown by one element length in a given direction. The problem can be decomposed into two stages as shown in Fig. 4-4. In Stage I, the existing crack and its fictitious growth element are subject to an external stress σ. The growth element is applied to a high stress $-\sigma_1$ so that the displacement at the element is zero. Here σ_1 should be equal to the stress at the element centre calculated by considering the pre-existing crack only. This stage is equivalent to a case where the growth element does not exist. In Stage 2, the existing crack and its growth element are free of external stress. Only the growth element is subjected to the internal stress σ_1. In this treatment, the total resultant stress at the growth element is the sum of $-\sigma_1$ (Stage 1) and σ_1 (Stage 2), i.e. zero. This is expected for Mode I fracture propagation.

For Mode II fracture growth, the surfaces of the growth element are in contact; therefore, no ‘bonding’ stress is required at Stage 1. At Stage 2, an additional shear stress is applied to the growth element equal to the difference between the total resultant shear stress at Stage 1 and the shear strength.

In the two cases, the crack geometry is kept the same in the superposed stages, and only the stresses are decomposed. In both cases, Stage 1 is equivalent to the case without crack growth. It hence can be modelled by the standard iteration method. When crack growth occurs, only one additional iteration step is needed to model Stage 2. This can be done by adding the growth element to the existing fracture system and applying the specified stresses to this element.

4.4 New crack formation

The FRACOD software was originally designed to simulate fracture propagation from a few predefined pre-existing fractures. Because FRACOD considers the 'intact rock' as a flawless and homogeneous medium, the stress concentrators have to be introduced in the model before discontinuous modelling can start. For FRACOD models, the term 'new crack formation' is used to cover the 'microstructural' processes leading to macro-crack formation and it is separated from 'fracture initiation' that occurs from an existing (macro) crack tip, see definition by Bieniawski (1967) in Section 2.1.

When the crack extends subcritically, a new element is introduced to the tip of the original crack, as will be explained in Section 4.5. Such crack propagation is called here 'subcritical crack growth', SCG.

When the crack is subjected to a critical stress state for fast crack propagation ($K = K_C$), a new element is introduced on the crack tip. If the fracture propagation ceases after the introduction of the new crack tip element, it is referred to here as 'stable fracture propagation'. For 'unstable fracture propagation', the crack will extend without an additional applied load after the critical level of stress for fracture propagation has been reached.

In a rock, the stress distribution on the grain scale is likely to be very complex. It is difficult to model explicitly how and when the microstructural processes start to create a new crack surface in a complex medium, because models cannot consider all details of the rock structure. Considerable generalisations and assumptions have to be made. Instead of describing the micro-scale process in detail, the FRACOD model defines those locations with the greatest potential for new crack formation at a given stress state. In FRACOD, 'newly formed cracks' reflect a critical stress concentration caused by grain boundaries, micro-cracks, pre-damage and other defects in real rock matrix. The location of these newly formed cracks mirrors the potential regions of micro-cracking and rock material loosening, for example a drop in the cohesion of mineral grains. It must be noted that the new crack initiation process only identifies locations where the failure may start, not to the final failure process and structural breakdown. The F-criterion controls whether or not these new cracks propagate and in which direction.

4.4.1 Critical stress state and direction for newly formed cracks

New crack formation depends upon the stress/strength ratio β, as presented in the next section. When the tensile stress at a given point in the model exceeds some predefined portion of the tensile strength σ_t of the intact rock, a potential failure surface will be introduced in the model with a direction perpendicular to the tensile stress. Similarly for shear failure, both the cohesion and the friction angle of the intact rock are used to define the direction of the potential failure plane according to the Mohr-Coulomb criterion. New fracture initiation in tension is defined as follows:

$$\sigma_{tensile} \geq \sigma_t \tag{4-17}$$

Direction of fracture initiation in tension:

$$\theta_{\mathrm{it}} = \theta(\sigma_{\mathrm{tensile}}) + \pi/2 \tag{4-18}$$

where $\sigma_{tensile}$ is the principal tensile stress at a given point, σ_t is the tensile strength of the intact rock, θ_{it} is the direction of the fracture initiation in tension, and $\theta(\sigma_{tensile})$ is the direction of the tensile stress.

New crack formation in shear occurs when:

$$\sigma_{shear} \geq \sigma_n \tan(\phi_i) + c_i \tag{4-19}$$

Direction of the new crack is:

$$\theta_{is} = \phi_i/2 + \pi/4 \tag{4-20}$$

where σ_{shear} is the shear stress in the direction of θ_{is}, σ_n is the normal stress to shear failure plane, ϕ_i is the internal friction angle of intact rock, c_i is the cohesion, and θ_{is} is the direction of potential shear failure, which is measured from the direction of the minimum principal stress.

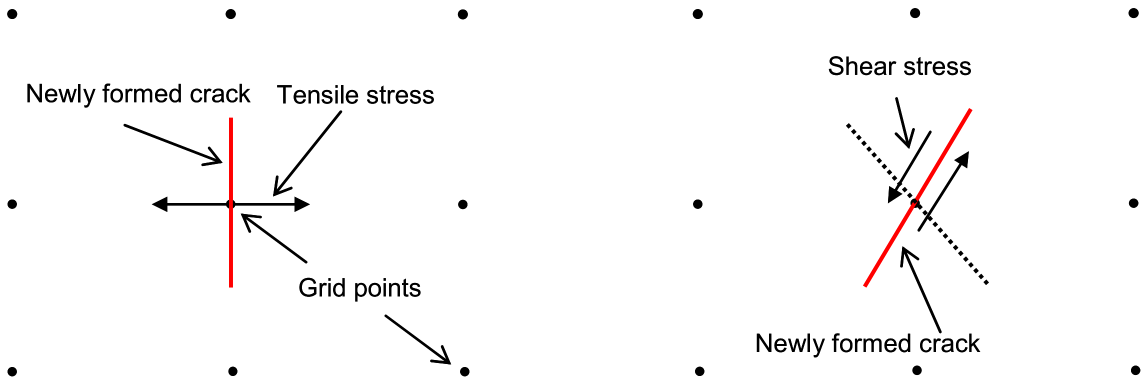

a) b)

Figure 4-5. *New crack formation: a) in tension; b) shear in intact rock (Shen et al. 2006).*

Because there are always two symmetric shear failure planes, two potential fracture planes are considered, but only the fracture direction that causes the maximum energy release is added to the model. In real rock, the new fractures are often curved or kinked. It is unlikely that they will experience large shear displacement during fracture propagation in a limited region (Shen in Rinne et al. 2003a). Therefore, it is considered that the peak fracture strength rather than the residual strength applies to these fractures. Intact rock strength properties (c_i and ϕ_i) are usually applied in newly formed cracks. When the local stress exceeds the strength of such a crack plane, it will slip or open and its cohesion drops to zero (residual strength). For pre-existing cracks, lower strength properties (c_f and ϕ_f) compared with newly formed cracks are usually applied.

Once the failure of a new introduced crack plane occurs, i.e. slipping or opening, the newly formed crack is treated in the same way as a pre-existent crack. The subsequent propagation is controlled according to the F-criterion, as explained in Section 4.2. The size and the density of the newly formed cracks are input parameters in the model. The new crack formation is only defined for models of finite area. Crack size, crack density and uncertainties related to modelling of newly formed cracks will be discussed in Chapter 8.

4.4.2 Probability of new crack formation

The new crack formation can start at a stress level far below the ultimate short-term strength. Usually the probability of crack initiation increases with stress. FRACOD uses a probabilistic approach to simulate new crack formation. It is assumed that, at a candidate location for fracture initiation, the probability of a fracture initiation depends upon the stress/strength ratio (σ/σ_m):

$$p = 0\,; \qquad \text{if} \quad \left(0 \le \frac{\sigma}{\sigma_m} \le \beta \right) \tag{4-21}$$

$$p = \frac{1}{(1-\beta)^2}\left[\frac{\sigma}{\sigma_m} - \beta\right]^2; \qquad \text{if} \quad \left(\beta \le \frac{\sigma}{\sigma_m} \le 1.0 \right) \tag{4-22}$$

$$p = 1.0\,; \qquad \text{if} \quad \left(\frac{\sigma}{\sigma_m} > 1.0 \right) \tag{4-23}$$

where p is the probability of fracture initiation, σ/σ_m is the ratio of the stress to strength and β is fracture initiation level. An example of the probability of new crack formation as a function of the stress/strength ratio is presented in Fig. 4-6. Figure 6-26 illustrates how the new cracks are modelled to initiate in a rock specimen loaded under uniaxial compressive conditions. The probability of new crack formation can be considered as a consequence of the heterogeneity of rock with weaker and stronger minerals or mineral grain boundaries. The form of the probability curve (Eq. (4-22)) can be adapted when the actual crack initiation behaviour is known, for example when registered from AE curves.

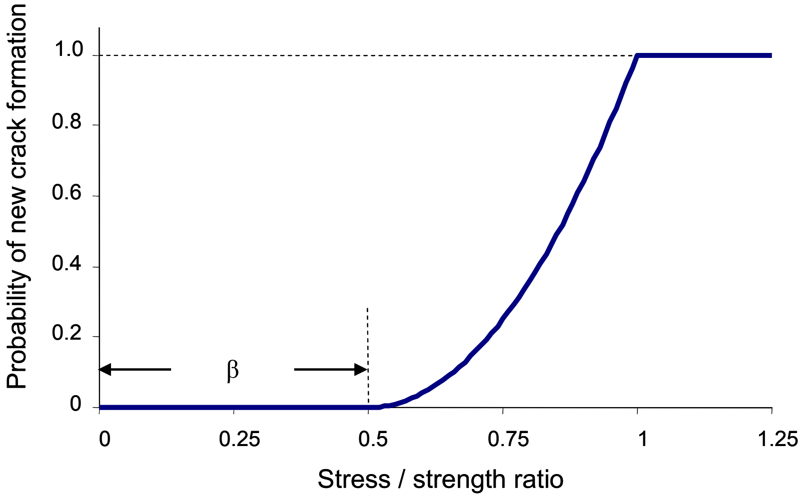

Figure 4-6. *Probability of new crack formation as a function of the stress and strength ratio. The probability of fracture propagation is plotted for β = 0.5 (Shen in Rinne et al. 2003a).*

4.5 Subcritical Crack Growth using FRACOD

Because the FRACOD software takes into account distinct fractures and explicitly models the fracture propagation, it is suitable for studying SCG. The concept presented in Chapter 3 is introduced in FRACOD using a calculation process as described below. The modifications of the code to implement the SCG concept were made by Dr Shen (Shen and Rinne 2007). As a first step, the software was developed to be able to monitor the stress and displacement history at any point in the model during the loading and unloading processes. This routine was needed to be able monitor the axial and lateral strain response of loaded rock specimens. Furthermore, code modifications were made to couple a time-marching algorithm and the SCG concept into the code. A time step Δt is used in the iteration. Figure 4-7 shows the SCG simulation process.

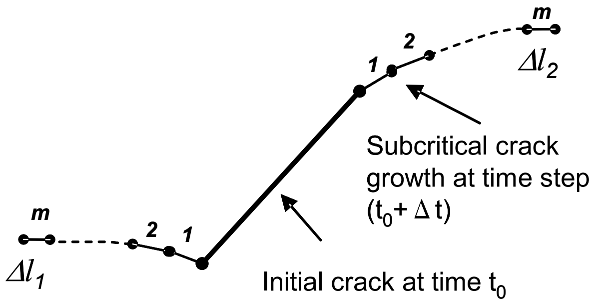

Figure 4-7. *Simulation of subcritical crack growth in FRACOD. The length of SCG (Δl) at the m^{th} time step ($t = t_0 + m\Delta t$) (Shen and Rinne 2007).*

The following calculation steps are performed:

Step 1: K_I and K_{II} are calculated at any given crack tip for the given loading condition and fracture configuration. The stress intensity factors are calculated from the strain energy release rates using the relationship between K and G, as discussed in Section 2.5. Subcritical crack velocities v_1 and v_2 are determined for the time t_0 from Eqs. (3-4) and (3-16). First the code determines which failure mode will occur at any given time and then it calculates the SCG velocity in the direction consistent with the failure mode.

Step 2: The length of SCG for a time step Δt is calculated:

$$\Delta l = v_1 \cdot \Delta t \text{ ; or } \Delta l = v_2 \cdot \Delta t \qquad (4\text{-}24)$$

for every crack tip.

Step 3: If the SCG length is equal to or greater than an element length, a new tip element is added to the crack. Otherwise, the length is temporarily stored in memory and accumulated in the subsequent time steps until it reaches one element length. Similar crack elements are used for SCG as described for (stable and unstable) fracture propagation. The length of the tip element is defined in the model set-up and it depends on the model accuracy requirements and the calculation capacity.

Step 4: Steps 1 to 3 are repeated using a new time step ($t_0 + N\Delta t$) until the specified end time is reached. N is the number of simulation cycles. If only one mode occurs, the total accumulated SCG length is for this mode only. If Mixed-mode occurs, the accumulated length is a mix of Mode I SCG and Mode II SCG. When the direct distance between the starting point (crack tip) and the finishing point is greater than the element length, then a new element is added. Hence, the direct distance is not necessarily the total SCG length because the path of a mixed mode crack growth can be a zigzag shape.

The size of each time step is defined based on the ratios K_I/K_{IC} or K_{II}/K_{IIC} to minimise the iteration cycles needed to reach the specified end time. When the ratio is low (K_I/K_{IC} or K_{II}/K_{IIC} << 1.0), the SCG speed is low; hence the time step can be larger. When the ratio is close to 1.0, the SCG speed is high; hence higher accuracy is needed and the time step must be smaller. The minimum and maximum lengths for a time step (Δt) and the total time (time span, T_{tot}) are given as input values. In addition to the parameters needed for non-time-dependent calculations, the time-dependent calculations require the SCG parameters n_1, n_2, B_1 and B_2.

5 LABORATORY EXPERIMENTS ON ÄSPÖ DIORITE

Several studies on radioactive waste management research have been carried out at the SKB's (The Swedish Nuclear Fuel and Waste Management Co.) underground Hard Rock Laboratory (HRL), Äspö, South-Eastern Sweden. As a result of continuous research and several laboratory programmes since late 1980, an extensive database of geological and geomechanical data exists[1]. This chapter summarises the laboratory data on the Äspö diorite that is of importance for failure analysis using the fracture mechanics approach.

For the CREEP-project (Rinne 2003), well-documented laboratory test cases were needed for two reasons: to provide appropriate input data for modelling and to compare the real rock behaviour with results from the numerical simulations (Rinne 2005). This section summarises the Strain Rate Stepping test performed to characterise the time-dependent behaviour of the compressed and saturated Äspö diorite (Antikainen 2007). Also, procedures to determine the input parameters for time-dependent calculations are described (Backers 2006). The modelling work presented in Chapters 6 and 7 are mainly based on results from these experiments.

5.1 Äspö diorite

A full-scale Äspö Pillar Stability Experiment (APSE) was carried out at the Äspö HRL. In the experiment, stress-induced brittle failure was monitored in a pillar between two large boreholes (Andersson et al. 2003, Andersson 2007). The rock characterisation programme made at the drift excavated for the APSE experiment is reported by Staub et al. (2004).

The results from the test site at 450 m depth show that the APSE tunnel is situated in an area dominated by different varieties of the Äspö diorite (Magnor 2004). The geology in the test area is fairly complex, partly due to the proximity of a main shear zone running along the test tunnel. The major rock volume consists of unaltered diorite, but relatively large volumes contain oxidised, sheared or mylonitic varieties of the Äspö diorite. The age of typical Äspö diorite is about 1800 million years, which corresponds to the crystallisation age of the rock.
The unaltered Äspö diorite (Figs 5-1 and 5-2) is a medium-grained, dark grey to dark reddish grey rock, generally porphyritic with megacrysts of red feldspar. The diameters of the K-feldspar porphyroclasts are between 1 and 2 cm (Lampinen 2006). The unaltered Äspö diorite, together with granite, is the dominant rock type in the Äspö HRL, especially at the deeper levels.

---

[1] Many of SKB's research reports referred to in this thesis are available on the SKB's web page (www.skb.se).

Figure 5-1. *Typical unaltered Äspö diorite (Staub et al. 2004).*

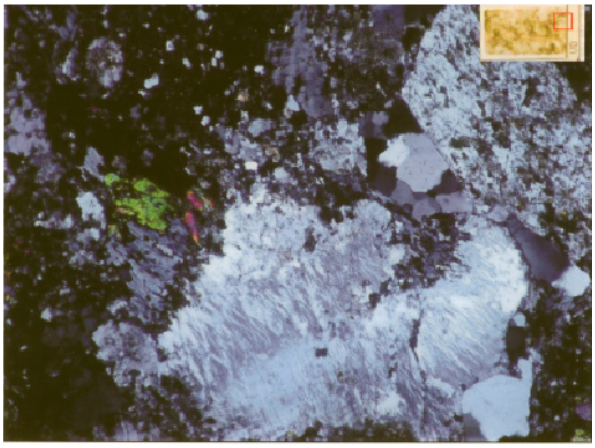

Figure 5-2. *Unaltered Äspö diorite in polarised light. The feldspar grain has flame-like perthite lamellae. The width of the image is 4 mm (Lampinen 2006).*

Figure 5-3. *Oxidised Äspö diorite (Staub et al. 2004).*

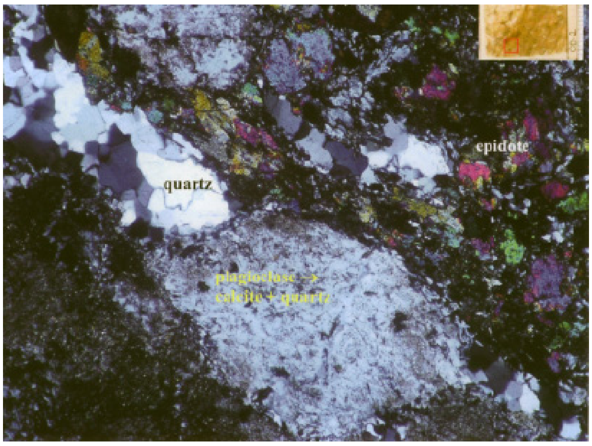

Figure 5-4. *Oxidised Äspö diorite in polarised light. Altered plagioclase crystals and quartz porphyroclasts. The width of the image is 4 mm (Lampinen 2006).*

The oxidised variety of the Äspö diorite (Figs 5-3 and 5-4) is red to greyish in colour. It is mainly restricted to areas bordering the shear zone. It usually constitutes a transition from the shear zone rock to the unaltered Äspö diorite. Almost 20% of the APSE tunnel is built in this rock type. In general, there is a gradual change between oxidised and unaltered Äspö diorite. This change can happen within 5 cm or it might be unclear for tens of centimetres.

The plagioclase constitutes approximately 50% of the mineralogical composition of the Äspö diorite. The rest is mainly quartz, biotite and K-feldspar. From analysis of thin sections, the grain size variation in both unaltered and oxidised rock is very similar (see Fig. 5-5a and b). Detailed information about minerals in thin sections from the test area is reported by Lampinen (2006). According to Backers (2005), the average grain size of the Äspö diorite at the APSE site is 1.28±1.61 mm (Fig. 5-6).

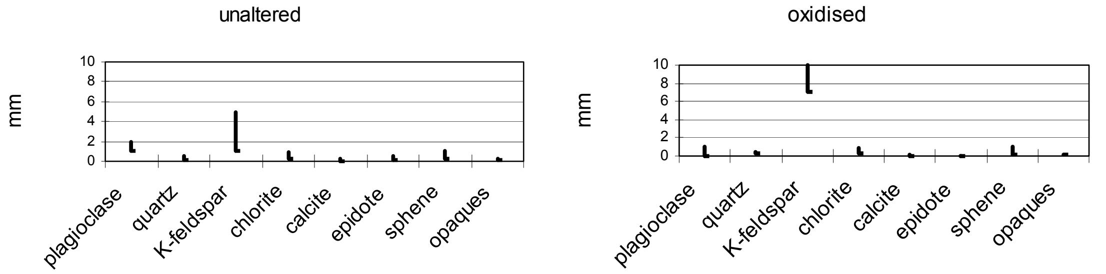

Figure 5-5. *Grain size of the different minerals. a) Unaltered and b) oxidised Äspö diorite (Lampinen 2006).*

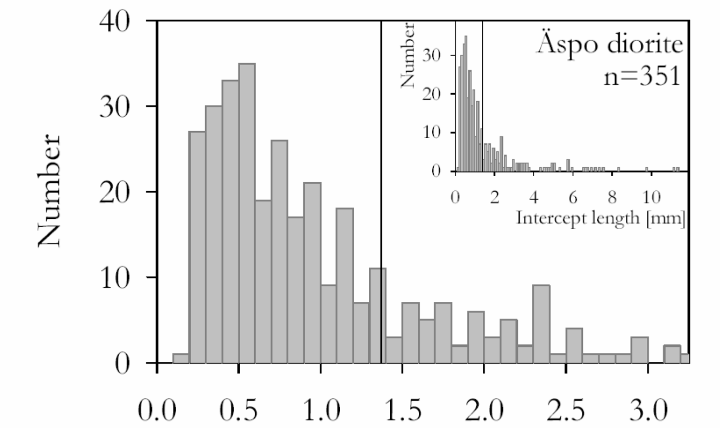

Figure 5-6. *Grain size distribution of the Äspö diorite. Arithmetic mean grain diameter as determined from intercept length (mm) measurements is indicated by a vertical line. Data were taken in two perpendicular directions, showing no anisotropy (Backers 2005).*

The modal analyses from thin sections have been recently performed in order to classify and characterise the different rock types from drill holes at SKB's site investigation area in Oskarshamn. The rock cores were taken also from drill cores at Äspö HRL (Janson et al. 2007). According to the Streckeisen classification, the rock type at the APSE site is mainly classified as granite or granodiorite. According to SKB's rock-type classification, the Äspö diorite with a high content of quartz is called Ävrö granite.

5.2 Tests on intact rock

Rock samples of the Äspö diorite were selected from three boreholes (KF0066A, KA3376B and KF0069A) drilled in the rock volume of the APSE experiment. The drill core sections were selected to be able to group the prepared specimens into six 'samples'. For each 'sample', four specimens were selected as close as possible from the same drill core considering the visible heterogeneity of the rock. For the six samples, the following four tests were carried out: (i) the Uniaxial Compressive Strength test (UCS test), (ii) the Brazilian test, (iii) the standard Triaxial

Compression Test (Triax test), and (iv) the slow-loading rate triaxial Strain Rate Stepping (SRS) test. These tests were performed at the Helsinki University of Technology (HUT).
All specimens were prepared and tested according to the respective ISRM Suggested Method (ISRM 1981). The tests were run using a digitally servo-controlled MTS 815 rock mechanics test system. An additional description of laboratory procedures and equipment to investigate the stress-strain behaviour (except for the SRS test) at HUT is reported by Hakala and Heikkilä (1997) and Hakala et al. (2005).

The boreholes, samples, specimens and test results are summarised in Table 5-1. A specimen is named according to its location along the borehole. For example, a UCS test performed on a specimen located 26.40 m from the start of the borehole is termed U2640; Triax tests are indicated by the prefix T, and SRS tests by S, respectively.

The rock referred to here as the Äspö diorite encapsulates different varieties of rock and the tested specimens have not been classified in sub-domains in terms of unaltered, oxidised or mylonitic Äspö diorite. According to Janson et al. (2007), the drill cores KF0066A01 and KF0069A01 merely represent granite and granodiorite, and, according to SKB's classification system, based on Boremap, they should be called Ävrö granite. The geological documentation of core-drilled boreholes according to the Boremap method is based on the use of BIPS images of the borehole wall and the simultaneous study of the drill core (Samuelson et al. 2007).

Table 5-1. Intact rock test results of the Äspö diorite. Compiled from Antikainen (2007) and the CREEP-project database.

Borehole (BH)		**KF0066A**	**KF0066A**	**KF0066A**	**KF0066A**	**KA3376B**	**KF0069A**
Sample (nr)	Unit	1	2	3	4	5	6
UCS, intact rock properties and AE measurements and tensile strength							
Length along the BH / specimen ID	m	26.40	36.04	38.95	49.89	12.08	45.77
Uniaxial compressive strength	MPa	185.3	270.2	300.0	257.4	182.1	301.6
Density	kg/m^3	2720	2673	2683	2670	2743	2677
Young's modulus	GPa	61.6	70.1	69.9	70.4	63.0	71.2
Poisson's ratio	(-)	0.32	0.31	0.31	0.29	0.32	0.32
σ_{ci}(AE)	MPa	75	64	80	50	85	120
σ_{ci} (reversal of the volumetric strain)	MPa	110	163	170	130	118	180
σ_{ci}(AE)/UCS	%	40	24	27	19	47	40
σ_{ci}/UCS	%	59	60	57	51	65	60
Tensile strength [1]	MPa	11.1	17.1	14.9	16.6	13.5	18.1
Triaxial compressive strength test							
Length along the BH / specimen ID	m	22.01	35.16	38.38B	48.27	12.26 [2]	43.47
Confining pressure	MPa	7	2	7	2	7	2
Peak strength	MPa	265.3	268.6	373.0	316.0	270.6	372.9
Axial strain at peak stress	mm/mm	4.12E-03	3.95E-03	5.42E-03	4.58E-03	3.53E-03	5.36E-03
Critical inelastic axial strain	mm/mm	4.10E-04	3.20E-04	3.60E-04	3.80E-04	1.80E-04	4.70E-04
Density	kg/m^3	2728	2676	2674	2665	2733	2665
Young's modulus	GPa	69.6	71.2	71.8	73.1	70.6	74.2
Poisson's ratio	(-)	0.34	0.38	0.32	0.35	0.34	0.29
Strain Rate Stepping test							
Length along the BH / specimen ID	m	22.14	35.29	38.51	48.4	12.39 [2]	44.60
Confining pressure	MPa	7	2	7	2	7	2
Peak strength	MPa	238.4	245.9	342.0	271.2	194.8	321.3
Axial strain at peak stress	mm/mm	4.22E-03	3.60E-03	5.41E-03	4.48E-03	2.82E-03	4.38E-03
Critical inelastic axial strain	mm/mm	8.8E-04	4.0E-04	7.5E-04	4.4E-04	1.4E-04	3.3E-04
Density	kg/m^3	2730	2672	2675	2665	2738	2669
Young's modulus	GPa	69.7	75.8	74.4	72.1	71.3	77.3
Poisson's ratio	(-)	0.31	0.29	0.30	0.30	0.29	0.28

[1] The indirect tensile strength is determined from a specimen adjacent to the UCS test specimen.

[2] Uncertainties were reported in the testing procedure.

5.2.1 Tensile strength tests

Uniaxial (direct) tensile strength tests in the laboratory were planned to determine the SCG parameters of the Äspö diorite (Backers 2006). These tests, however, appeared to be difficult to perform, because failure usually occurred in the section connecting the specimen to the loading platens. To test the set-up and the methodology, a number of direct tensile tests were performed. The surface roughness of the specimen ends was about 100 µm. The end surfaces of the specimens were then glued to metal plates, which were connected to the loading machine.

Chains connected to the metal plates apply the tensile load to the specimen. During the experiments, failure occurred in the glue rather than in the specimen. Refining of the gluing procedure reduced the failure of the glue, but still more than 70% of the experiments failed at the glue. In light of the high failure rate of the glue, it was concluded that the direct tensile test is not a suitable method to determine the tensile strength of the Äspö diorite and SCG parameters according to Wilkins' (1980) method. The indirect Brazilian strength test and the three-point bending (3PB) test were performed instead, as described in Section 5.3.2.

Determination of the intact rock tensile strength using indirect methods is common due to difficulties in obtaining successful results by direct tests. The Brazilian test is often used to determine the indirect uniaxial tensile strength (Fig. 5-7). The justification for the test is based on the experimental fact that disc-shaped rock samples under a diametrical loading fail in tension. The tensile strength of the specimen, σ_t, is calculated by a formula involving the peak compressive load and the specimen dimensions. The indirect tensile strength of the Äspö diorite using Brazilian tests has been earlier reported by Nordlund et al. (1999).

For the CREEP-project, six Brazilian tests were performed to estimate the tensile strength of the Äspö diorite (Antikainen 2007). The saturated density, Young's modulus (E) and the Poisson's ration (ν) were also determined. The test results are listed in Table 5-1.

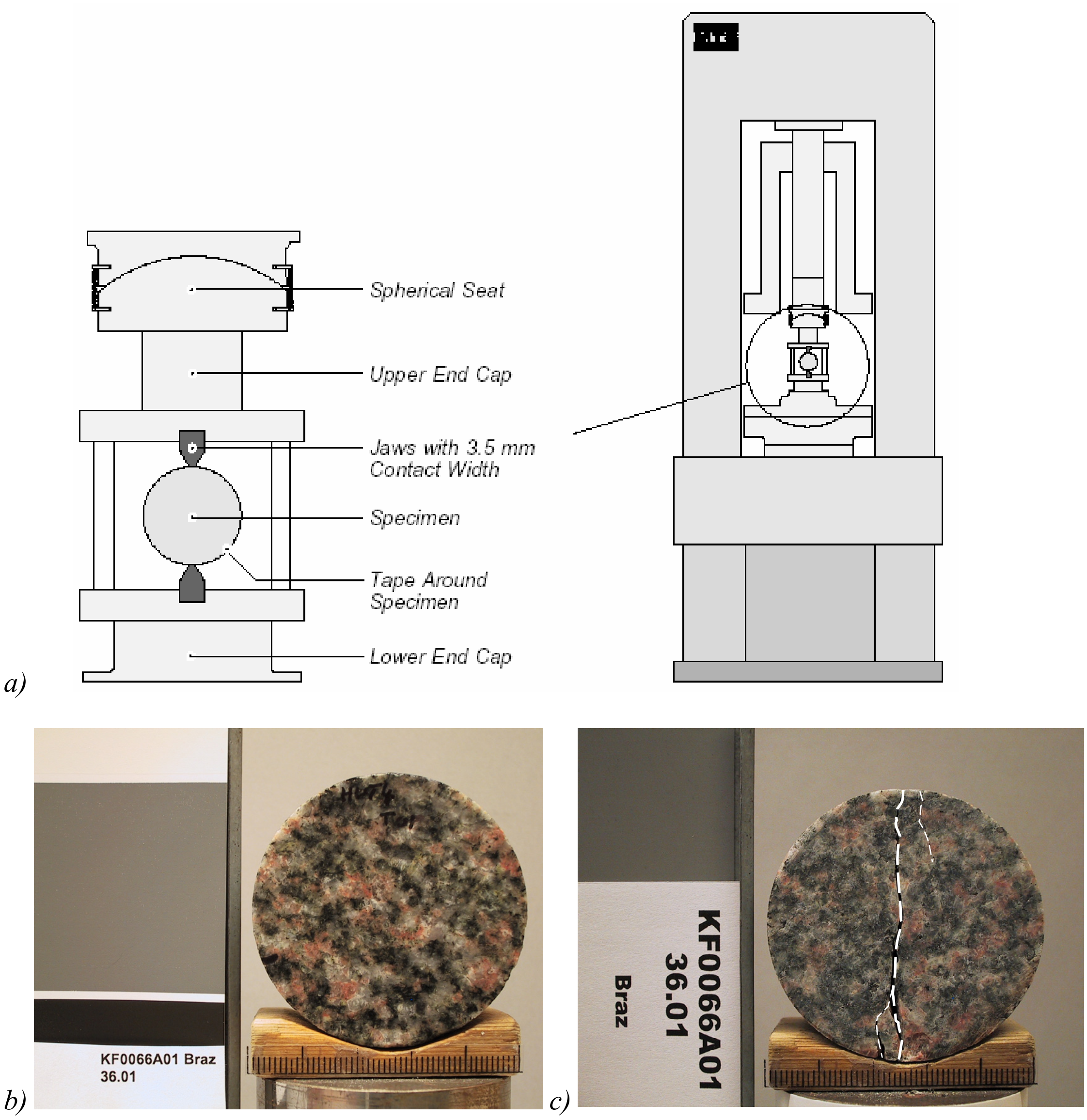

Figure 5-7. *a) Test configuration of the Brazilian test (from Hakala et al. 2005). b) Wet specimen of the Äspö diorite before and c) after the test. Fractures are highlighted by broken lines.*

5.2.2 Uniaxial Compressive Strength tests

For the SRS tests, a good estimate of the short-term-strength is needed to plan the loading sequences close to the expected failure. If the slow loading is started at too low a stress level, the duration of a single test may take several days. On the other hand, if the starting stress level is too high, specimen failure will occur too early and the time-dependent behaviour cannot be recorded. Figure 5-8 presents a typical stress-strain curve from a UCS test on the Äspö diorite.

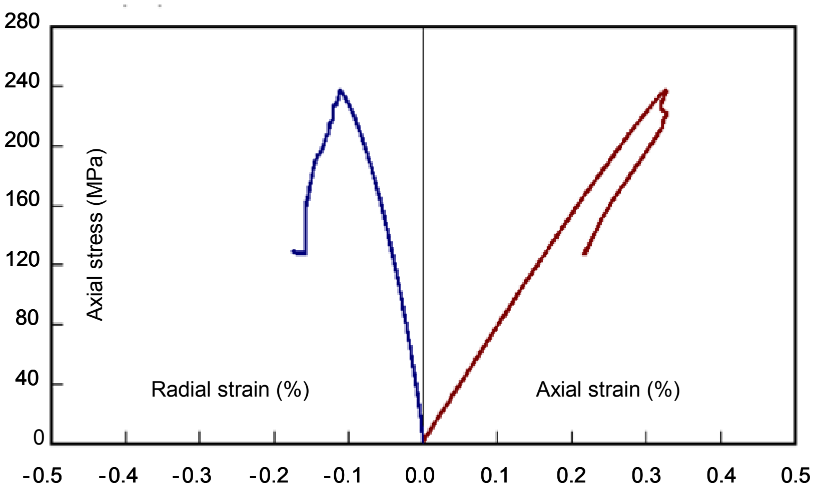

Figure 5-8. *Typical stress-strain curve from a radial strain controlled UCS test on the Äspö diorite (Kuula and Eloranta 2003).*

To plan the SRS tests for the CREEP-project, six UCS tests were conducted to estimate the peak strength of the Äspö diorite. The results are presented in Table 5-1. All specimens have been photographed and tested fully saturated. UCS tests were started with a loading rate of 0.5-1.0 MPa/s with axial load control. The axial load control was changed to radial strain rate control after -0.01% radial strain but before crack initiation stress σ_{ci}. The σ_{ci} values were determined as the stress value where the volume of a specimen starts to increase after the initial compaction phase (Martin and Chandler 1994).

The AE was recorded during the UCS tests (Hakala et al. 2005). The acoustic events are sorted into intervals according to their energy. The crack initiation stress σ_{ci}(AE) was interpreted from the two lowest energy bands (Antikainen 2007). The specimen instrumentation is presented in Fig. 5-9 and the loading equipment in Fig. 5-10. The σ_{ci}(AE) values were compared with the σ_{ci} values (Table 5-1). The interpreted σ_{ci}(AE) values are systematically lower than the σ_{ci} values determined with the volumetric strain method.

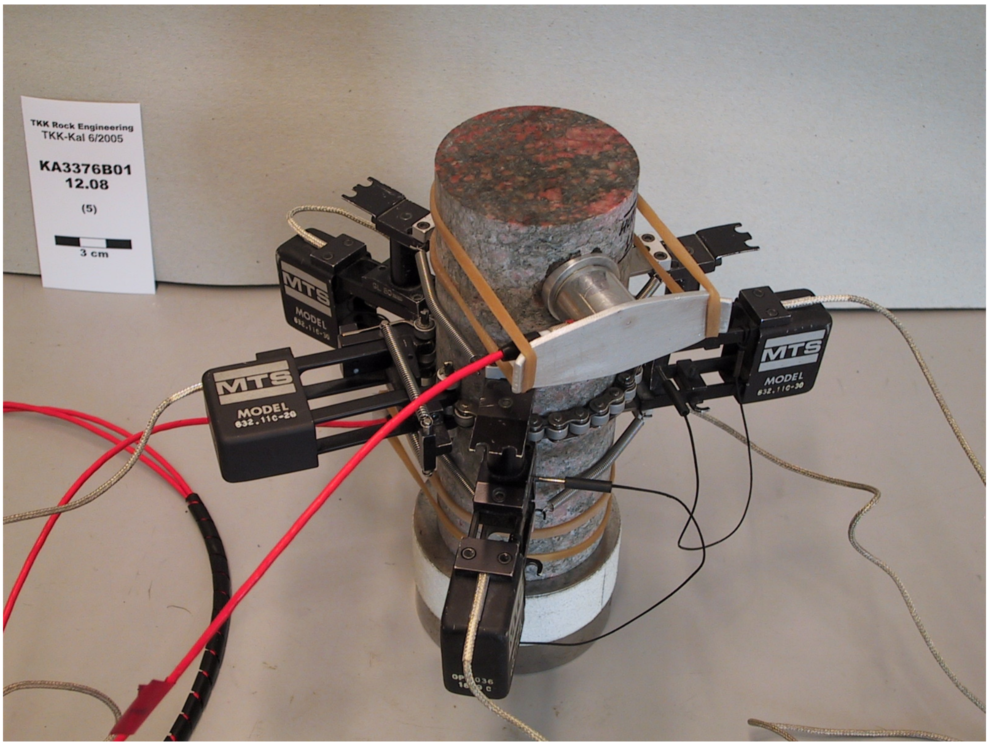

Figure 5-9. *Specimen instrumentation for the UCS test at HUT: three axial extensometers, a chain extensometer for radial displacement and two sensors recording acoustic emission.*

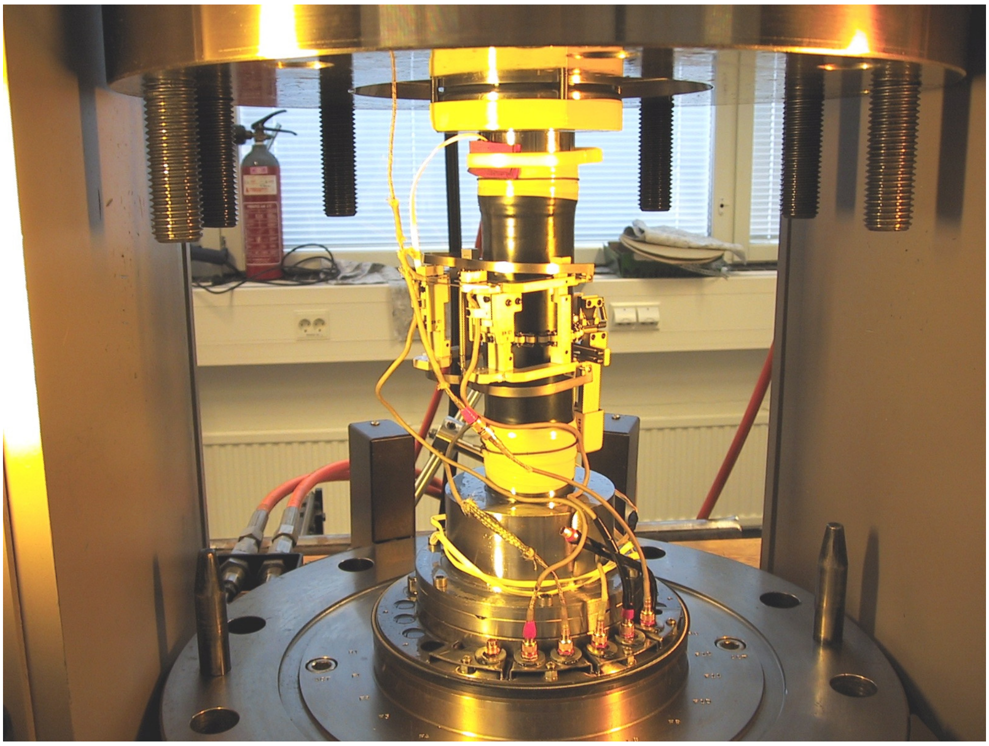

Figure 5-10. *A MTS 815 rock mechanics test system at HUT.*

5.2.3 Triaxial tests

The triaxial experiments were performed at loading rates of 0.5–1.0 MPa/s (average 0.8 MPa/s). Instead of radial strain controlled loading, as was used for the UCS tests, these tests were performed using axial strain rate control corresponding to the above loading rates. The instrumentation of the specimens consists of one strain gage glued onto the specimen surface and two axial and one chain extensometer attached to the thin protective neoprene jacket.

Because the time-dependent behaviour might be a function of the confining pressure, tests with two confining pressures (2 MPa and 7 MPa) were conducted. A typical standard triaxial test is presented in Fig. 5-11 and the test results are summarised in Table 5-1. The critical inelastic strain is calculated by subtracting the elastic axial strain from the total axial strain. The critical inelastic strain is defined as the inelastic strain at the fault nucleation, i.e. when sudden failure occurs. The term 'inelastic strain' as used by Lockner (1998) should be read here as the 'non-linear component of the total strain'.

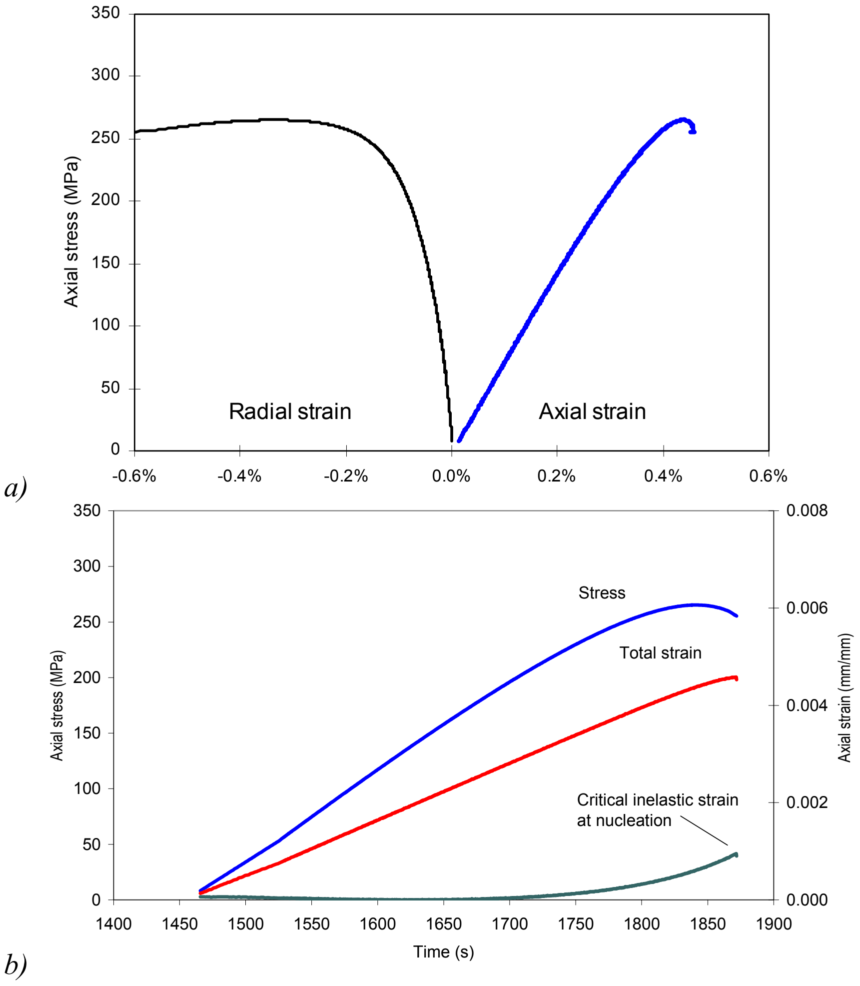

Figure 5-11. *Triaxial test T2201. a) A typical stress versus strain curve. b) Stress, strain and inelastic strain envelope as a function of time (data from Antikainen 2006).*

5.2.4 Strain Rate Stepping tests

The ultimate goal of long-term testing of rock is usually to construct a time-dependent model of rock strength or deformability, or both. Typical compressive tests are: (a) the Constant Stress Test, where the TTF is recorded at different constant stress values; (b) the Fixed Strain or Stress Relaxation Test, where the axial strain is kept constant and the changes in load and radial strain are recorded; (c) the Stress Stepping Test, where the axial stress is increased and possibly decreased stepwise while the strains are recorded; and (d) the SRS test, where the axial strain rate is varied while the strains and axial stress are recorded. The methods have specific advantages and disadvantages (Lockner 1993, 1998). It was evaluated that the problems encountered in hard-rock creep testing due to the heterogeneous rock material, such as the Äspö diorite, can be overcome by SRS tests (Antikainen 2006).

A specimen for the SRS procedure was taken along the core next to each triaxial test specimen. In the SRS test, the stress in the specimen is increased by a similar loading rate as that applied in the triaxial test up to 60% of the peak strength evaluated from the respective triaxial test. After the initial loading the SRS is started. The strain rates are varied stepwise from about 10% to 0.1% of the strain rates applied in the standard tests, resulting in stepwise increasing stresses. The measured stress and strain values are plotted as a function of time. The testing time for SRS tests varied between 17 and 33 h. A typical SRS test is presented in Fig. 5-12 and the results are summarised in Table 5-1.

a)

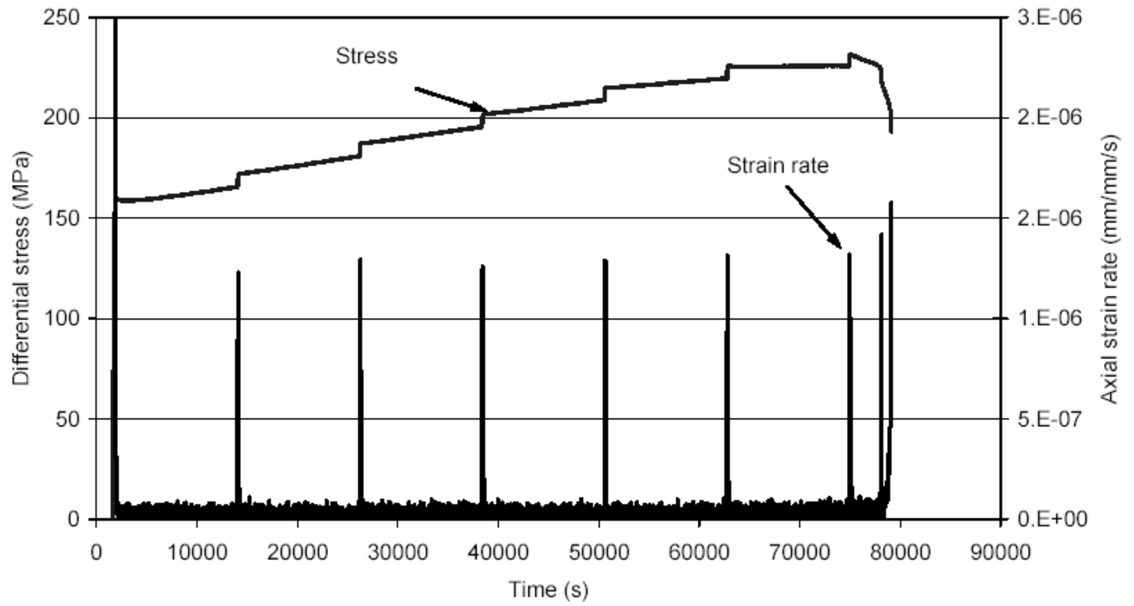

b)

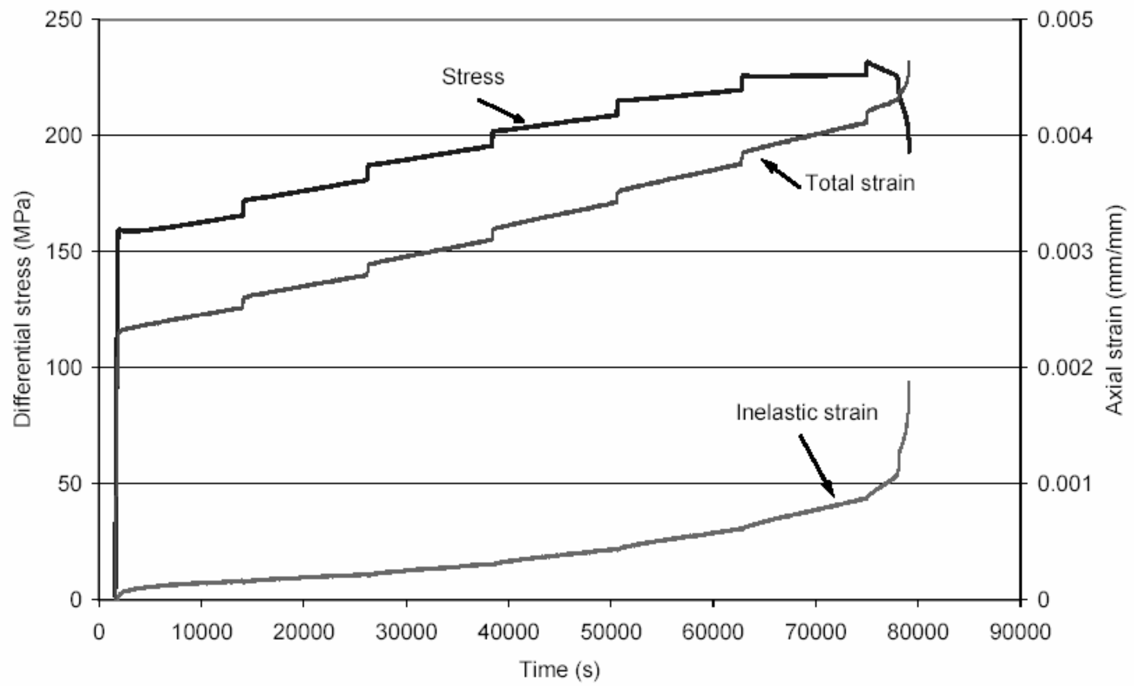

Figure 5-12. *a) Axial strain rate and differential stress (σ_1-σ_3) as a function of time; b) axial strain and calculated inelastic axial strain versus differential stress in the SRS test, S2214 (Antikainen 2007).*

It was shown that the problem of unpredictable and/or excessive test duration in hard-rock creeping tests caused by heterogeneity can be resolved with the SRS test. Confinement stress of 2 MPa provided a reasonably stable process to run through the time-dependent behaviour test using a slow constant axial strain rate. The SRS test results are evaluated and two representative experiments are modelled in Chapter 7.

5.3 Test on fractures

Because the fracture mechanics principles and the SCG theory have been used as a platform for the time-dependent rock behaviour modelling, appropriate fracture tests have to be performed to determine the essential input parameters. Here a short overview of the methods for fracture toughness and fracture stiffness determination is given. Determination of SCG parameters is briefly presented to clarify the physical test of the parameters used in a time-dependent calculation. The laboratory procedures and results are reported in more detail in Backers (2005, 2006), Backers et al. (2006a) and Backers and Stephansson (2007). All fracture test results discussed in this section refer to Äspö diorite at the APSE experiment site.

5.3.1 Fracture toughness

The determination of fracture toughness, K_{IC}, for Mode I loading conditions was carried out according to the ISRM Suggested Method using the Chevron-Bend (CB) method (Ouchterlony 1988). At present, there is no ISRM recommended method to determine Mode II rock fracture toughness. To determine the K_{IIC} of the Äspö diorite, a technique named the Punch-Through-Shear (PTS) test described by Backers (2005) was applied. In the PTS, test a confining pressure can be applied, i.e. a normal stress to the shear-loaded zone. A confining pressure is most desirable for Mode II fracture growth as large compressive pressures suppress the tensile Mode I and therefore Mode II failure is most likely to occur in such environments (Backers 2005). The PTS test is currently in preparation to become an ISRM Suggested Method.

Methods for the determination of fracture toughness, both in Mode I and Mode II, can be found in the literature (Whittaker et al. 1992; Rao 1998, 1999; Backers 2005) and the experimental set-ups are presented in Fig. 5-13. Fracture testing to obtain toughness parameters was carried out by using a stiff, servo-controlled MTS loading machine. All specimens were saturated with deionised water before testing.

The Mode I fracture toughness was determined by carrying out two tests under controlled laboratory conditions. K_{IC} for saturated Äspö diorite yields 2.74 MPa m$^{1/2}$. Mode II fracture toughness was determined by carrying out 11 experiments with a constant displacement rate. The determined K_{IIC} for saturated Äspö diorite yields K_{IIC} = 4.46 MPa m$^{1/2}$.

Backers (2005) reports K_{IC} = 3.83 MPam$^{1/2}$ and K_{IIC} = 5.09 MPam$^{1/2}$ for dry samples of the Äspö diorite. The test series for saturated specimens shows about 30% lower K_{IC} and 12% lower K_{IIC} fracture toughness in saturated test conditions. Although the dry specimens are not manufactured from the same samples as the saturated specimens, it seems that fracture toughness is reduced by the presence of water for both K_{IC} and for K_{IIC}. (Backers et al. 2006a). Fracture toughness determined from the Äspö diorite by Nordlund et al. (1999) and Backers (2003, 2005, 2006) is summarized in Table 5-2.

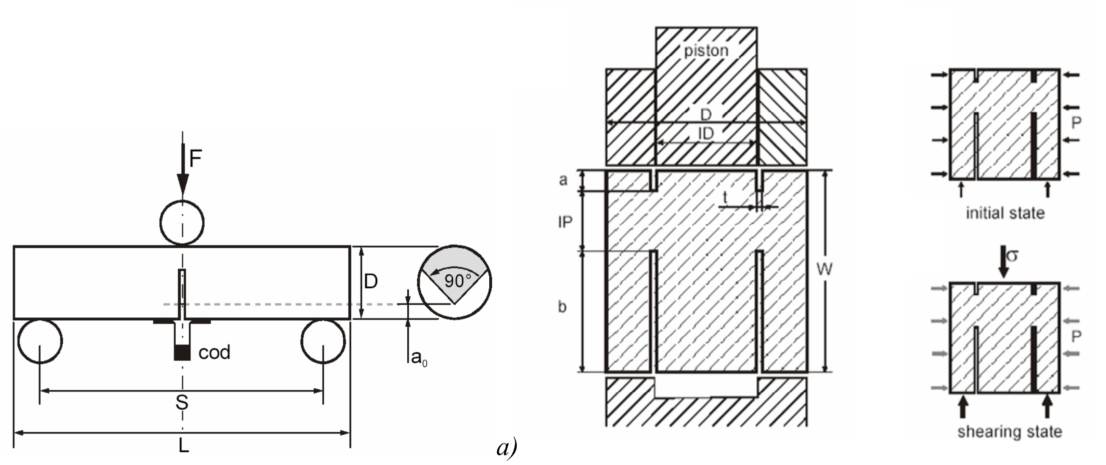

a)

b)

Figure 5-13. *Testing methods for determination of fracture toughness. a) Chevron-Bend configuration (Ouchterlony 1988). b) Testing configuration and loading in the PTS test (Backers 2005).*

5.3.2 Subcritical crack growth parameters

One goal of the CREEP-project was to develop experimental testing methods to describe time-dependent rock fracturing (Rinne 2003). After a study on different approaches to model time-dependent failure of brittle rock (Rinne 2005), the SCG theory, as described in Chapter 3, was chosen as the platform for further studies. To be able to utilise this approach it is crucial to determine the SCG parameters *n* and *A* under Mode I and II conditions. Different methods for experimental determination of these parameters were evaluated by Ojala et al. (2004). It was concluded that to determine these parameters, very few methods exist, and these are for Mode I (tensile) loading only. A method, originally suggested by Wilkins (1980) for Mode I loading conditions, was recommended to be used for further development for Mode II. Modification of Wilkins' method for Mode II parameter determination and a description of related laboratory processes are reported methodically in Backers (2006). Here only an overview is given to clarify the physical test of those fundamental parameters used to model time-dependent failure in this thesis (Chapter 7).

Wilkins carried out tensile tests in order to obtain data in the form of ln(σ_H) versus ln(TTF), where σ_H is the homologous stress ratio that expresses the ratio of the applied stress σ_A to instant breaking stress σ_i of the material. Time to failure and instant breaking stress (σ_i) cannot be measured on the same sample. In practice, the method consists of two sets of tests. Firstly, a series of rapid loading tests at a constant displacement rate is carried out until failure in order to determine the Weibull distribution parameters. This set of samples is also referred to as 'Population 1'. Secondly, a series of constant load tests is performed on a second set of specimens of identical volume ('Population 2'). These tests determine the TTF at a specific stress, (σ_A), which corresponds to a certain failure probability. Sets of tests representing Populations 1 and 2 are assumed to represent material with a similar distribution of strength.

The data from the constant displacement rate experiments can be described using Weibull statistics:

$$P_i = 1 - exp\left[-\sigma_i / \sigma_w \right]^f \qquad (5\text{-}1)$$

where P_i is the cumulative probability of a given instantaneous fracture stress while σ_w and f are the distribution constants. Rapid loading test data are ranked and the cumulative probability is plotted against the failure stress σ_{Ti}. From this plot the Weibull exponent, f, and the scaling factor, σ_w, are determined and the probability function is defined.

The constant displacement data are ranked and paired with the corresponding homologous ratio, $\sigma_H = \sigma_A/\sigma_i$, where σ_A is the constant load and σ_i is derived from Eq. (5-1). The paired data are then plotted into the ln – space (Fig. 5-14). In other words, the probability from the Weibull function for Population 1 is used to determine the respective σ_i for Population 2. The negative inverse of the linear regression to the $\ln(\sigma_H)$ versus ln(TTF) data is the SCG index n.
The TTF versus σ_H diagram and the fracture toughness values K_{IC} and K_{IIC} are used to evaluate the scaling factor A in the Charles power law equation (Eq. 3-2), following the procedure described by Wilkins (1980).

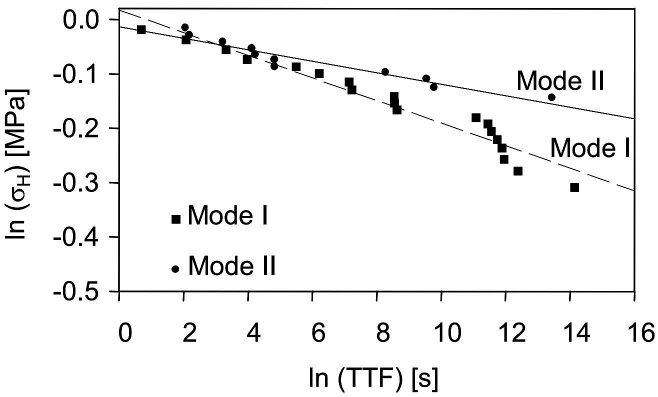

Figure 5-14. Homologous ratio as a function of the ranked TTF data of the Äspö diorite (after Backers et al. 2006a).

The 3PB test was used to determine Mode I SCG parameters. This method uses cylindrical samples with a straight notch and the procedure is quite comparable to the test with CB specimens for fracture toughness testing (as presented in Fig. 5-13a). The set-up of the 3PB test provides rapid fracture propagation and a reliable repeatability of results (Backers 2006). To determine subcritical crack growth parameters in Mode I, 19 constant displacement rate experiments and 26 TTF tests were performed. The PTS configuration was used to determine Mode II SCG parameters (Fig. 5-13b). For Mode II, the number of tests was 11 displacement rate experiments and 16 constant displacement (TTF) tests.

The constant load PTS tests have shown that time-dependent fracturing exists under Mode II loading under laboratory conditions (Backers et al. 2006a). The laboratory campaign gave n = 48 and $-\log A$ = 24 for Mode I conditions, and n = 94 and $-\log A$ = 65 for Mode II conditions. Figure 5-15 presents the crack velocity versus stress intensity factor data for Mode I and Mode II loading conditions.

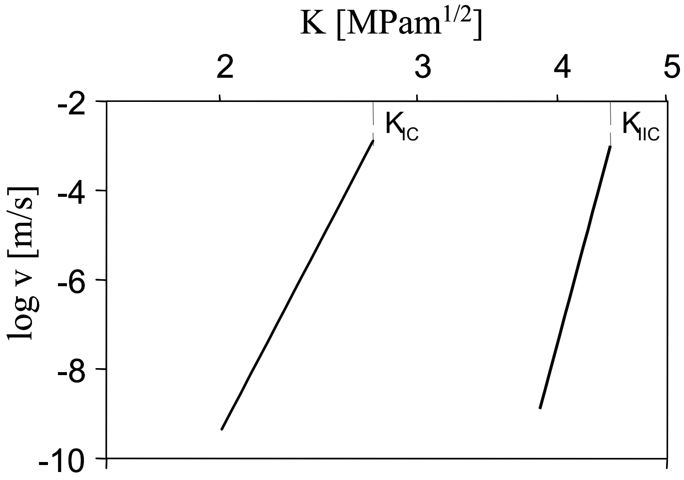

Figure 5-15. *Crack velocity log (v) versus stress intensity factor (K) for Mode I and Mode II subcritical crack growth (Backers et al. 2006a).*

5.3.3 Fracture normal stiffness

Backers (2003) reports normal stiffness test results on the Äspö diorite using the crack produced in the CB tests. Firstly, the stiffness of the intact CB specimen was measured, then the Mode I fracture toughness was determined. The fracture was propagated almost through the sample until a small rock bridge remained to hold the newly formed fracture faces in position. The stiffness of the fractured specimen was then determined. The specimen is loaded perpendicular to the fracture. A cyclic load is applied in axial displacement control and the fracture closure is measured using a clip gage (clip-gage opening displacement, COD) (Fig. 5-16). Four loading cycles are carried out with increasing maximum force. The displacement is measured to an accuracy of 0.5 μm. The maximum force that can be applied with a sufficient accuracy is 25 kN. The normal stiffness, K_N, is determined on the last loading cycle. The displacements of the intact and fractured specimens were subtracted from each other for the same load, yielding the fracture stiffness plot (Backers in Staub et al. 2004).

The average initial fracture normal stiffness (K_{ni}) for new cracks in the Äspö diorite determined from test specimens is 175 ± 68 GPa/m. It varies between 105 GPa/m and 311GPa/m at a normal stress between 0 and 1.5 MPa. At a normal stress between 12 and 25 MPa, the average fracture normal stiffness (K_{nh}) is about 27000 ± 23000 GPa/m and the values vary between 3000 GPa/m and 54000 GPa/m.

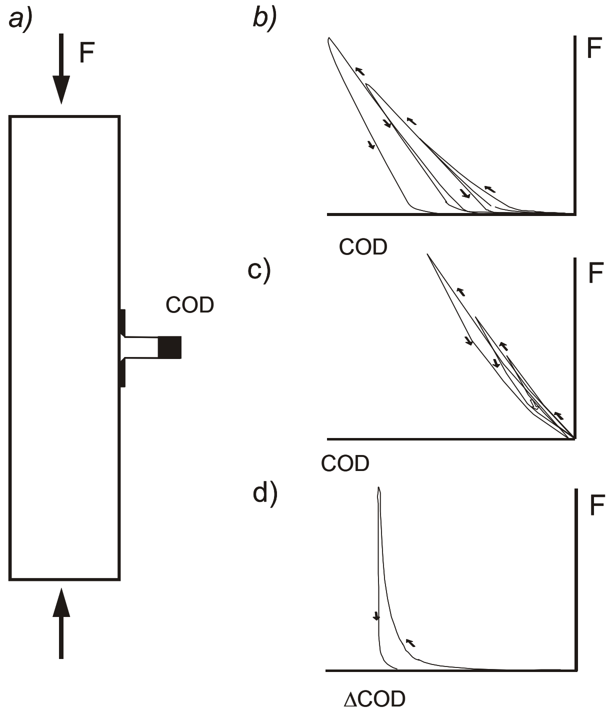

Figure 5-16. *(a) Loading set-up for fracture normal stiffness testing. (b)-(d) force versus cod plots of (b) fractured rock, (c) unfractured rock and (d) displacements of unfractured rock are subtracted from displacements of fractured rock (Backers in Staub et al. 2004).*

Fracture stiffness is further discussed in Section 8.3.8.

5.4 Input parameters suggested for modelling

A summary of material parameters used in the following FRACOD models is listed in Table 5-2. Models assume all material parameters to be constant, i.e. stress, size, temperature or time dependency is not considered.

Uncertainties exist concerning the fracture properties of the newly formed cracks because there are no appropriate techniques available to directly define these parameters. Numerical sensitivity analyses have been performed with varying crack lengths and crack densities to obtain these values (Section 6.3). Uncertainties related to the input parameters are discussed in Section 8.3.

Table 5-2. Input parameters for FRACOD simulations.

Parameter	Value and unit	References and notes
Intact rock		
Young's modulus (E)	68 GPa	Rinne et al. 2003a (APSE)
Poisson's ratio (υ)	0.24	Rinne et al. 2003a (APSE)
Cohesion (c_i)	31 MPa	Rinne et al. 2003a (APSE)
Friction angle (ϕ_i)	49°	Rinne et al. 2003a (APSE)
Tensile strength (σ_t)	14.8 MPa	Rinne et al. 2003a (APSE)
Fractures		
Fracture toughness, (K_{IC})	3.21 MPam$^{1/2}$	Nordlund et al. 1999 (assumed to be dry)
Fracture toughness, (K_{IC})	3.83 MPam$^{1/2}$	Backers 2005. Dry Äspö diorite (APSE)
Fracture toughness, (K_{IC})	2.74 MPam$^{1/2}$	Backers 2006. Saturated Äspö diorite (DECOVALEX)
Fracture toughness, (K_{IIC})	4.60 MPam$^{1/2}$	Backers 2003. Dry Äspö diorite (APSE)
Fracture toughness, (K_{IIC})	5.09 MPam$^{1/2}$	Backers 2005. Dry Äspö diorite
Fracture toughness, (K_{IIC})	4.46 MPam$^{1/2}$	Backers 2006. Saturated Åspö diorite (DECOVALEX)
Fracture cohesion (c_f)	31 MPa / 0MPa	Rinne et al. 2004. Newly formed crack (APSE)
Friction angle (ϕ_f)	49°	Rinne et al. 2004. Newly formed crack (APSE)
Fracture normal stiffness, (K_N)	30x10^{12} Pa/m	Rinne et al. 2004. Newly formed crack (APSE)
Fracture shear stiffness, (K_S)	30x10^{12} Pa/m	Rinne et al. 2004. Newly formed crack (APSE)
Fracture normal stiffness, (K_N)	2x10^{12} Pa/m	Rutqvist et al. 2007 (DECOVALEX)
Fracture shear stiffness, (K_S)	0.2x10^{12} Pa/m	Rutqvist et al. 2007 (DECOVALEX)
Dilation angle (ϕ_d)	2.3° /12.1°	Rinne et al. 2003a. Shear / tensile cracks (APSE)
Initial fracture aperture (a_i)	≤10x10^{-6}m	Rutqvist et al. 2007 (DECOVALEX)
Residual fracture aperture (a_r)	≤3x10^{-6}m	Rutqvist et al. 2007 (DECOVALEX)
Initial crack half length (a_0)	0.5 mm-3 mm	Estimated, see Section 8.3
Crack distance (density, d)	5-10 mm/mm	Estimated, see Section 8.3
Subcritcal crack growth		
Stress corrosion index (n_1)	48	Backers 2006. Saturated Äspö diorite
Scaling factor (-logA_1)	24	Backers 2006. Saturated Äspö diorite
Stress corrosion index (n_2)	94	Backers 2006. Saturated Äspö diorite
Scaling factor (-logA_2)	65	Backers 2006. Saturated Äspö diorite

6 NON-TIME-DEPENDENT FRACTURE MODELLING

This chapter aims to introduce the reader to the failure mechanisms as suggested by the FRACOD models. It also aims to simulate the failure of the Äspö diorite as observed in short-term strength tests including the pre- and post-peak failure behaviour. Results from models representing tensile failure, failure under uniaxial compression and confined compressive loading conditions are presented. Factors affecting the failure have been highlighted by examples.

The material parameters used in calculations refer to the 'Äspö diorite' at the APSE experiment site, as listed in Table 5-2. Fracture toughness representing the Äspö diorite in saturated conditions is used, if not otherwise stated.

The intact rock material between cracks is assumed to be homogeneous, isotropic and linearly elastic. All models assume 2D-plane-strain conditions. The model accuracy, parameter sensitivity to results and uncertainties related to material parameters are discussed in Chapter 8. The FRACOD code has been improved continuously during the studies reported in this thesis and the code improvements are mainly related to the SCG function. The most part of models presented here are calculated using FRACOD version 2.0.0 (released June 2005) through version 2.2.1 (released October 2006). Slight differences may appear in results from different code versions but generally the results are consistent.

6.1 The stability of a single inclined crack

The stability analysis for a single inclined crack under uniaxial and biaxial compressive loading conditions using FRACOD has been reported in Rinne (2000). To demonstrate the fracture behaviour as suggested by the code the crack model is subjected to six different loading conditions, as presented in Fig. 6-1. The crack is inclined 30° with respect to the major principal stress (σ_1). The state of the crack according to modelling is as follows:
Uniaxial loading:
a) Low uniaxial compressive load. Fracture cohesion resists sliding of the fracture and only elastic deformations controlled by the fracture stiffness occur.
b) The load is increased above fracture cohesion and slip occurs.
c) The load is increased above the threshold load for fracture propagation. The fracture grows only by one fracture tip element. This is referred to here as stable fracture propagation.
d) The uniaxial load is increased successively and open wing cracks develop.
Biaxial loading:
e) Biaxial loading with low confinement (σ_2). Fracture propagation alternates between tensile and shear failure, leading to slip and opening displacement on the new fracture surface. The sections of tensile failure are stable, but the shear failure propagation occurs in an unstable manner. The shear failure will, however, cease after a few elements of fracture propagation and the 'wing-crack' propagation takes over in a stable manner.
f) Biaxial loading with high confinement. The crack propagates in shear mode and extends in an unstable manner after the load is increased above the critical magnitude.

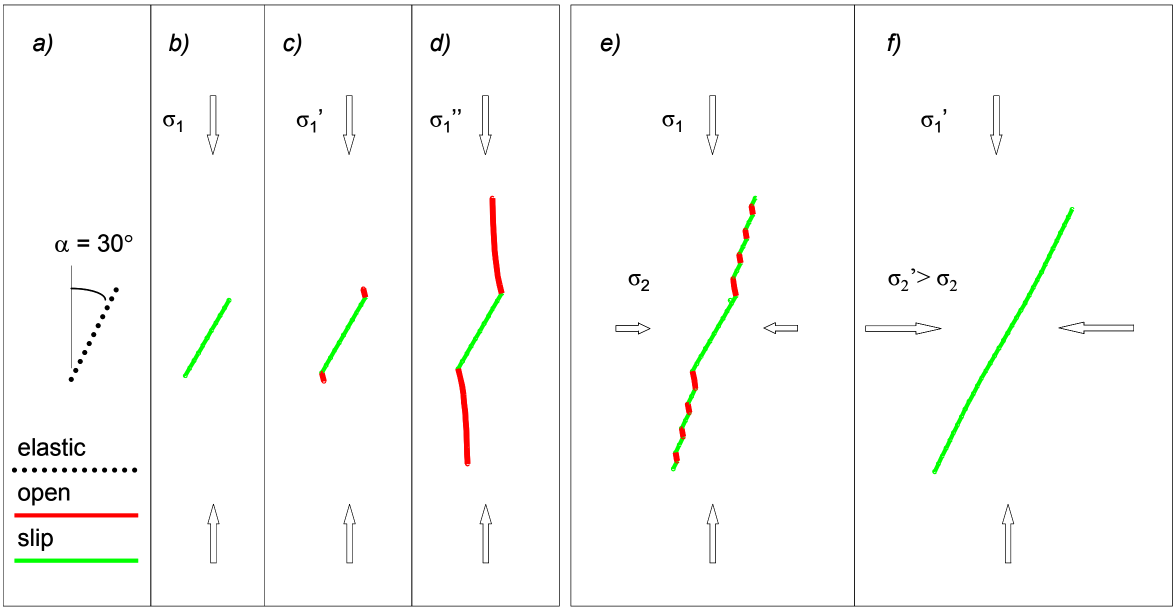

Figure 6-1. *Propagation of inclined cracks subjected to six far-field loading conditions according to FRACOD. Figures a) to d), uniaxial loading; e) and f), biaxial loading (Rinne 2000).*

In the following example, a single pre-defined model crack extends in a rock specimen subjected to uniaxial compression (Fig. 6-2). The initial angle of the crack is α = 20° with respect to the major principal stress. Loading configuration and parameters are as described for the UCS model in Section 6.5, except here an asymmetrical model is used. The compression is introduced in the model by downward displacement of the top boundary. The shear displacement is restricted in the top and bottom of the model to simulate the effect of friction between the load platens and the specimen in all 'specimen models' presented in this thesis.

Local tensile failure takes place at the fracture tips (Fig. 6-2a) and the fracture extends with wing cracks that tend to align themselves towards the orientation of the major principal stress (see also Fig. 6-1 c and d). Increasing stress is required to maintain wing-crack propagation. After the stresses have reached a certain level and the wing crack is almost parallel with the major principal stress, Mode II failure takes place (Fig. 6-2b). The fracture extends alternating between Mode I and II failure (Figs 6-2b, c and d). The shear component of the failure is increased as the fracture approaches the top and bottom boundaries (Fig. 6-2e). Modelled stress distribution in a loaded uniaxial specimen is discussed in more detail in Section 6.5 (see Fig. 6-25).

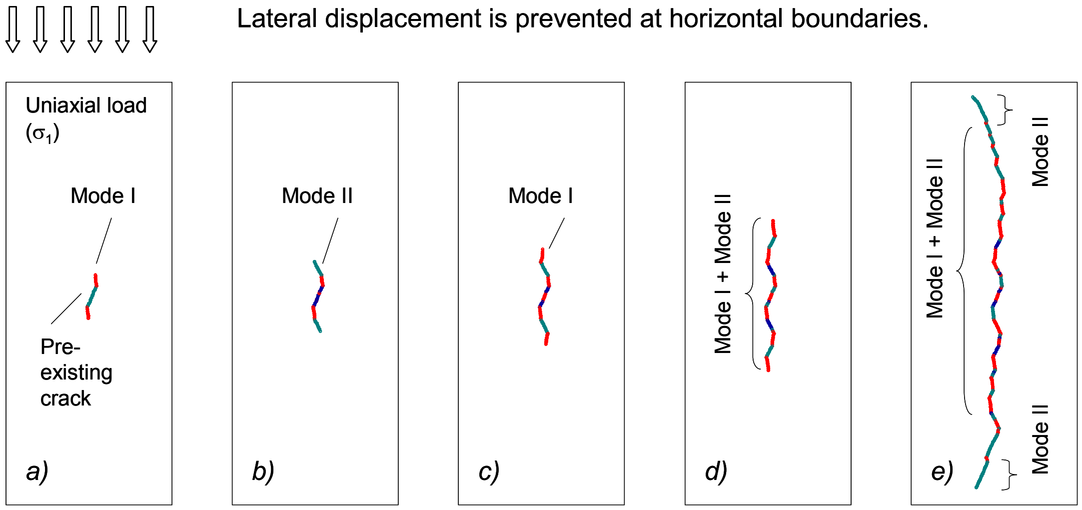

Figure 6-2. *Fracture propagation of a single inclined crack subjected to uniaxial compression.*

6.2 Interaction and coalescence of fractures

Interaction and coalescence of fractures are complex processes and are not studied here in detail. Some examples will, however, be presented. In Fig. 6-3, two inclined cracks propagate under an increasing uniaxial load. Only the inner crack tip extends significantly while the other one is affected by the close crack and extends only by a few elements. Figure 6-4b illustrates the effect of confinement on crack interaction and crack coalescence.

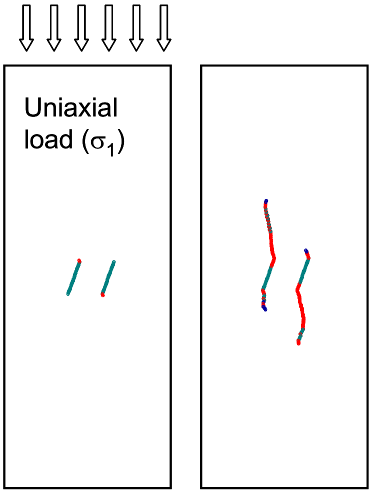

Figure 6-3. *FRACOD simulations of interaction of two inclined ($\alpha = 20°$) fractures subjected to uniaxial compressive loading.*

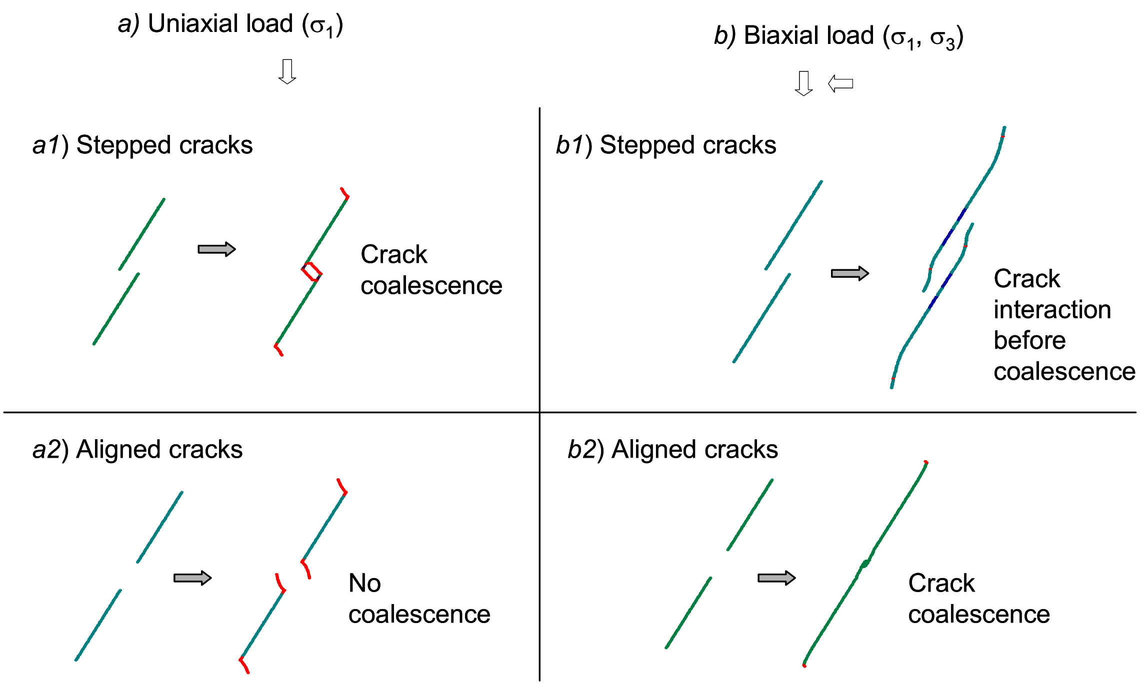

Figure 6-4. *Effect of loading configuration on crack interaction. a) Uniaxial load, b) biaxial load.*

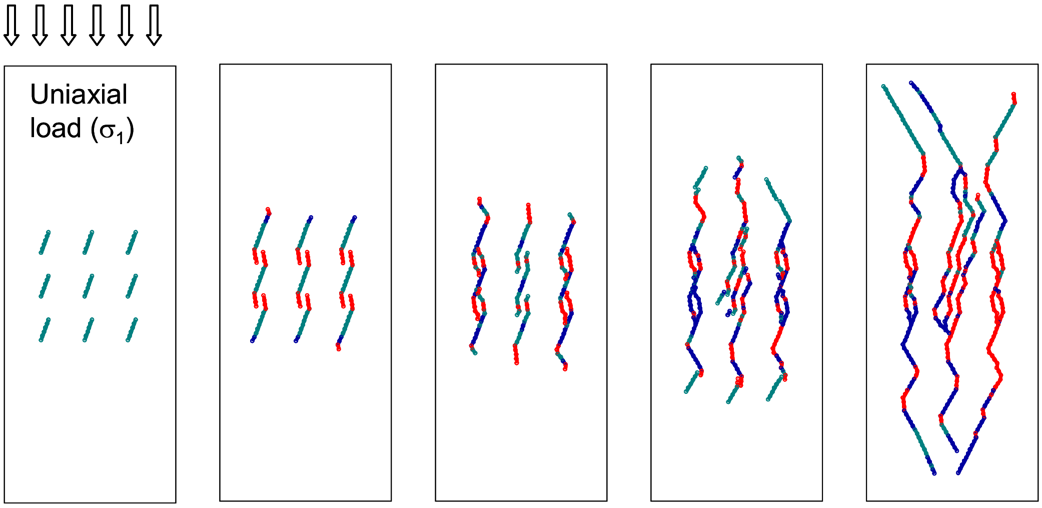

Figure 6-5. *FRACOD simulation of a set of nine parallel and inclined cracks subjected to an increasing uniaxial load.*

In Fig. 6-5, a fracture pattern of a set of nine inclined parallel cracks is subjected to a compressive uniaxial stress.

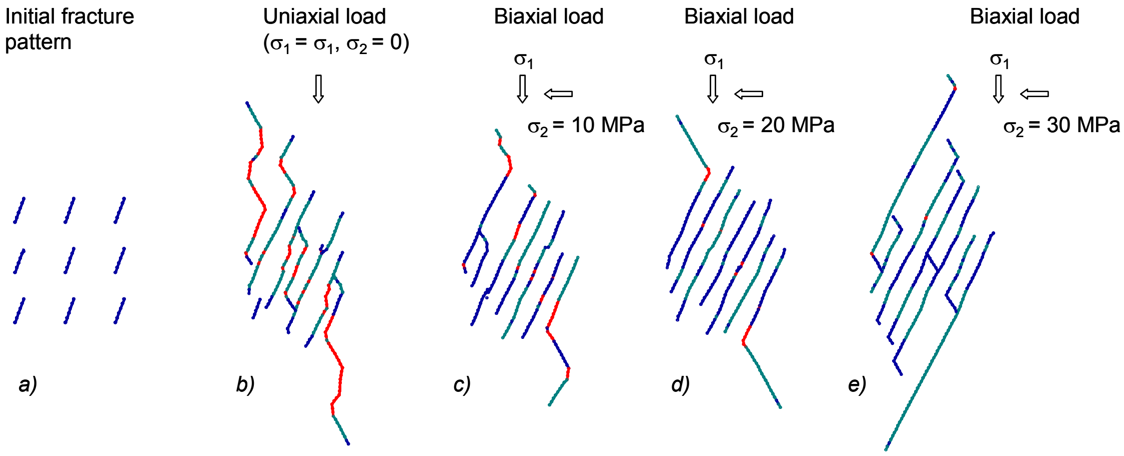

Figure 6-6. *Effect of confining pressure on fracture pattern. a) The initial geometry of a set of nine inclined cracks. Fracture pattern after b) uniaxial loading. Fracture pattern after loading with c) 10 MPa confining pressure, d) 20 MPa and e) 30 MPa confining pressure.*

Figure 6-6 shows the effect of confining pressure on failure of the same fracture pattern as in Fig. 6.5. The effect of finite boundaries is avoided by using a far-field stress model. The formation of distinct shear planes is more obvious if the confinement is applied.

The fracture pattern from numerical models as presented in Figs 6-1 to 6.6 will be discussed more thoroughly and compared with behaviour observed in laboratory experiments in Chapter 8.

6.3 Analyses of newly formed cracks

Size, geometry and spatial distributions of different kinds of micro-defects may vary considerably throughout the rock volume. Minerals with different stiffness properties will also cause stress disturbance at grain boundaries under loading. Experimental indications of these micro-defects are of great interest. In practice, however, it is not possible to model all these micro-defects, including the fracture process zone, in detail.

For FRACOD models, the ‘intact rock’ material between cracks is assumed to be homogeneous, isotropic and linearly elastic. To simulate the failure of ‘intact rock’, defects must be incorporated into the model to induce the inherent stress distribution. This is dealt with by using representative flaws, i.e. newly formed cracks, as described in Section 4.4. Crack size, crack density and the initial fracture angle with respect to loading affect the stress redistribution and thus control the critical applied load required for fracture initiation. In addition, for a closed crack the fracture surface properties also affect the deformations and the redistribution of stresses. The question is how well the modelled newly formed cracks mirror the microstructure of the material in view of stress redistribution. The aim of the following analysis is to shed light on these artificial small-scale discontinuities incorporated in the model to generate the failure process.

6.3.1 Initial crack length

Figure 6-7 illustrates the critical half-crack length versus far-field stress at fracture initiation. Both analytical results and the FRACOD approximation are presented. The level of far-field stress required for fracture initiation (and propagation) is calculated for seven cracks with half-crack lengths varying from 0.5 mm to 15 mm. The crack element length is 0.2 mm for all cases. As can be seen from the diagram, the error from the numerical approximation is small with an initial half-crack length *a* > 2 mm. The maximum error (8.6%) is calculated for the shortest crack (*a* = 0.5 mm) discretised into five elements.

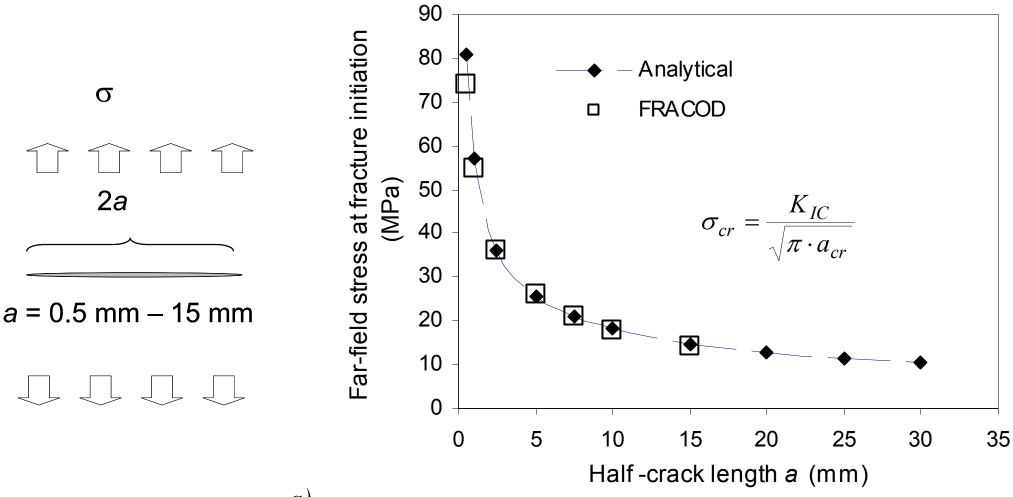

a) *b)*

Figure 6-7. *a) Loading configuration. b) The critical half-crack length versus tensile stress required to initiate fracture propagation.* $K_{IC} = 3.21\ MPam^{1/2}$.

From Fig. 6-7 it can also be seen that the stress required for fracture initiation increases rapidly when the half-crack length is less than about 10 mm. When the half-crack length is more than 20 mm, the far-field stress required to initiate fracture propagation is not so sensitive to the crack length. Figure 6-8 shows the stress distribution around a $2a = 10$ mm long crack subjected to a 26 MPa far-field tensile stress. The fracture toughness is $K_{IC} = 3.21$ MPam$^{1/2}$ as employed in Fig. 6-7. The tensile stresses are considered to be positive in this thesis.

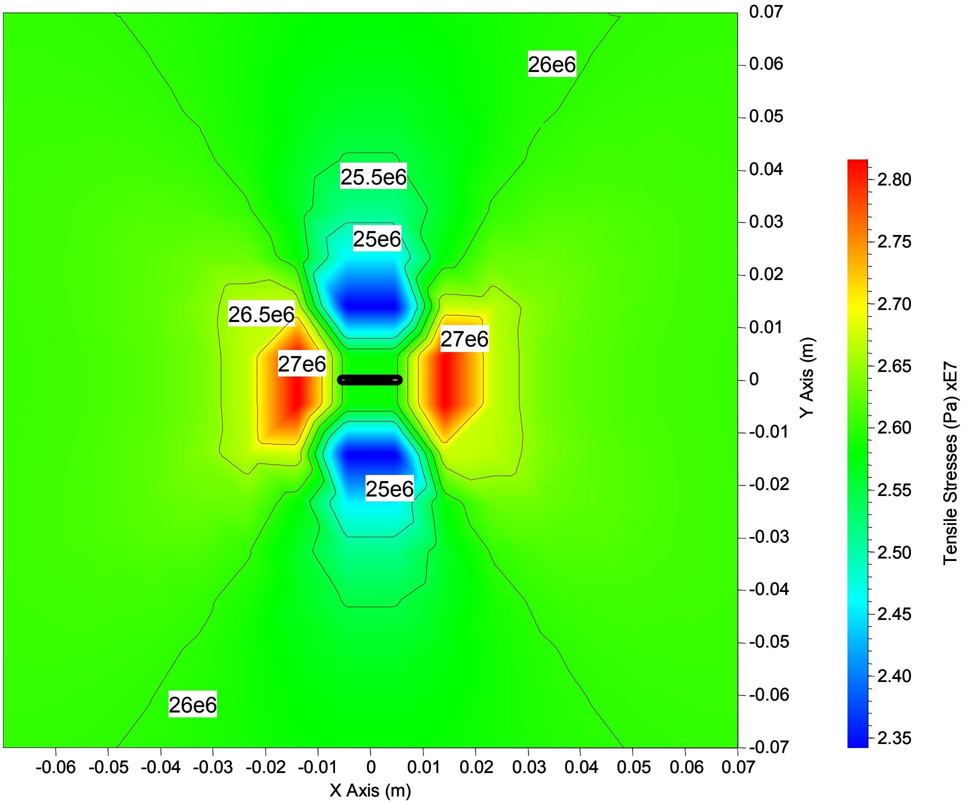

Figure 6-8. *Tensile stress distribution prior to fracture initiation around a horizontal crack (2a = 10 mm) subjected to a 26 MPa tensile far-field stress.*

Similarly to what was shown for a tensile crack, an inclined crack subjected to a compressive stress is presented to demonstrate the effect of crack length on required far-field stress for fracture initiation (Figs 6-9 and 6-10). Also in this example, elements defining a crack have a length of 0.2 mm. An inclination of $\alpha = 20°$ is studied mirroring the angle of the newly formed shear cracks in the Äspö diorite models ($\theta_{is} = \phi_i/2 + 180°/4 \approx 70°$, when $\phi_i = 49°$ and θ_{is} measured from the direction of minor principal stress).

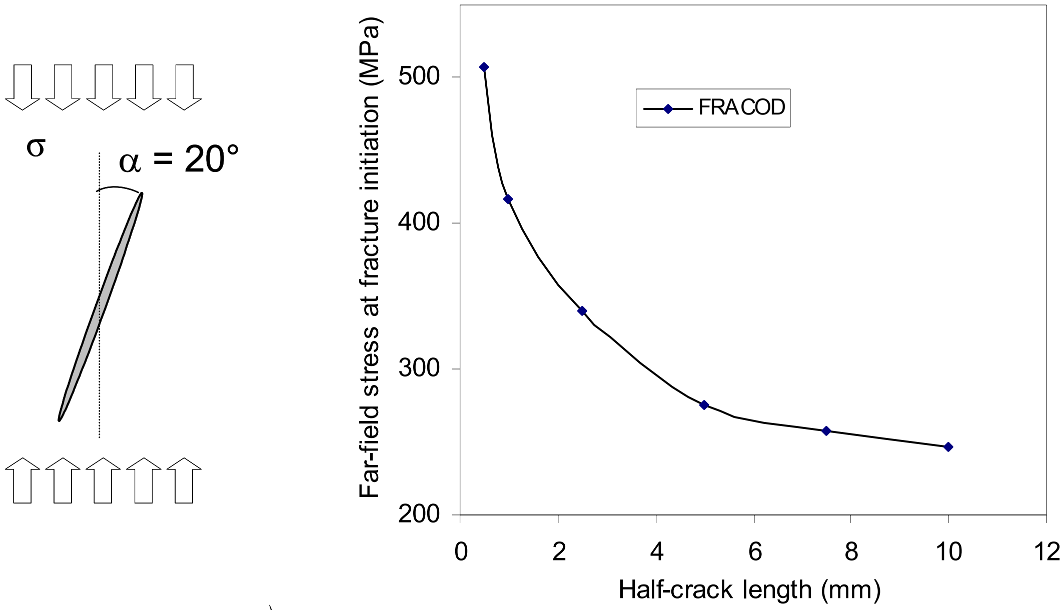

a) *b)*

Figure 6-9. *a) An inclined crack subjected to far-field compression; b) the initial crack length versus critical applied stress for fracture initiation (*$K_{IC} = 3.21\ MPam^{1/2}$*,* $K_{IIC} = 4.60\ MPam^{1/2}$*).*

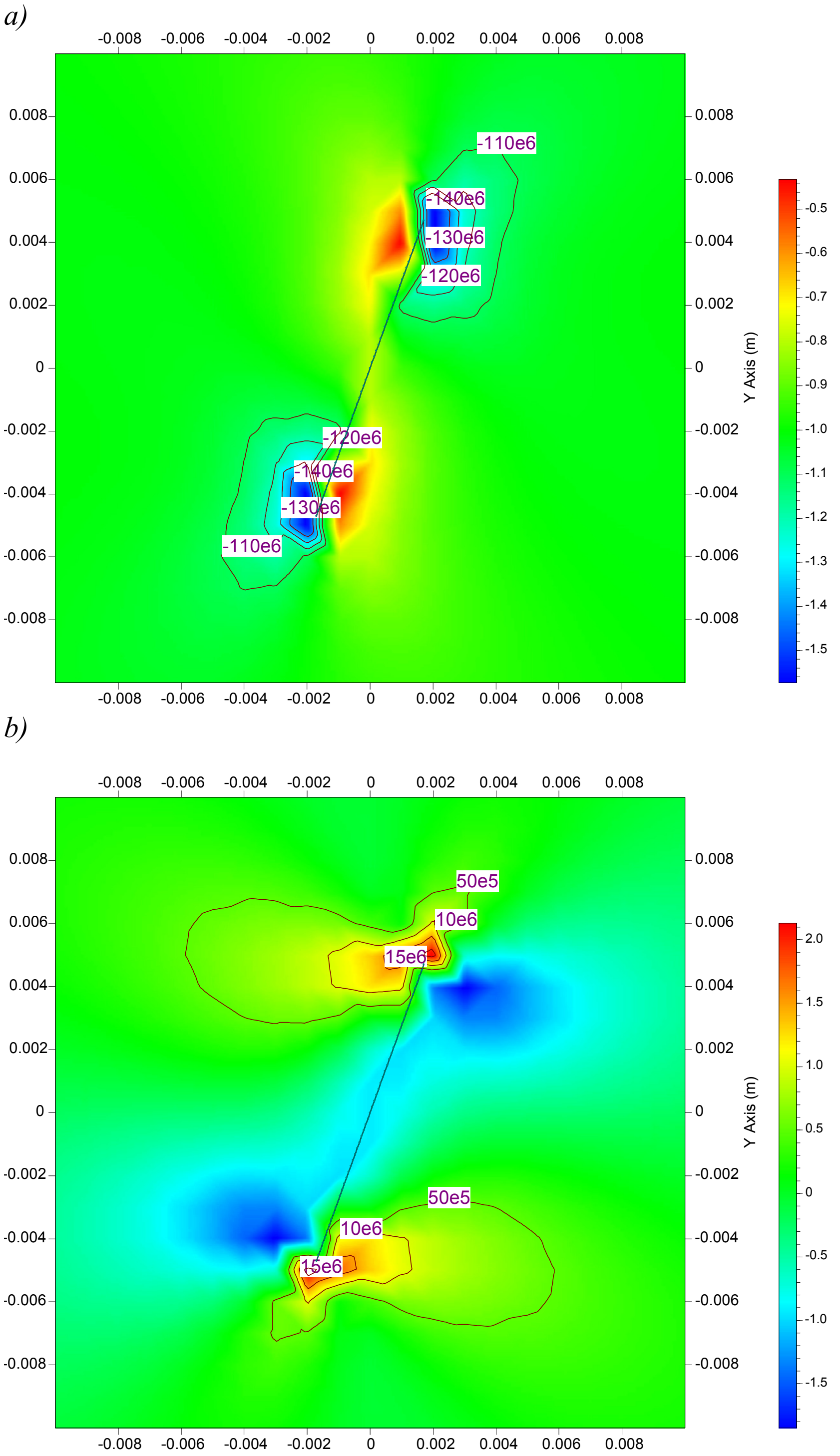

Figure 6-10. *Inclined crack (2a = 10 mm and α = 20°) subjected to a uniaxial compressive far-field stress of 100 MPa. The compression has a negative sign: a) major compressive stresses; b) major tensile stresses.*

6.3.2 Interaction of two closely distanced cracks

In this section, we investigate how the distance between two horizontal cracks affects the far-field tensile stress required to initiate fracture propagation (Fig. 6-11). The distance between these two cracks is varied and the critical applied load for crack propagation is calculated. The crack length is 2*a* = 1 mm and is defined by 25 elements, i.e. fine model discretisation is used and the element length is 40 μm.

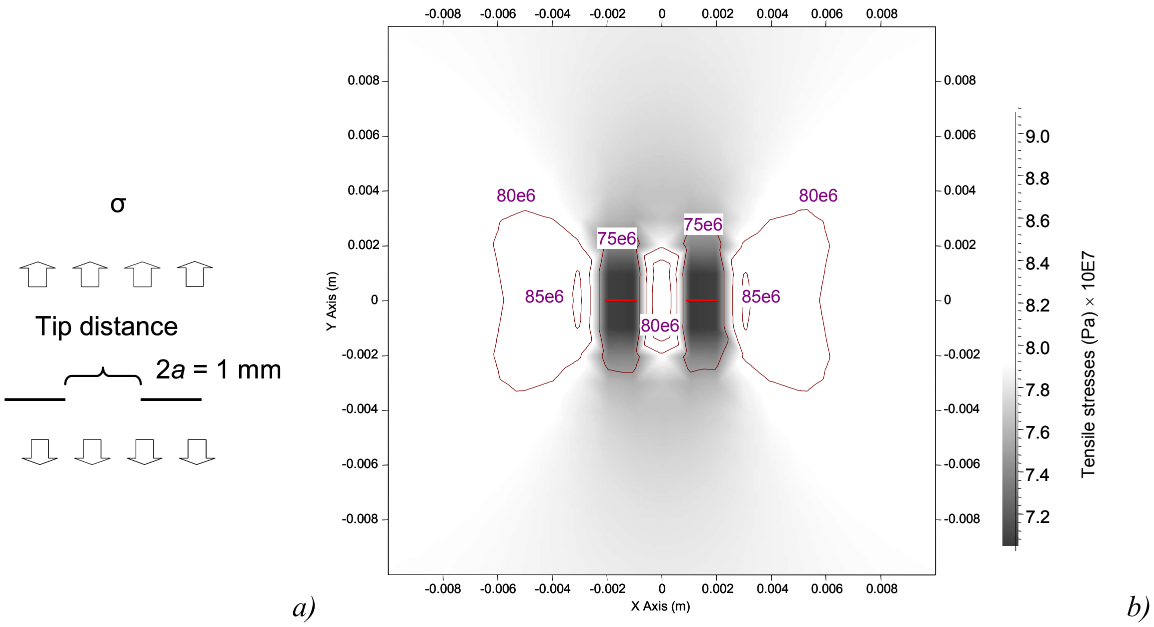

Figure 6-11. *a) Loading configuration for two horizontal cracks subjected to far-field tensile stress. b) Stress distribution around two interacting cracks prior to fracture propagation (tip distance 1 mm; σ = 75MPa).*

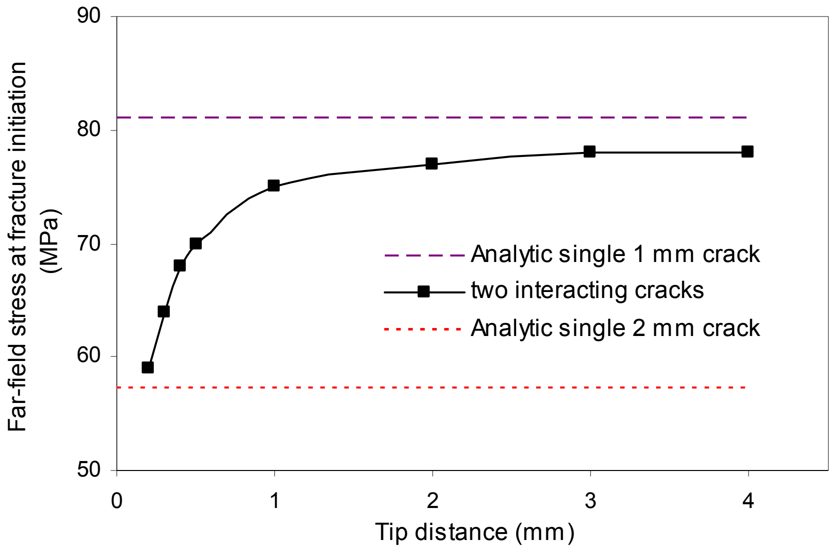

Figure 6-12. *Far-field stress at fracture initiation for two cracks with varying crack distance in tensile conditions.*

From Fig. 6-12 it can be seen that the effect of two closely distanced cracks becomes significant when the tip distance is less than 2 mm for the studied loading configuration. The analytically determined critical stresses for a single isolated crack of length 1 mm and a single 2 mm crack are presented for comparison. Similar analyses were made for two parallel inclined cracks (Figs 6-13 and 6-14) and for two successive aligned cracks (Fig. 6-15) to analyse the interaction and effect of the distance on strength under compression.

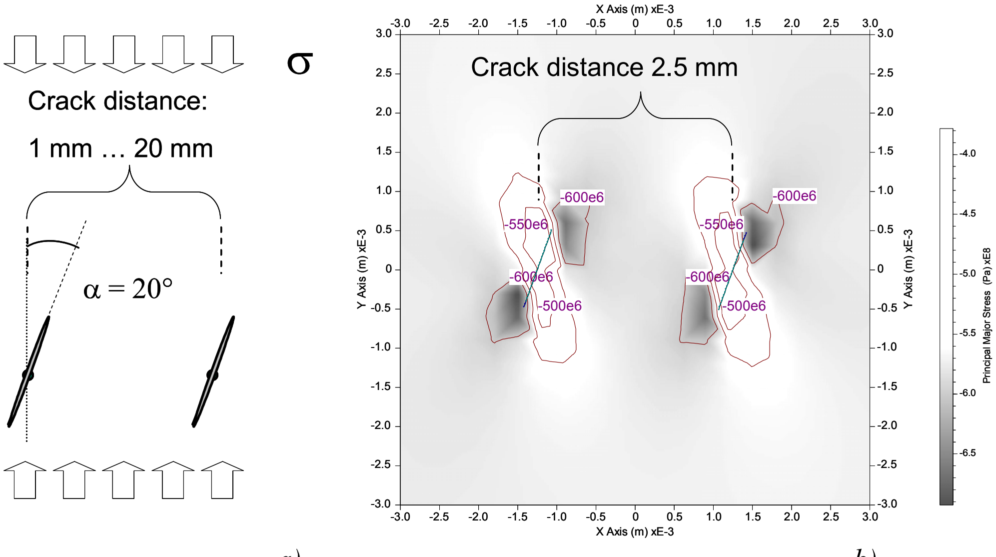

a) *b)*

Figure 6-13. *a) Loading configuration; and b) major stress distribution prior to fracture initiation for two inclined and closely distanced cracks.*

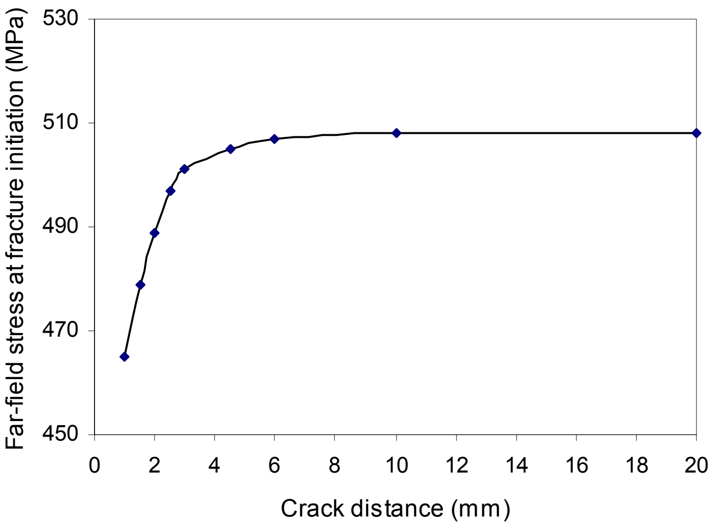

Figure 6-14. *Crack distance versus far-field stress required for fracture initiation.*

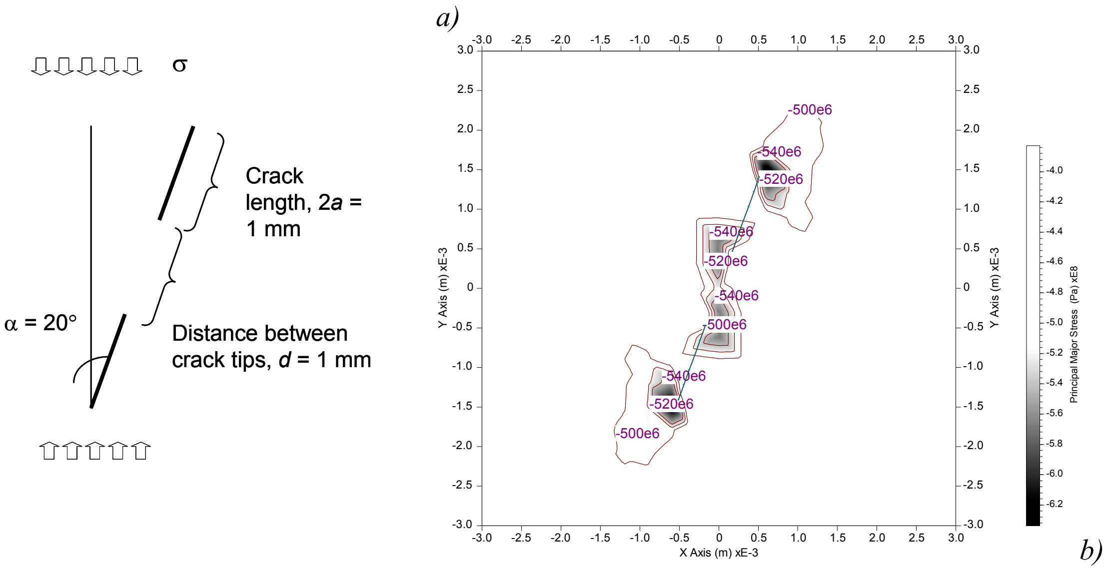

Figure 6-15. *a) Loading configuration for two aligned cracks; b) stress distribution around two cracks.*

For the loading configuration presented in Fig. 6-15, the effect of crack distance on far-field stress to initiate the crack propagation is comparable to the loading configuration presented in Fig. 6-11 and results in that presented in Fig. 6-12. As the distance between cracks increases the far-field stress required to initiate the crack increases and asymptotically approaches the far-field stress required to initiate a single crack. When the distance between two cracks becomes zero they perform as one crack. It must, however, be noted that the accuracy of the presented calculations becomes lower when the crack tips are closer than about twice the element length (2 × 0.2 mm).

The calculations with a compressive load indicate that the influence of two closely distanced cracks on the far-field stress required for fracture initiation is comparable to the tensile stress conditions. The interaction between two cracks with similar geometries becomes significant when the distance is less than about three times the crack length for the studied loading configurations.

6.3.3 Interaction of multiple cracks

The following model aims to study how the number of cracks in a set affects the far-field stress required for fracture initiation. The loading configuration is presented in Fig. 6-16. Cracks, each having a length of 2*a* = 1 mm, are added one after another in the model. The critical far-field stress for fracture initiation is calculated for every set after adding a new crack. The distance between two crack tips is 1 mm for all cases and a crack element length of 0.2 mm is used.

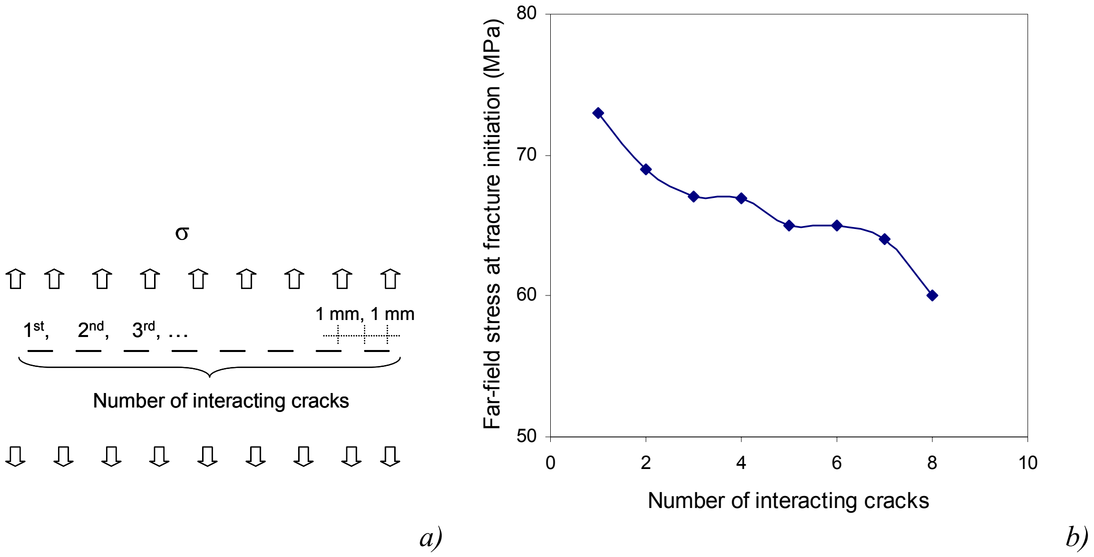

Figure 6-16. *a) Loading configuration. Each crack has a length of 2a = 1 mm. b) Far-field stress required to initiate fracture propagation for sets of interacting horizontal cracks.*

As expected, increasing the number of closely distanced cracks in a set reduces the threshold magnitude of the far-field stress required to initiate fracture propagation.

Finally, the influence of crack distance on failure is analysed for a set of cracks under compression (Fig. 6-17). The distance is calculated from the crack midpoint to the neighbouring crack's midpoint and the distance is the same in horizontal and vertical directions. The crack element length is 0.2 mm.

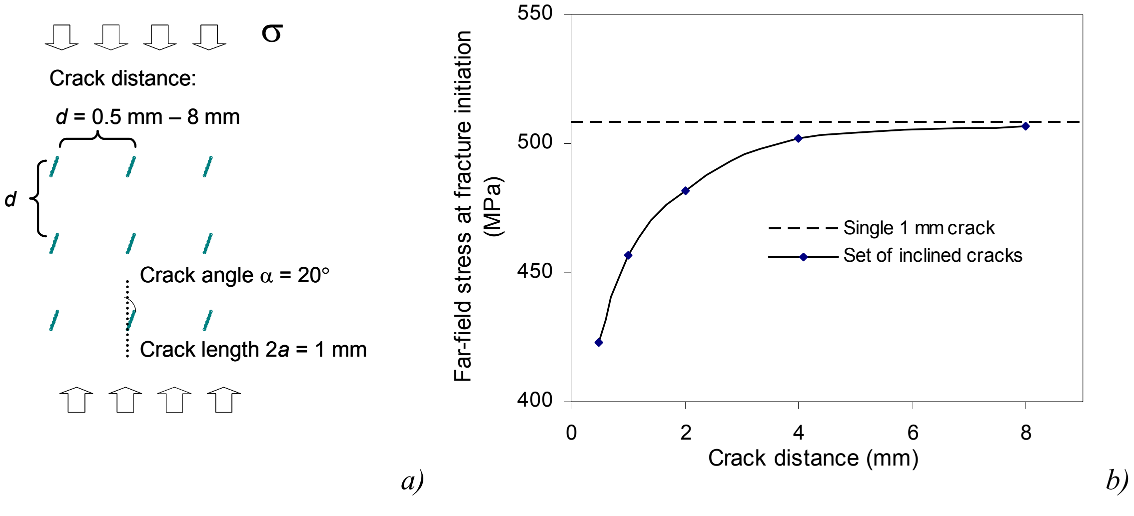

Figure 6-17. *a) Loading configuration for a set of inclined cracks; b) Far-field stress required for fracture initiation for a set of cracks.*

From the analysis of multiple cracks it is concluded that in addition to the crack density the number of cracks in the crack set also affects the applied load required to initiate fracture propagation. For the studied cases, the effect of closeness becomes apparent when the distance between the cracks is less than three times the crack length.

6.4 Direct tensile test model

The stress evolution and the failure process in the indirect Brazilian test are complex, because the compressive loading may give significant components of shear failure mechanisms. Although no successful results were attained in laboratory from the direct tensile tests, it has been modelled due to its simple loading configuration and because it clearly expresses the tensile failure mechanisms. Also, the difficulties reported for direct tensile testing by Backers (2006) have been analysed using the direct tensile test model.

6.4.1 Model description

The FRACOD model of the direct tensile test has a length of 125 mm and a width of 50 mm (Fig. 6-18). Because of the 2D-plane-strain assumption, the numerical specimen actually represents a long beam with cross-section dimensions of 125 mm × 50 mm. The stress evolution is controlled by axial displacement increments (*dy*) of the top boundary. At the top and bottom boundaries, shear movements are prevented ($dx = 0$) to simulate the glued contact conditions between the loading machine and the specimen. Asymmetric model was used. The intact rock properties as presented in Table 5-2 have been applied with a fracture toughness K_{IC} and K_{IIC} of 3.21 and 4.60 MPam$^{1/2}$, respectively.

The stress-strain response of the model is linear prior to the onset of new crack formation, i.e. it is not path dependent. Hence, the strain in the elastic region can be increased by large increments from the start. After detecting the first new crack formation, the vertical strain of 8×10^{-6} was applied in steps corresponding to a 0.5 MPa equivalent elastic stress increase. After reaching a stress level for unstable fracture propagation, the top boundary displacement was kept constant. The unstable fracture propagation can be identified in Fig. 6-21; the axial stress at the monitoring points on the top of the specimen decreases while axial strain (boundary displacement, *dy*) is kept constant.

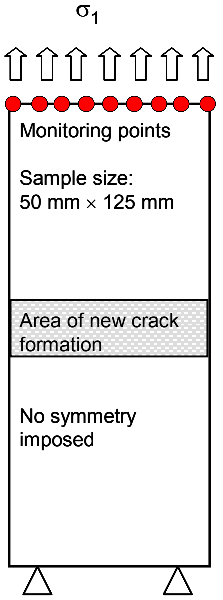

Figure 6-18. *Loading configuration of the direct tensile test model. The crack initiation can occur only in the central area of the model.*

6.4.2 Stress distribution and failure

The stress distribution in the elastic model of the direct tensile test is presented in Fig. 6-19. The loading refers to the stress state prior to failure when the total displacement of 28 μm (0.0224% of strain) corresponding to σ_I = 15.2 MPa tensile stress, is applied on the top boundary (Fig. 6-18). Both major and minor stresses are fairly evenly distributed in the middle section of the numerical FRACOD specimen. Near the top and bottom boundaries the stresses are disturbed due to prevented shear displacement, mirroring the friction at the contact between the loading plate and the specimen. The plot of the tensile stress distribution (Fig. 6-19b) suggests local stress concentrations in the vicinity of the specimen corners. It is not clear whether this is a real physical effect caused by restricted shear at the top and bottom boundaries or whether it is caused by a numerical inaccuracy close to a sharp corner.

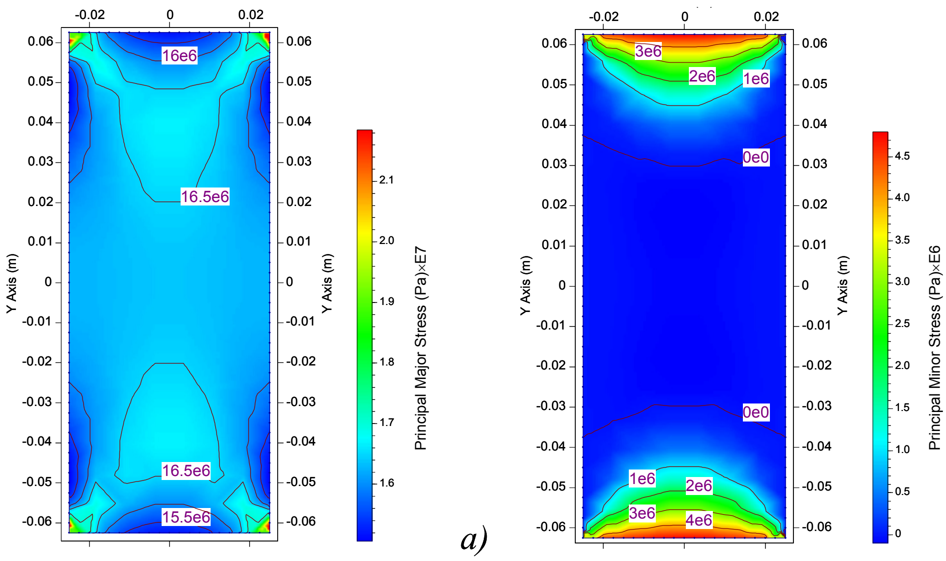

Figure 6-19. *Stress distribution in an elastic FRACOD model corresponding to the load (σ_I = 15.2 MPa) prior to tensile failure. a) Major stresses; b) minor stresses.*

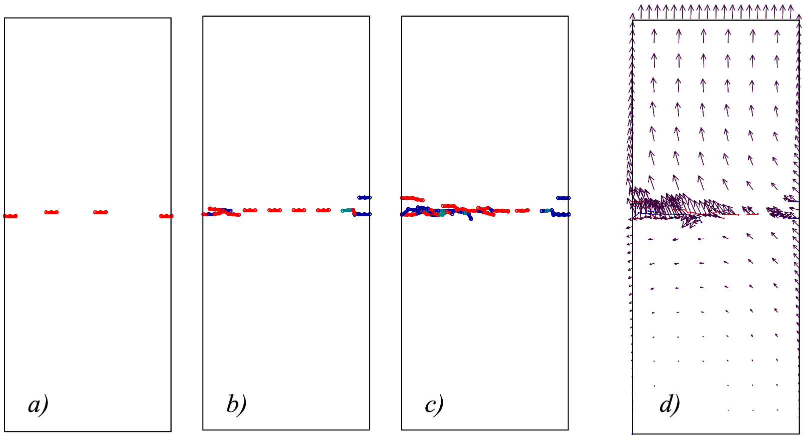

Figure 6-20. *Tensile failure modelled by FRACOD. Material parameters as presented in Table 5-2. Crack initiation is restricted to the central section of the model. The crack distance (from midpoint to midpoint) of the newly formed cracks is 7.4 mm and the crack length 2a = 3.125 mm. Arrows in (d) indicate the displacements.*

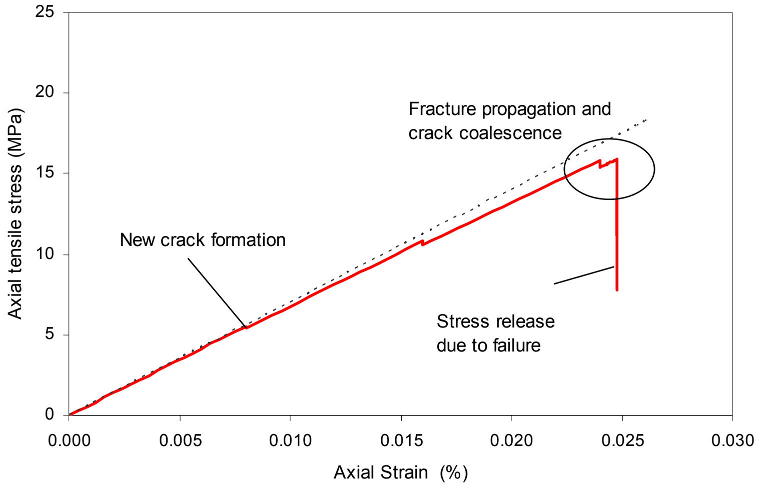

Figure 6-21. *Modelled stress-strain behaviour of the Äspö diorite subjected to tensile stress. Displacement is applied at the top boundary. Axial stress is averaged from monitoring points at the top of the specimen.*

Due to the applied tensile stresses the newly formed cracks are introduced perpendicular to the major tensile stress (Fig. 6-20a). In this model, the crack initiation is set to start at 20% of the short-term tensile strength (σ_t = 14.8 MPa). This reduced strength aims to represent micro-crack formation and local loosening of the rock material prior to crack propagation and macro-scale failure. This loosening of material can be considered as micro-cracking at the grain boundaries. Due to tensional loading conditions, grain boundaries perpendicular to the tensile stress are most critically oriented for micro-cracking.

The first crack appears at about 5 MPa average stress level corresponding to a strain of about 0.008%. New crack formation is detected as a slight deviation from linearity in the stress-strain curve (Fig. 6-21).

Increasing the load leads to an increase in new crack formation and finally to fracture initiation at an average stress of about 15.2 MPa. The extending crack links with the neighbouring crack (Fig. 6-20b) and the propagation ceases. A slight increase in strain leads to escalating crack growth and unstable failure (Fig. 6-20 c and d). The stress relaxation due to unstable fracture propagation can be detected as a sudden stress drop as shown in Fig. 6-21.

According to the model, the stress near the top and bottom boundaries is more irregularly distributed compared with stresses in the middle section (Fig. 6-19) and there are sections of increased stress close to the corners. The modelled stresses suggest that even if the gluing was done correctly, as discussed in Section 5.2.1, the failure is likely to occur in the top or bottom section of the specimen rather than in the middle section. For a real rock specimen, the sample preparation might have also introduced some damage at the ends of the specimen that furthermore guides the failure to occur in the vicinity of the loading plates.

In the previous example, the crack initiation was restricted to the central area of the model where the stress is evenly distributed (Fig. 6-19). The area of potential failure was set as a 10 mm wide band in the middle of the model (Fig. 6-18). If the initiation was not restricted, the failure starts close to the top or bottom boundaries, as shown in Fig. 6-22, not in the middle of the specimen as presented in Fig. 6-20.

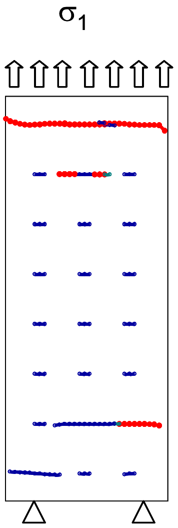

Figure 6-22. *Modelled uniaxial tensile failure of a rock specimen. Failure starts at the top boundary if not constrained to initiate in the central part of the model.*

6.5 Uniaxial and triaxial test models

Before considering the time-dependent effects on failure, short-term compressive strength test models were set up aiming to reproduce the general stress-strain behaviour observed for the Äspö diorite in laboratory. UCS and triaxial compression tests have been carried out on this rock type in several laboratory studies. The following FRACOD models refer to mechanical properties reported in Särkkä and Eloranta (2003), Kuula and Eloranta (2003), Jacobsson and Bäckström (2005) and to laboratory studies described in Chapter 5. The input parameters as listed in Table 5-2 are used.

6.5.1 Brittle failure under compression

According to laboratory observations the failure process in rocks under compression is more complex involving both stable and unstable crack propagation. Local failure in rocks occurs in directions of the major applied load and in the shear stress direction. Under uniaxial compression an isolated inclined crack starts to grow in a stable manner towards the major principal stress, forming the so-called wing cracks. Successively increased far-field stress is required to maintain wing-crack propagation. This is because when the wing crack grows, the angle between the major stress and the wing crack decreases, resulting in decreased stress intensity at the crack tip. After the stresses have reached a certain level, failure in the shear stress direction is more favourable from the point of view of the total energy of the system.

Under increasing stress cracks start to interact and coalesce. This linkage is often suggested as a possible mechanism for strain softening (Fakhimi and Fairhurst 1994), and it begins long before the uniaxial short-term laboratory peak strength of a rock sample. The final macroscopic failure occurs when cracks begin to coalesce in an unstable manner. A chain of cracks propagates both in shear and/or in tensile modes depending on the local heterogeneity of the rock.

An idealised synoptic model of damage development in a heterogeneous brittle solid under compression by Main et al. (1993) is presented in Fig. 6-23. (a) The first crack grows on the weakest element (upper left-hand diagram). The local probability of the fracture (right diagram) is reduced in a domain of a diameter *d* around this crack, but is slightly enhanced elsewhere. This implies that the sites of incremental crack growth initially tend to avoid each other. Damage progresses in a similar manner until the whole sample is pervaded by micro-cracks (b). At this stage, the deformation is optimally distributed and the local probability of a fracture has returned to a uniform level. (c) The first two cracks coalesce as an incipient shear fault. This leads to stress concentration and an increase in the probability of a fracture occurring around the nucleating faultlet, which grows rapidly to form a through-going fault. In reality, the transition from (b) to (c) will be gradual, and will have a statistical element that depends on the crack density. (d) Fault slippage closes the dilatant micro-cracks and further deformation is concentrated on and around the new fault.

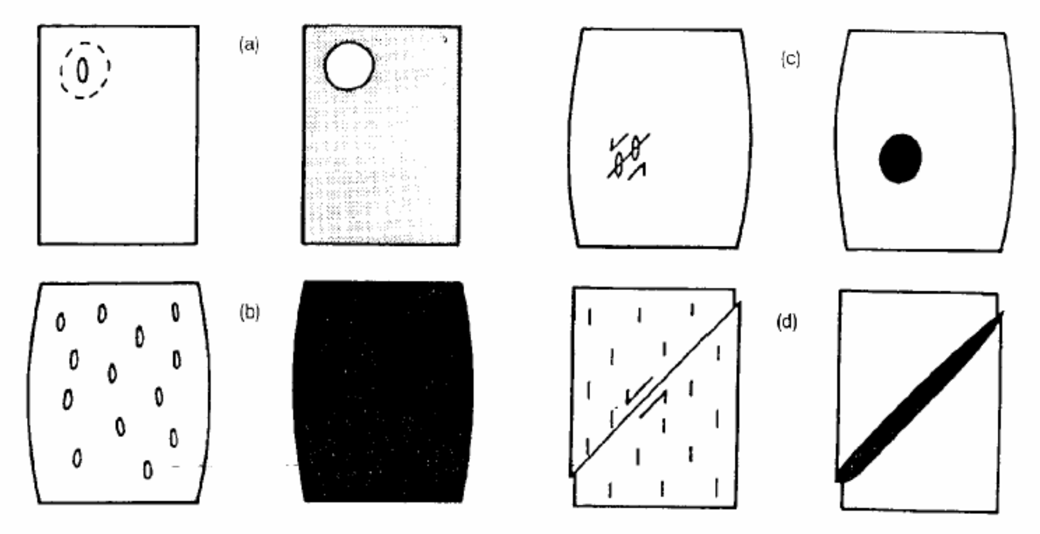

Figure 6-23. *Idealised synoptic model of damage development in a heterogeneous brittle solid under compression (Main et al. 1993).*

6.5.2 Model description

The dimensions of numerical 2D models presented here correspond to the laboratory specimens having an approximate length of 125 mm and a width of 50 mm (Fig. 6-24). The element size at the boundaries is e_b = 6.25 mm for all laboratory specimen models. Because the compression failure models involve a large number of simultaneously growing fractures, a symmetrical model is used to improve the accuracy and calculation capacity. In this study, symmetry against point x = 0 and y = 0 is used. Symmetry conditions against x-axis or y-axis symmetry could be used as well.

The input parameters as listed in Table 5-2 are used for wet conditions (K_{IC} = 2.74 MPam$^{1/2}$ and K_{IIC} = 4.46 MPam$^{1/2}$). The initial half-crack length is 1 mm and the crack density is 10 mm, defined as the crack midpoint distance (Fig. 6-17).

The top and bottom boundaries are restricted in shear movement to simulate the stiff contact conditions (i.e. strong friction) in laboratory tests. This is done using shear and normal displacement boundaries. Boundary conditions at the side walls are defined using normal stress boundaries.

An axial displacement is applied incrementally on the top boundary. As explained for the case of the tensile test model, the stress-strain response is not path dependent in the elastic region (intact rock model); hence, the size of the loading increments can be increased in large steps up to the onset of new crack formation. In the following models, the new crack formation is set to start at 121 MPa, corresponding to the crack initiation stress (σ_{ci}) reported for the Äspö diorite (Andersson 2004). The level of applied stress at new crack formation is given as an input parameter (β), as described in Section 4.4.2.

When the stress is close to this pre-defined crack initiation stress, the strain is increased in smaller steps, here by 2 µm (strain of 1.6×10^{-5}) corresponding to stress steps of about 1.1 MPa. The model stability is calculated by five cycles after every strain increment during the loading process. When a crack starts to propagate, every cycle will add a new element to the crack tip.

The axial stress in the specimen is detected at four monitoring points located on the top boundary of the model (A1-A4 in Fig. 6-24). The axial stress in the following stress-strain diagrams is presented as an average stress calculated at these monitoring points. The lateral displacement is calculated at four locations along the vertical edge (M1-M4).

The stress distributions in the UCS model are presented in Fig. 6-25. The figure shows the major and minor principal stresses in the elastic model for a strain of 3.76×10^{-3} corresponding to a 256 MPa average compressive stress.

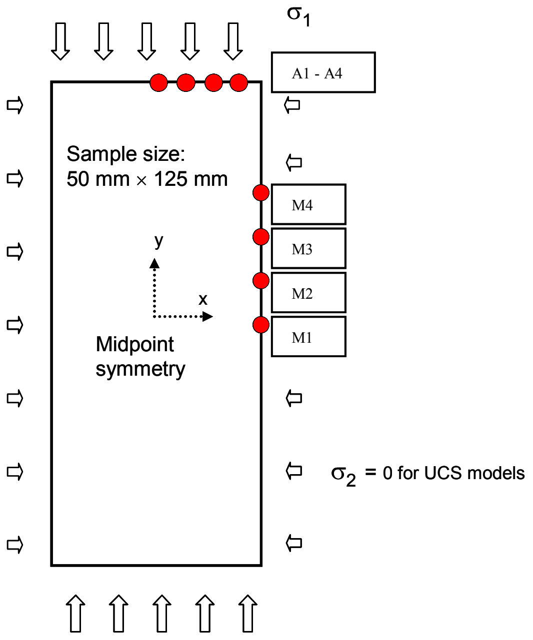

Figure 6-24. *Loading configuration for FRACOD simulations.*

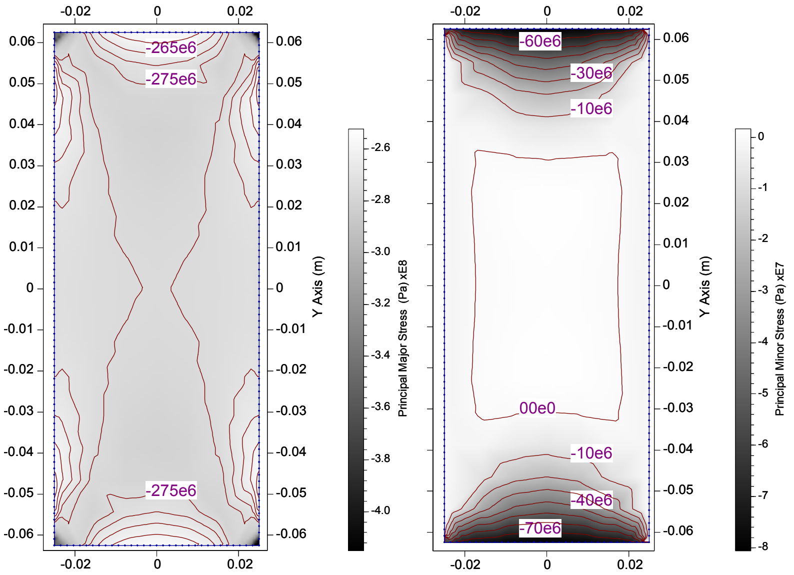

Figure 6-25. *Major and minor principal stresses in the UCS model. Elastic conditions for σ_1 = 256 MPa.*

6.5.3 Modelled structural breakdown

According to the numerical modelling results, the failure may start at various places in the specimen, except near the top and bottom boundaries where the friction causes confinement, which prevents the failure. The new crack formation was disallowed in the close vicinity of the specimen edge to avoid the possible incorrect fracture propagation caused by decreased accuracy close the boundary element (see Section 8.2).

As the stress increases the number of new cracks also increases (Fig. 6-26), resulting in accumulated inelastic strain (Fig. 6-27). However, the model is stable and further damage requires an increased level of stress. The stress versus displacement response is almost elastic, suggesting that no significant damage occurs.

Depending on the given properties of the newly formed cracks, they may slip or dilate according to the local loading conditions. In the current model, some of these new cracks slip when the average axial stress reaches a stress of 196 MPa. The number of slipping cracks progressively increases as the stress is increased.

The model suggests initial stable fracture propagation at a stress of about 291 MPa. When the stress is increased to a level equivalent to an axial stress of 293 MPa, continuing unstable fracture propagation occurs (peak strength). The following post-peak failure can be identified as a continuous decrease in axial stress. After reaching the peak stress, single cracks start to coalesce and to create large fracture traces. The failure involves crack propagation in both directions of the major principal stress and in the shear stress direction. The wing-crack propagation in the early phase of pre-peak failure is underestimated in this model compared with models containing finer model discretisation. Wing-crack propagation in uniaxial compression using higher model resolution is presented in Figs 6-1d, 6-2 and 6-5.

The maximum displacements (shear and normal displacement) at the fracture surfaces are small, about 50 µm. The extending fracture traces follow rough paths, deviating in a zigzag manner. The symmetrical shape of the failure is a consequence of a symmetrical model.

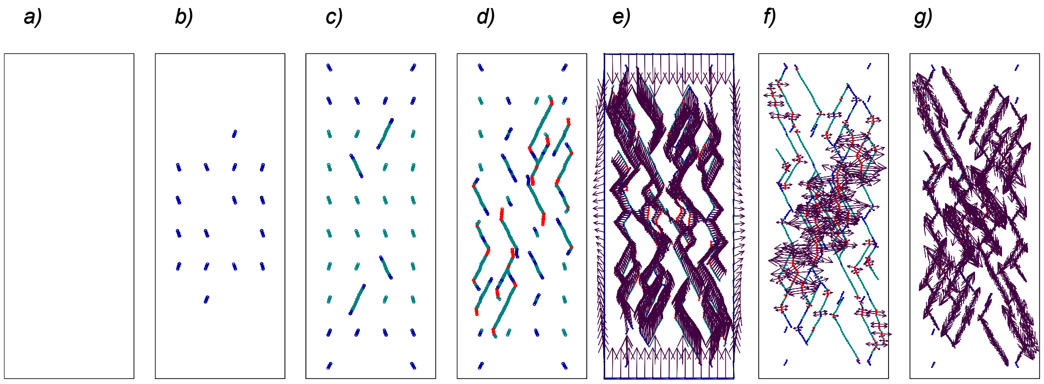

Figure 6-26. *Failure in the UCS test according to FRACOD simulation. Red marks an open fracture, green marks shear. a) Intact rock model; b) new crack formation; c) stable fracture propagation; d) unstable fracture propagation; e) displacements; f) maximum fracture aperture, dn = 46 µm ; g) maximum shear displacement, ds =50 µm.*

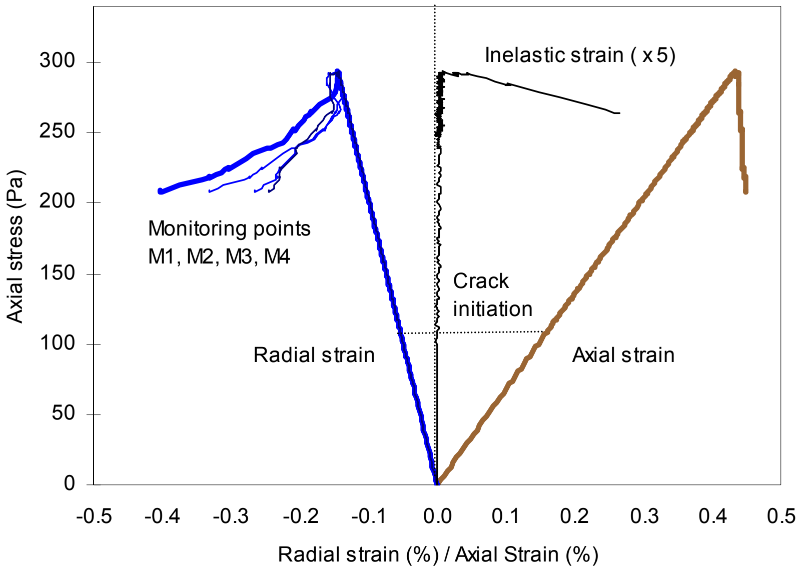

Figure 6-27. *FRACOD modelling of stress-strain behaviour of the Äspö diorite using monotonic axial strain increments at the top boundary and typical material properties for the Äspö diorite.*

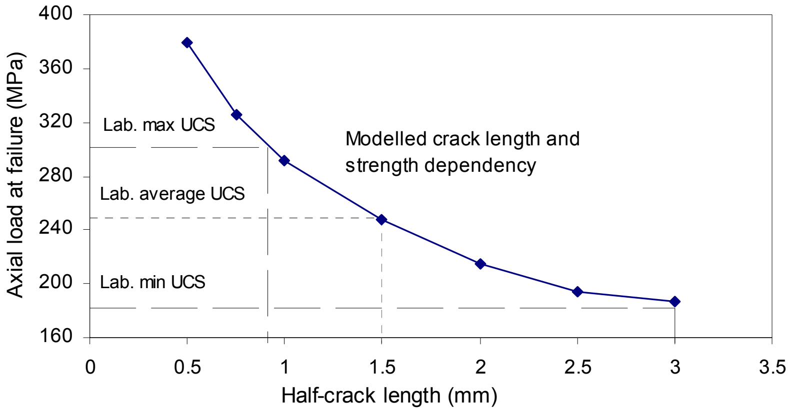

Figure 6-28. *The relationship between the initial crack sizes versus peak strength. FRACOD model behaviour as calculated for the Äspö diorite in wet UCS test conditions.*

The assigned length of newly formed cracks significantly affects the failure strength, as was presented in Section 6.3.1 for tensile loading conditions. The length of newly formed cracks versus the peak strength for UCS models is presented in Fig. 6-28. All material parameters are the same as in the presented UCS model, except that the initial (half) crack length ranges from $a = 0.5$ mm to 3.0 mm. According to Fig. 6-28, the calculations suggest that the critical half-crack length of the UCS-tested Äspö diorite is between 1 mm and 3 mm. The average laboratory strength is 249 MPa, corresponding to an initial half-crack length of 1.5 mm. The modelled critical crack length is in the range of the average grain size (1.28 ±1.61 mm) reported for the Äspö diorite, see Section 5.1.

6.5.4 Class II post-peak behaviour

In determining the mechanical properties of brittle rocks, such as the uniaxial tensile strength σ_t and the uniaxial compressive strength σ_c, one is more concerned about the pre-peak elastic behaviour of the brittle rock, which does not have some of the difficulties of the post-peak non-linear behaviour. One of the main difficulties lies in the testing systems used to determine the strength of the rock specimens, since they become unstable as soon as the peak of the stress-strain characteristic is passed and its slope becomes negative. This indicates that an unstable or dynamic fracture process occurs in the specimen and that kinetic energy is generated (Whittaker et al. 1992). It is important to understand the post-peak behaviour of rock failure and how the energy is absorbed in the failure process when studying the sudden progressive failure, such as it occurs in rockbursts and earthquakes. Special techniques are needed to detect the post-peak stress-strain behaviour in the laboratory. Such techniques are, for example, the use of the constant radial strain rate of the specimen as a control variable for the axial load (Section 5.2.2) or using a linear combination of stress and strain as the control variable, as described by Okubo and Nishimatsu (1985).

Considering the post-peak axial deformational behaviour of a loaded rock specimen, rock types are classified into Class I or Class II (Fig. 6-29) according to Wawersik and Fairhurst (1969). Class I behaviour is characterised by 'stable' fracture propagation, in the sense that work must be done on the specimen to effect further reduction in load-bearing ability. Hence rocks that exhibit Class I behaviour retain some strength even after the compressive strength has been exceeded. The specimen will only fail by continuous movement of the machine platens.
In contrast to 'stable' fracture development, failure for Class II post-peak behaviour is unstable or self-sustaining, i.e. the elastic strain energy stored in the sample when the applied stress equals the compressive strength is sufficient to maintain fracture propagation until the specimen has lost virtually all strength. To control the fast failure process the surplus strain energy must be removed from the system. In practice, this is done by moving the loading plates in the opposite direction. The dividing line between Class I and Class II post-peak behaviour is defined by the dashed line in Fig. 6-29, which represents the case when the stored elastic energy just balances the energy required to produce total breakdown of the specimen.

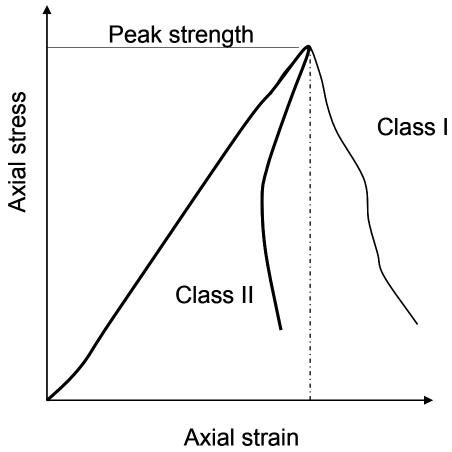

Figure 6-29. *Representative stress-strain curves for Class I and Class II post-peak axial deformation behaviour in uniaxial compression (modified from Wawersik and Fairhurst, 1969).*

Laboratory tests on the Äspö diorite suggest a Class II behaviour (see Fig. 5-8). The radial strain control of the testing machine enables the post-failure Class II behaviour to be followed. At the

peak strength, the axial loading rate is decreased to zero and the direction of the loading piston is changed in a controlled manner, aiming to produce a constant rate of radial expansion.
In the actual laboratory test, the energy stored in the loading machine may also contribute to a sudden specimen failure (Hudson et al. 1972). By numerical modelling it is possible to study the failure process without the effects caused by unloading of the adjacent element, as illustrated in Fig. 2-7, i.e. to simulate a loading machine with infinitely high stiffness.

To simulate the Class II behaviour, unloading of the model presented in Section 6.5.3 was started after passing the peak strength using similarly sized strain increments but in the opposite direction as was used in the loading phase. Two calculation cycles were applied for each unloading increment during the unstable phase of fracture propagation. The progressing failure is detected by the increased radial strain while the axial strain is decreased, as expected for Class II behaviour (Fig. 6-30).

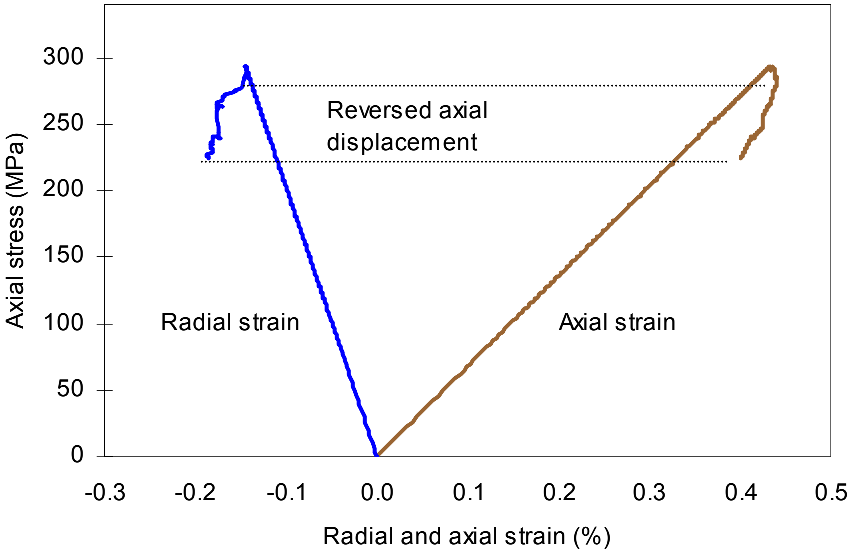

Figure 6-30. *FRACOD modelling of axial and radial stress-strain behaviour using typical rock parameters for the Äspö diorite. Reversed axial displacement at peak stress results in Class II type post-peak behaviour.*

Figure 6-27 shows to some extent Class I type post-peak behaviour. This is because the axial strain in the model is increased during the failure process, i.e. while the cracks still propagate. If the strain increase was stopped when unstable failure was detected (at peak stress), the post-peak stress-strain slope would be vertical.

6.5.5 Damage controlled test model

To study the progressive failure in the laboratory, a so-called damage controlled test can be conducted (Martin 1997). The minimum load value that increases the damage in rock is tracked by the cycling load. The load is repeatedly released at peak conditions. The locus of damage is a path of the critical stress-strain point defined separately for each loading ramp. Peak loads obtained from cyclic and monotonic procedures are suggested to be about the same magnitude (Backers 2005). The data from triaxial tests performed on Lac du Bonnet granite were used in the DECOVALEX project in order to study the degradation of elastic properties (Nguyen and Jing 2007). The work involved numerical simulations of laboratory-tested granite samples (Fig. 6-31).

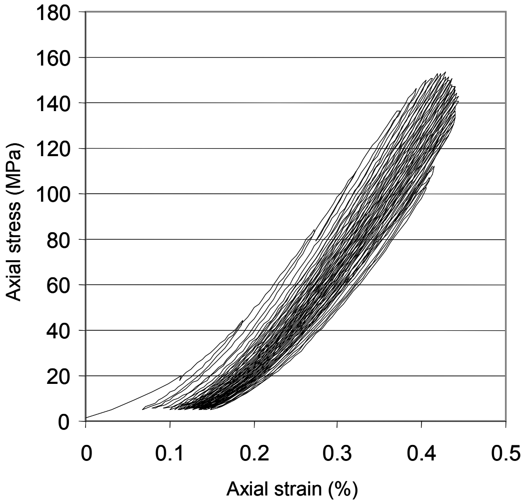

Figure 6-31. *Rock damage laboratory experiment performed on Lac du Bonnet granite (DECOVALEX Workshop presentation Kunming; Nguyen, 2005).*

To test the capacity of the FRACOD to model such a loading-unloading-reloading process, the Äspö diorite properties were used for an initially intact model specimen. Simulated cyclic loading and related stress-strain curves are presented in Fig. 6-32. The failure locus in the cyclic loading model also suggests Class II behaviour for the Äspö diorite.

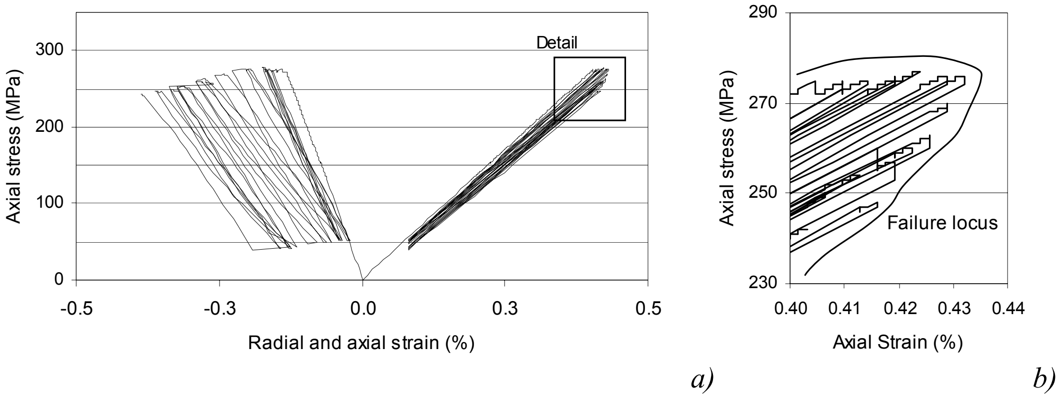

Figure 6-32. *a) FRACOD-simulated cyclic loading using typical Äspö diorite parameters; b) detail of the axial strain vs. axial stress at peak conditions.*

6.5.6 Griffith locus and post-peak failure behaviour

By considering the energy changes associated with crack propagation, the non-linear locus of failure can be determined by a curve called the Griffith locus (Berry 1960; Cook 1965; Whittaker et al. 1992; Jaeger et al. 2007).

Referring to Fig. 2-1a, which shows an infinite plate containing a flat elliptical crack in tension, assume that the applied stress σ is constant, i.e. a 'dead-weight loading condition'. Following the derivation presented in Whittaker et al. 1992 (see Section 2.2), the total stored strain energy in the plate in the presence of the crack is the sum of U_t and U_c. Due to the work done by the external force this increases the strain energy for the system, U_c, which is taken as a positive. Thus:

$$U_t + U_c = \frac{\sigma^2 A}{2E'} + \frac{\pi \sigma^2 a^2}{E'} \tag{6-1}$$

The work done by the external force prior to crack extension, W, is:

$$W = \frac{\sigma \cdot \varepsilon \cdot A}{2} \ , \tag{6-2}$$

the equilibrium state is:

$$W = U_t + U_c \text{ , i.e.} \tag{6-3}$$

$$\frac{\sigma \varepsilon A}{2} = \frac{\sigma^2 A}{2E'} + \frac{\pi \sigma^2 a^2}{E'} \tag{6-4}$$

from which the strain, ε, can be obtained by:

$$\varepsilon = \frac{\sigma}{E'} + \frac{2\pi\sigma \cdot a^2}{A \cdot E'} \tag{6-5}$$

The critical crack length, a, can be defined from Eq. (2-5):

$$a_{cr} = \frac{2\gamma_s \cdot E'}{\pi \cdot \sigma^2} \tag{6-6}$$

Substituting this into Eq. (6-5) gives:

$$\varepsilon = \frac{\sigma}{E'} + \frac{1}{A} \cdot \frac{8{\gamma_s}^2 \cdot E'}{\pi \cdot \sigma^3} \tag{6-7}$$

Equation (6-7) is the expression of the Griffith locus for tensile conditions (Berry 1960). Using the relationship:

$$K_I = \sqrt{2 \cdot E' \cdot \gamma_s} \tag{6-8}$$

and the critical condition when $K_I = K_{IC}$, we get the Griffith locus in terms of fracture toughness:

$$\varepsilon = \frac{\sigma}{E'} + \frac{1}{A} \cdot \frac{2K_{IC}{}^{4}}{E' \cdot \pi \cdot \sigma^{3}} \tag{6-9}$$

The Griffith locus for the tensile condition is shown in Fig. 6-33. Typical values for material parameters as applied in an analytical example for a cracked finite plate in tension presented by Cook (1965) have been used. The surface energy (γ_s = 100 1×10^{-3} ergs/cm^3) is recalculated to fracture toughness (K_{IC} = 3.65 MPam$^{1/2}$) using the relation in Eq. (6-8). Young's modulus E = 50 GPa and Poisson's ratio ν = 0.25 have been used.

FRACOD far-field stress models were set up to express the Griffith locus and to compare the results with analytical calculations. The critical applied stress for fracture initiation was detected for cracks with varying lengths. Because the strain release caused by the crack, $\varepsilon(a_{cr})$, corresponds to the crack length, the displacements above the crack were monitored at the critical level of the far-field stress. The displacement was multiplied by a factor, D, analogous to the geometrical term $1/A$ in Eq. (6-7), and added to the strain of the un-cracked medium. The total strain above the crack is then:

$$\varepsilon_{tot} = \frac{\sigma_{cr}}{E'} + D \cdot \varepsilon(a_{cr}) \tag{6-10}$$

The constant D = 16.2 gives the best fit for displacements monitored 5 m above the midpoint of the crack with the analytical solution (A = 1). This procedure reflects the strain measurements in physical tests. Alternatively, the Griffith locus can be approximated more directly by calculating the crack deformation along the crack surface, or by implementing the detected critical crack length ($a = a_{cr}$) and the critical stress ($\sigma = \sigma_{cr}$) into Eq. (6-5). The aforementioned measures yield similar results with the analytical solution, providing that the geometrical term A is adapted to the considered block volume.

From Fig. 6-33, it can be noted that an almost perfect match is attained from numerical modelling compared with the analytical solution for Griffith locus. The modelled non-linear strain from critical cracks (crack deformation) corresponds to the non-linear term in the analytical solution (the power law term in Eq. 6-7). Note the analogy and comparable asymptotic shape of the critical crack length (a_{cr}) versus the far-field stress (σ) curve in Fig. 6-7 and the non-linear term in Fig. 6-33.

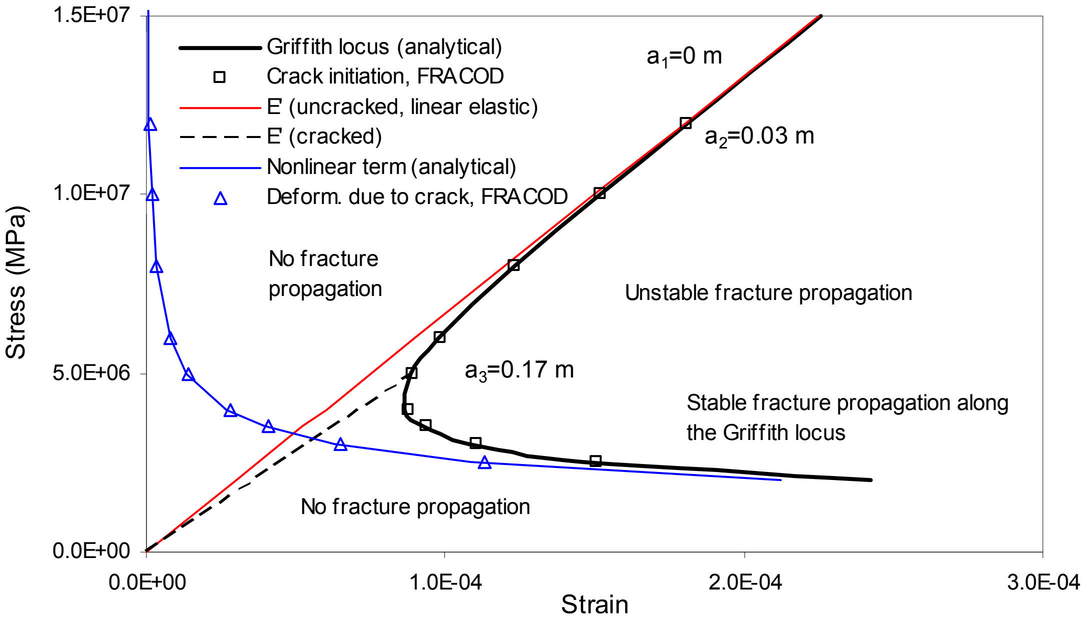

Figure 6-33. *The Griffith locus defining the non-elastic behaviour in tension. Analytical solution and FRACOD approximation.*

It can be seen that the failure locus is asymptotic to the intrinsic modulus slope, which corresponds to a crack length equal to zero ($a_1 = 0$ m). For any crack length, the stress-strain response is linearly elastic until it intersects the Griffith locus at some point. For example, at the point a_3, which corresponds to a half-crack length of 0.17 m, the critical stress level for fracture propagation is just satisfied at $\sigma = 5$ MPa, and the broken line expresses the modulus of the cracked body before further propagation. If the stress is reduced during the crack extension to exactly follow the Griffith locus, then the criterion is continuously just satisfied and the crack grows quasi-statically without accelerating, i.e. in a stable manner.

According to Cook (1965), the equations describing the Griffith locus for tension and compression have similar forms, except that for compression the friction between the crack faces must be considered. The fracture initiation locus for an inclined crack, as presented in Fig. 6-9a, was determined by FRACOD using the typical Äspö material parameters as were used in the numerical UCS test presented in Section 6.5. Because compression of an inclined crack involves Mixed-mode I-II loading conditions, both G_{IC} and G_{IIC} (or K_{IC} and K_{IIC}) must be considered. The effect of two fracture friction angles was considered and the fracture cohesion was set to $c_f = 0$. The critical levels of stress were registered from the model for varying crack sizes ($a = 0.8$ mm to 10 mm) and these values were implemented in Eq. (6-5). The geometrical term $A = 2.5\times10^{-4}$ was used to reflect the finite sample size (r = 0.025, l = 0.125). The modelling was performed for a uniaxial compressive stress and with a confining pressure of 10 MPa. The effect of the fracture friction angle ($\phi_f = 35°$ respective $\phi_f = 49°$) and the confining pressure is presented in Fig. 6-34. Similarly shaped stress-strain behaviour for the critical crack state is observed for compressive loading conditions as was detected for tensile failure (Fig. 6-33).

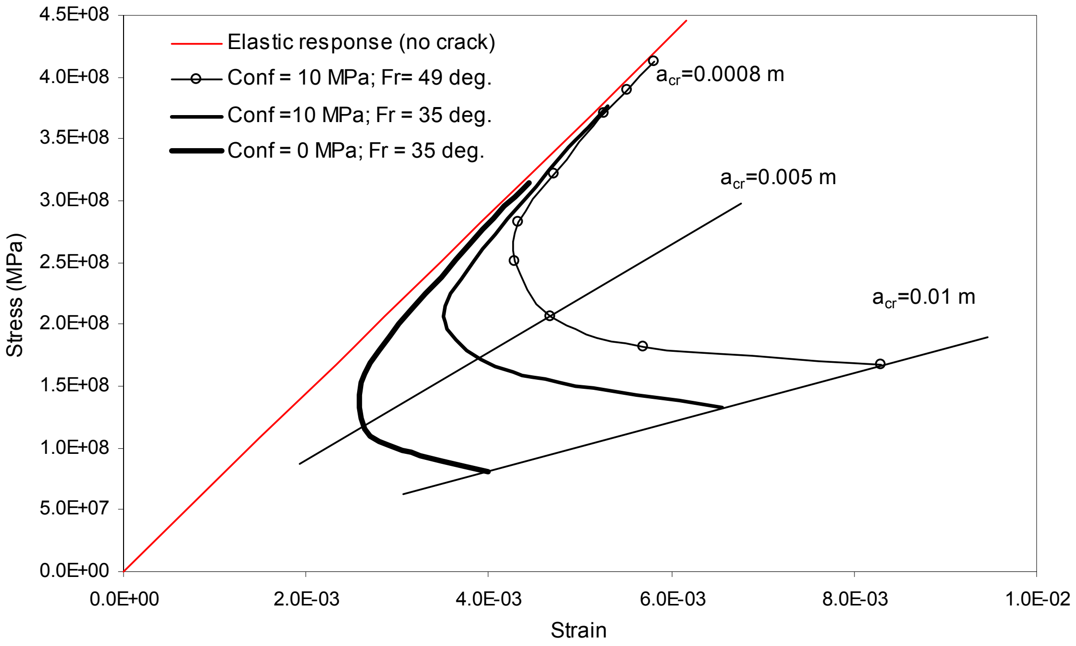

Figure 6-34. *Crack initiation locus in compression as modelled by FRACOD for a single inclined crack.*

Equations presented for Griffith locus are exact for a single crack in an infinite plate. For the case of more than one crack, these equations are shown to be valid, providing that the term A is replaced by a factor relating to the number of cracks (Cook 1965).

Stable crack propagation is physically defined by Bieniawski (1967) as the failure process by which crack growth is a function of the loading and can be controlled consequently. This case corresponds to the stored strain energy just supplying the surface energy required to extend the crack. Therefore, stable or unstable crack propagation depends on whether it is possible or not to follow the Griffith locus. Beyond the locus the crack propagation is unstable (Fig. 6-33) and the surplus energy corresponds to kinetic energy. Some of this kinetic energy is dissipated through vibrational energy and it can be related to acoustic emission, rockbursts or earthquakes. At the laboratory scale, the unstable fracture propagation leads to catastrophic rupture of the specimen. From the shape of the locus it can be seen that at low failure stresses, corresponding to the fracture initiation of long cracks, the system becomes more stable in the sense that the strain must be increased to sustain crack propagation.

Comparing the shape of the stress-strain curve of Class II post-peak behaviour and the Griffith locus, it is obvious that the registered phenomena in the laboratory can be related to the energy balance theory. As presented in Section 4.1, the failure criterion of FRACOD is based on the energy balance approach (Section 2.2), hence the modelled stress-strain behaviour obeys the Griffith locus and reflects the Class II post-peak behaviour observed by physical tests. The Class II type failure locus for multiple cracks according to FRACOD modelling is presented in Figs 6-30 and 6-32.

It must be noted that the locus in compression as presented in Fig. 6-34 is the fracture initiation locus, and not necessarily the failure locus, because at low confinements, fractures may grow as stable wing cracks, i.e. the system must be supplied with more energy (strain) to sustain the crack extension.

6.5.7 Triaxial compressive strength test models

The effect of confinement on peak strength was modelled using the same model geometry, material parameters and loading increments as described for the UCS model. A monotonic axial strain increase was applied. That is, five calculation cycles are applied after every strain increment during the loading process, even if the peak strength is reached. The monotonic increase of axial load is applied by 2-µm boundary displacement steps (0.0016%), corresponding to about a 1.1 MPa stress increase. The confinement (between 0 MPa and 50 MPa) was applied on the numerical FRACOD specimen before axial loading.

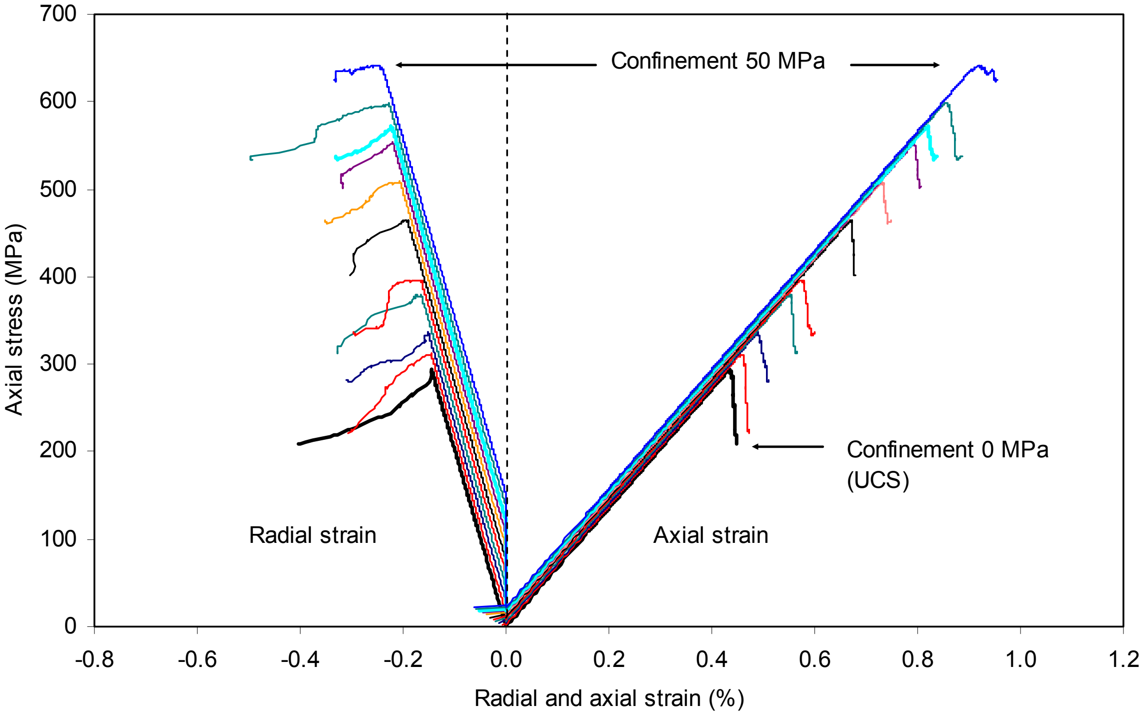

Figure 6-35. *Biaxial compressive stress-strain curves for confined FRACOD models using monotonic axial loading.*

In the biaxial models, the stress level required for new crack formation increases linearly with increasing confinement due to constant intact rock friction angle (ϕ_i), constant intact rock cohesion (c_i) and because of a constant portion ($\beta = 68\%$) of the strength to form new cracks is used. Constant fracture toughness (K_{IC}/K_{IIC}) and constant fracture friction angle (ϕ_f) are also used and the increased peak stress with increased confinement is caused by increased friction at the fracture surface. Hence, the stress level for fracture propagation can also be expected to show a linear relationship (Fig. 6-36).

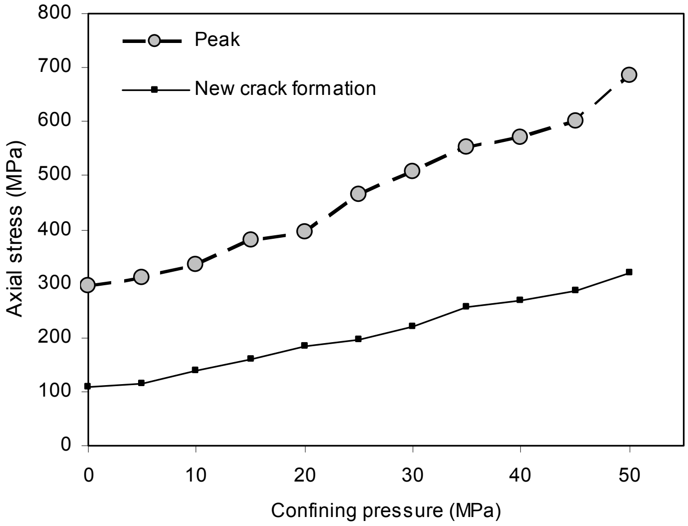

Figure 6-36. *Calculated effect of confinement on new crack formation and peak strength (Äspö diorite material parameters, a = 1 mm).*

Rao (1999) suggests that Mode II fracture toughness increases linearly with the increase of compressive stress (σ) on the notch plane. According to Backers (2005) the fracture toughness increases bilinearly with the increase in confining stress and shows a change in slope at about 30 MPa for the Äspö diorite. The tests by Backers were performed for a confining stress from 0 MPa to 70 MPa, as shown in Fig. 6-37. Figure 6-38 shows the results from uniaxial and triaxial strength test models of the Äspö diorite using confining pressures of 0, 5, 10, 15, 20, 30, 50 and 70 MPa and corresponding fracture toughness values of 4.6, 7.1, 8.8, 10.0, 10.9, 11.9 and 12.7 MPam$^{1/2}$ for 50 and 70 MPa, as suggested by Backers (2005). The peak strength response is consequently roughly bilinear. Due to the restricted number of UCS and triaxial laboratory tests and due to the large scattering in the laboratory results (Fig. 8-6), it was not clarified whether the strength of the Äspö diorite obeys a linear, bilinear or some other relationship for strength and confining pressure.

Model discretisation affects the uniformity of the model results and the fluctuation of the curve. The mode of fracture initiation and probability approach used for new crack formation might also affect the variation of the results.

In Fig. 6-39, the effect of a confining stress on the fracture pattern is presented (model with varying K_{IIC}). As the confinement increases the wing-crack growth and adjacent crack dilation are suppressed. The effect of confining pressure is also presented in Section 6.2 using improved model discretisation (Fig. 6-6).

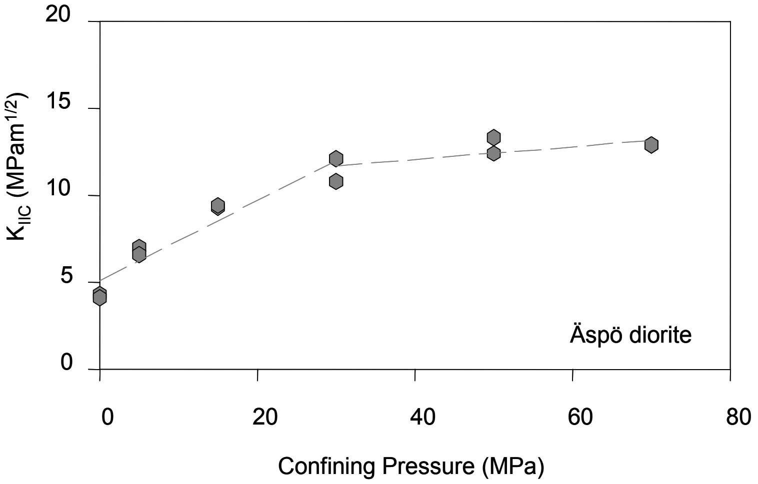

Figure 6-37. *Influence of confining pressure on Mode II fracture toughness (KIIC) for the Äspö diorite (Backers 2005).*

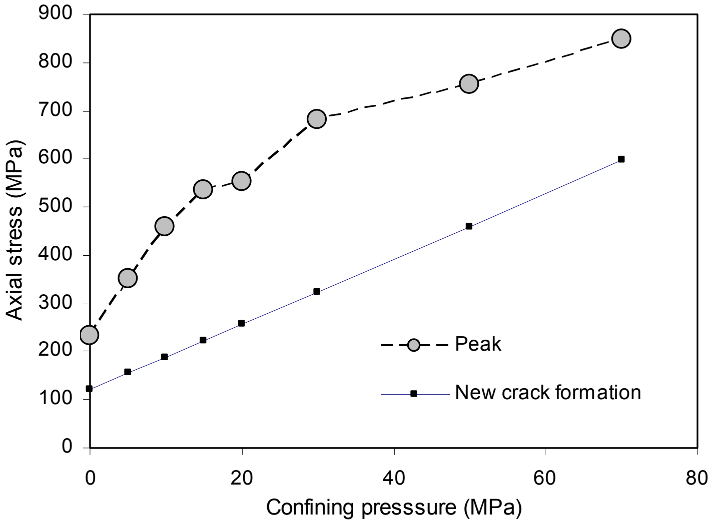

Figure 6-38. *Calculated effect of confinement on fracture peak strength using stress-dependent Mode II fracture toughness (K_{IIC}) as suggested by Backers (2005). Äspö diorite material parameters have been used with an initial half-crack length of a = 1.6 mm (Rinne et al. 2006).*

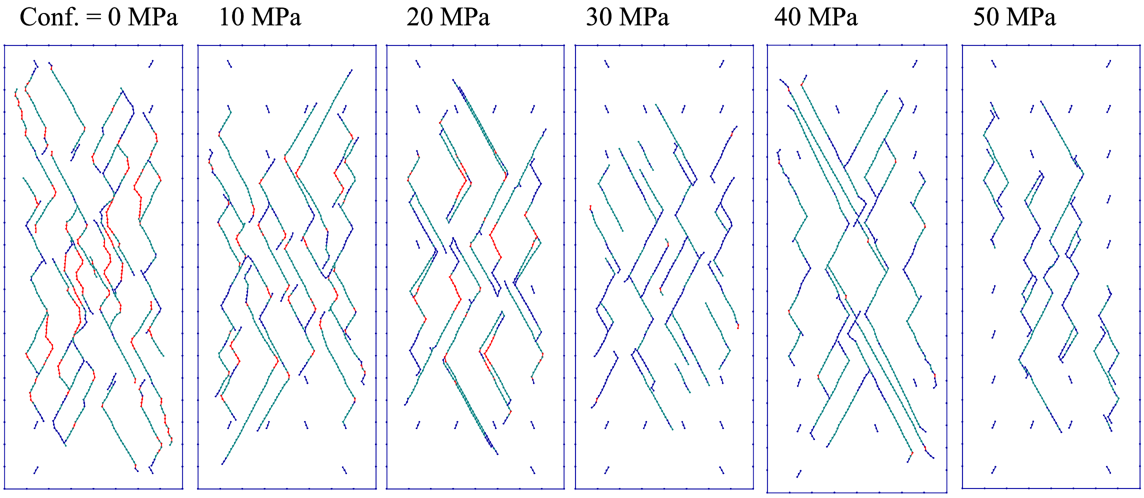

Figure 6-39. *Fracture pattern for biaxial compression tests for confining pressure between 0 and 50 MPa according to FRACOD modelling.*

6.5.8 Specimen specific models

The radial post-peak stress-strain response varies very strongly from one laboratory test to another. The radial strain varies strongly even if the tested specimens look homogeneous on visual inspection. Efforts were made to simulate accurately both the axial and lateral strain of individual radial-controlled laboratory tests. Figure 6-40b presents a FRACOD model aiming to replicate the stress-strain response including the loading and unloading sequences of the physical test (Fig. 6-40a). It proved to be complex to model simultaneously the true axial and radial response in the post-peak region of a specific test. The general stress–strain response was, however, reflected.

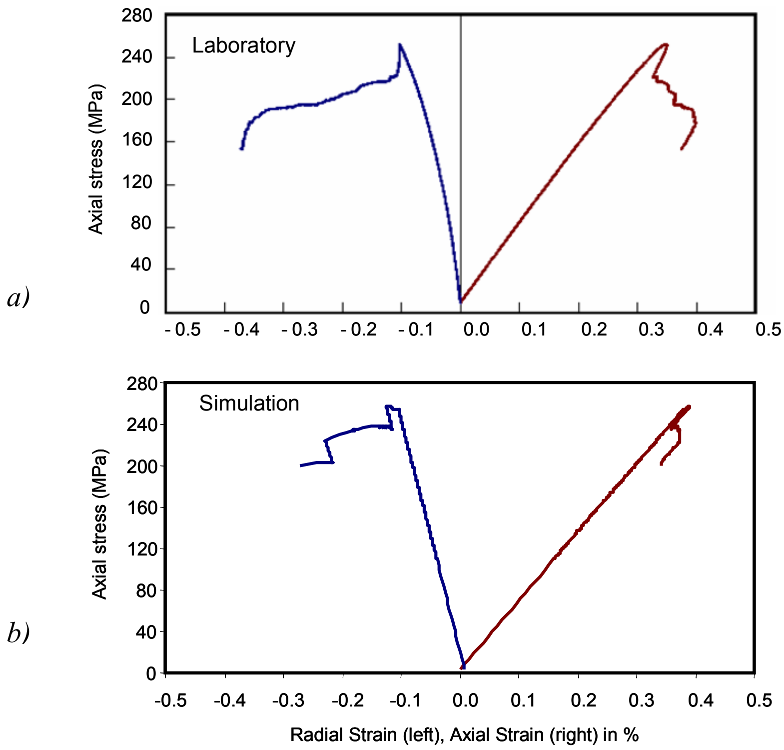

Figure 6-40. *a) Radial strain controlled triaxial compression test of the Äspö diorite with 7 MPa confinement (Staub et al. 2004); b) FRACOD simulation.*

According to the numerical modelling the failure may start at different places in the specimen and the radial response of the brittle failure depends on where the radial expansion is measured. Figure 6-27 shows the modelled radial response at four monitoring points (Fig. 6-24). A propagating fracture near the monitoring point strongly affects the radial response of the model, especially if a detached rock piece is developing. This kind of local expansion and chipping was also observed in some laboratory tests.

7 TIME-DEPENDENT FRACTURE MODELLING

Many laboratory investigations have revealed that the peak strength of rock is affected by the loading rate (Schmidtke and Lajtai 1985; Lajtai and Bielus 1986; Helal et al. 1988; Lockner 1993, 1998; Szczepanik et al. 2003; Antikainen 2007). The strain increments presented in the previous UCS and triaxial models were not related to time and therefore the true loading rate was not properly simulated. To model the actual influence of loading rate, the velocity of the fractures has to be linked to time and strain. In this chapter, we consider the rock failure as a time-dependent process using the SCG model described in Chapter 3. All material parameters used refer to Äspö diorite (water-saturated condition), including the SCG parameters, as presented in Table 5-2.

7.1 Tensile failure

A model for testing the capacity of the new SCG function was set up. The aim of this model was to simulate the time-dependent stress relaxation and the failure in tensile stress conditions. A constant tensile axial strain was applied to the model by using a loading rate of about 500 Pa/s, until an initial average tensile stress of 10 MPa is reached (Fig. 7-1). The specimen size (50 mm × 120 mm) is the same as in the previous models and the parameters for water-saturated Äspö diorite are used (Table 5-2). The crack length of the horizontal pre-existing crack is $2a = 20$ mm and is defined by 50 elements.

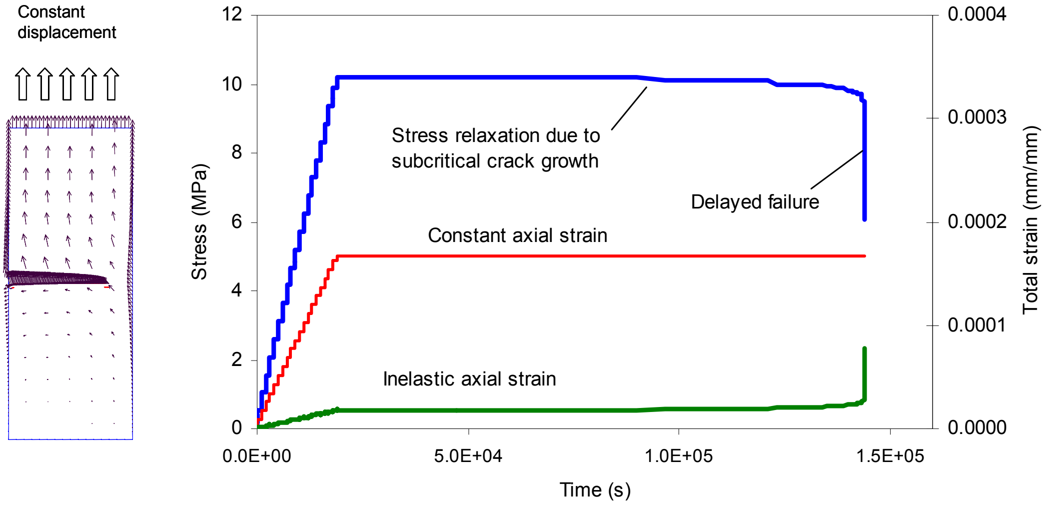

***Figure 7-1.** FRACOD modelling of delayed failure caused by subcritical crack growth in a specimen with a pre-existing horizontal crack subjected to a constant tensile strain.*

The first SCG element appears in the model after 9.68×10^4 s (~ 27 h). The delayed failure takes place after about 1.44×10^5 s (~ 40 h). If the crack was discretised in more elements, the stress relaxation due to SCG could be detected earlier. The total amount of crack growth prior to delayed failure is, however, not significantly affected by the model resolution because the calculated SCG is temporarily stored in the memory and accumulated until SCG reaches one element in length. Model discretisation, however, also affects the TTF, because the model accuracy affects the stress intensity as will be described in Section 8.2.

7.2 Triaxial and Strain Rate Stepping test models

7.2.1 Evaluation of the laboratory test results

Evaluations of the triaxial and SRS laboratory tests were made in order to decide on representative experiments for modelling. To evaluate how well the UCS, Triax and SRS test strengths correlate with the grouping of the six 'samples' (as described in Section 5.2) all strength test results are shown in the diagram presented in Fig. 7-2. A large scatter and inconsistency in results are observed if no grouping of the tests is considered. For instance, UCS strength in Samples 3 and 6 is higher than the Triax strength in Samples 1 and 2. The average peak strength for Triax tests is the same for testing at 2 MPa and at 7 MPa confining pressures (Table 7-1).

However, tests made on specimens from a short section of a drill core (i.e. specimens that belong to approximately the same location) show reasonably consistent behaviour: the peak strength increases with increasing confining pressure. Only Sample 2 shows a slightly lower strength for 2 MPa confinement strength compared with the adjacent UCS test (Fig. 7-2). The distance between the UCS specimen and the Triax specimen within a sample is about 1 to 2 m. The distance between the Triax and SRS tests within a sample is less, in most cases only a few centimetres.

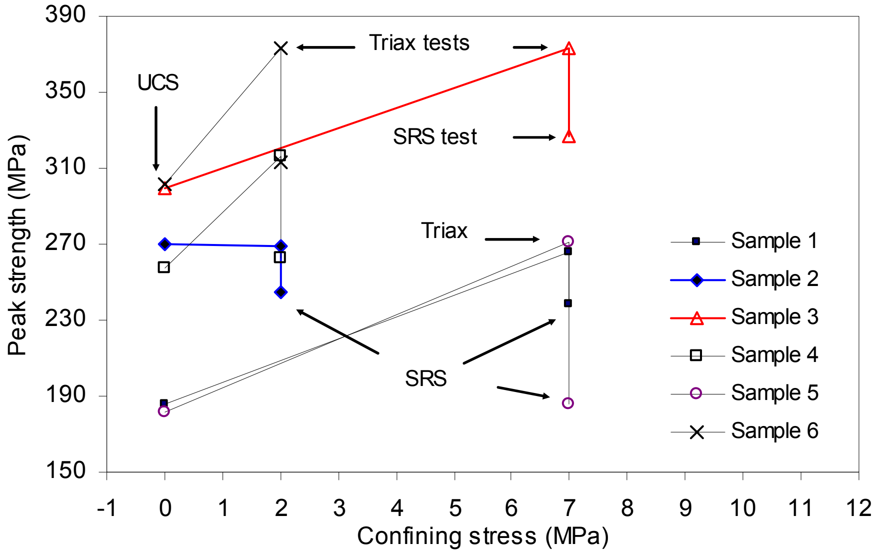

Figure 7-2. *Peak strength for specimens taken from six drill core sections (Samples 1-6) of the Äspö diorite. Each sample is subjected to UCS, triaxial and SRS testing conditions.*

Table 7-1. Average peak strength and strain at peak stress for Samples 1-6.

Standard triaxial tests			**Unit**
Confining pressure	2	7	MPa
Peak strength	319.2	319.2	MPa
Axial strain at peak stress	4.63E-03	4.77E-03	mm/mm
Strain Rate Stepping tests(*)			**Unit**
Confining pressure	2	7	MPa
Peak strength	279.5	290.2	MPa
Axial strain at peak stress	4.15E-03	4.81E-03	mm/mm

(*) Sample 5 is excluded.

Five triaxial and SRS test pairs (samples) out of six were successful for TTF analyses. The SRS test from Sample 5 was unsuccessful due to uncontrolled and unexpected failure during the first slow-loading step. It shows much lower strength compared with the other SRS tests (Fig. 7-3). Also the triaxial test from Sample 5 shows unclear peak behaviour. Sample 5 is included in the figures (Figs 7-3, 7-4 and 8-6). The test results are, however, not included in the analysis concerning average time-dependent behaviour (Table 7-1).

For all tested triaxial and SRS test pairs, the peak stress is significantly lower as the loading rate is decreased and the loading time is increased from a few minutes (standard triaxial tests takes about 5-8 min) to many hours (SRS test takes about 17-33 h) (Fig. 7-3). Hence, the strength results within the sample show consistent behaviour in terms of time-dependent strength. The drop in peak strength is more pronounced at a 2 MPa confining pressure (12%) compared with the stress drop with a 7 MPa confining pressure (9%).

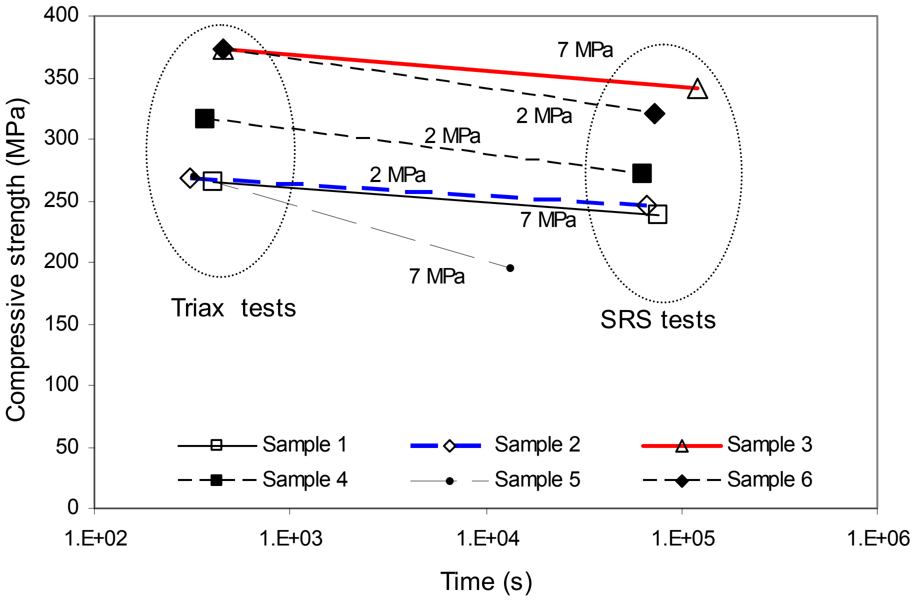

Figure 7-3. *Time to failure and compressive strength for the Äspö diorite.*

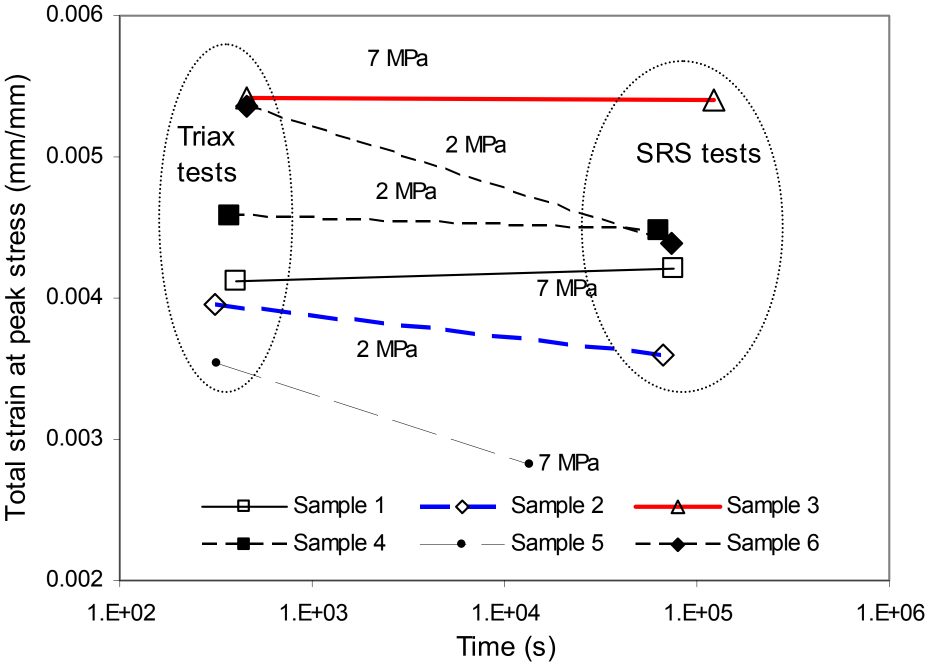

Figure 7-4. *Time to failure and total axial strain at peak stress of the Äspö diorite.*

Also, the total axial strain at the peak stress tends to decrease when the loading rate is decreased. This holds for all tested sample pairs, except Sample 1 (Fig. 7-4). Average peak stress and strains at peak stress are presented in Table 7-1.
Even if the number of tests is too small to allow quantitative conclusions to be drawn, some general trends can be identified. Tests made on specimens sampled close to each other from a core section of limited length show reasonably consistent behaviour: as the peak strength increases with increasing confining pressure, the peak strength is significantly lower when the loading rate is decreased.

Sample 2 (Triax test T3516 and the SRS test S3529) representing a 2 MPa confining pressure and Sample 3 (T3838 and S3851) representing a 7 MPa confining pressure were suggested to be modelled as representative experiments of the tested material for the following reasons. Both samples originate from the same borehole (3.5 m long section of borehole KF0066A) and all specimens show high strength, high Young's modulus and low density compared with the low strength Sample 1 and Sample 5. Samples 2 and 3 also show consistent behaviour in terms of increased strength with increased confining pressure and low strength with low loading rate. Sample 4 could have been an alternative for Sample 2. The SRS test for Sample 2 shows, however, slightly more stable behaviour and better quality laboratory data than the respective SRS test for Sample 4. Sample 6 represents alone borehole KF0069A and shows higher decrease in axial strain at peak strength for the SRS test compared with Samples 1 to 4 (Fig. 7-4).

7.2.2 Triaxial model (TM3516) with confining stress = 2 MPa

The triaxial test T3516 and the SRS test S3529 (from Sample 2 in Table 5-1) were chosen to be modelled to investigate the capacity of FRACOD to simulate delayed failure as observed in the laboratory. In Fig. 7-5b, the stress-strain behaviour of the triaxial compressive strength test T3516 is presented. The axial loading rate was about 0.9 MPa/s. The specimen failed rapidly after reaching the peak strength. The failure pattern suggested shear behaviour.

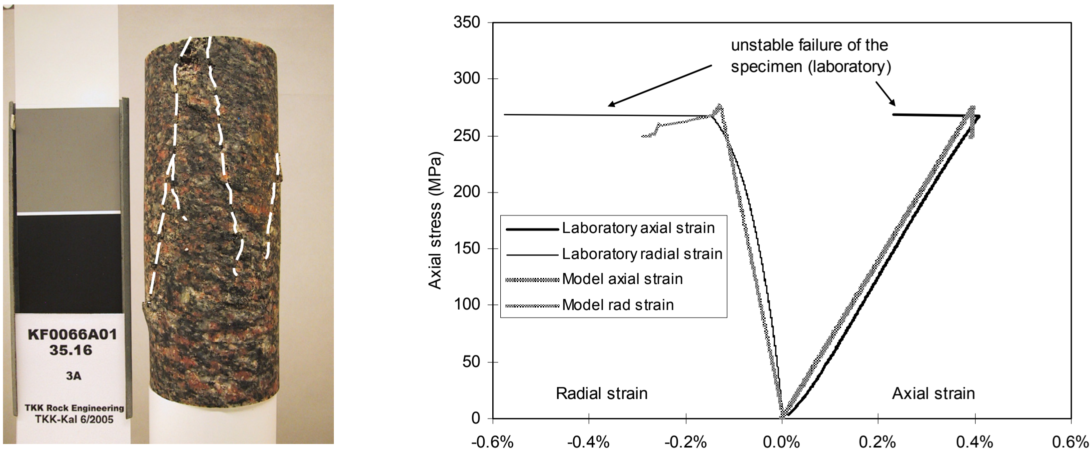

a) *b)*

Figure 7-5. *a) Test specimen T3516 after failure (fractures are highlighted by broken lines); b) stress-strain curve from the experiment and from FRACOD simulation.*

The related FRACOD model was set up as follows: average Äspö diorite material parameters, as presented in Table 5-2 (water-saturated conditions, specimen length 125 mm and width 50 mm). To introduce new cracks into the model already at low levels of applied stress, the new crack formation was set to start using the probability function and $\beta = 0.0$ (Section 4.4.2).

The strain and corresponding time was determined from the laboratory data (Fig. 7-6) registered by extensometers. The strain in the model was then increased in steps as a time-dependent displacement boundary. Additional strain increments were also applied using the average strain rate in order to be able to increase the stress in the model beyond the level of failure detected in the laboratory. In the model, the strain was increased by 1.3×10^{-4} every 10 s corresponding to about a 9 MPa stress increase. Figure 7-6 shows the differential stress (σ_1-σ_3) and strain versus time in the laboratory experiment.

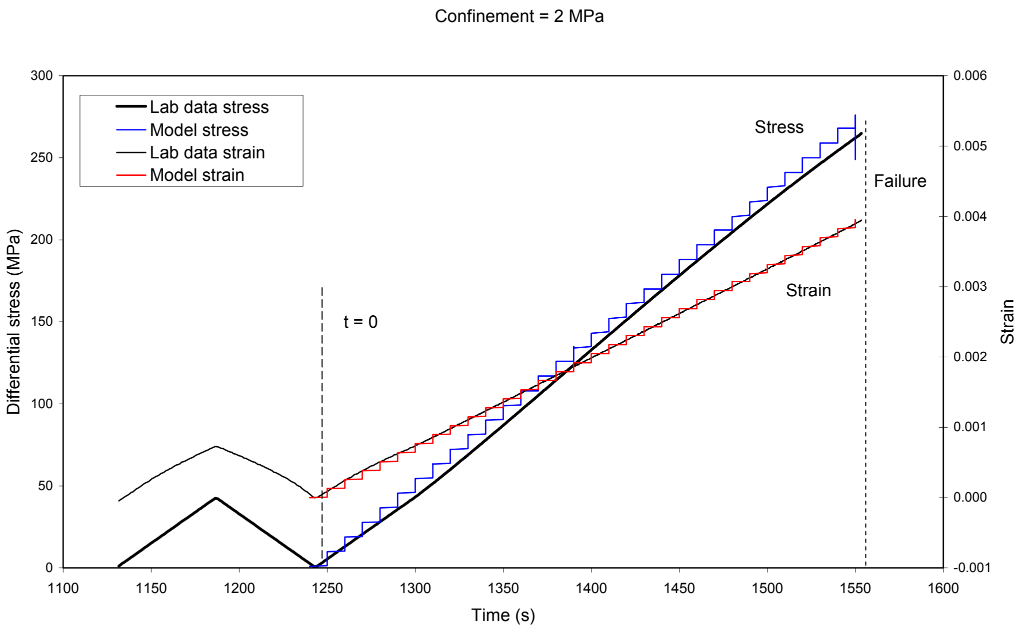

Figure 7-6. *Stress-strain envelope for triaxial test versus time. Laboratory test (T3516) and the FRACOD simulation (TM3516).*

The elastic modulus was set to match the stress-strain curve observed in the laboratory. For the triaxial model TM3516, a Young's modulus E of 70 GPa and a Poissons's ratio ν of 0.24 gave the best fit. The modelled axial stress and strain are added in the laboratory plot (Fig. 7-6) for comparison.

The length of newly formed cracks was calibrated to match the compressive strength and the detected TTF, see Fig. 7-7. The crack length of 1.4 mm gave the best fit (calibration accuracy of 0.05 mm). According to the laboratory test, the compressive strength is 269 MPa and failure occurred after 309 s (Table 7-2). The respective calibrated FRACOD model failed after 306 s at 268 MPa. Figure 7-6 shows the loading process up to failure. The modelled fracture pattern is much like the fracture pattern presented for the SRS test S3529 in Fig. 7-9c.

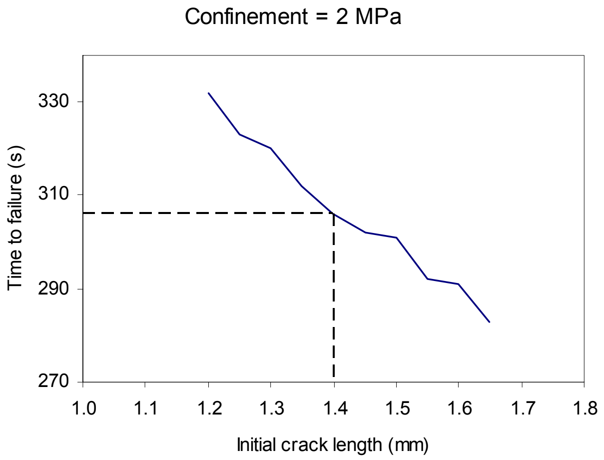

Figure 7-7. *Crack length calibration for the triaxial model to match the laboratory measured TTF.*

7.2.3 SRS model (SM3529) with confining stress = 2 MPa

The SRS model SM3529 was set up by using the fit parameters for the adjacent triaxial model TM3516. All material parameters, including the initial crack length ($2a = 1.4$ mm), were the same as for the triaxial TM3516 model, only the loading sequence was changed to match the actual strain evolution of the adjacent SRS laboratory test. The strain steps were determined from the laboratory data. A few additional representative strain steps (the average size of six strain steps) were included in the model to extend the calculations beyond the level of strain of laboratory-registered failure. The load was increased stepwise altering between a short step and a long step. The short step increase the stress by about 4 MPa within 500 seconds and the slow loading step increased the stress in average about 13 MPa within about 12000 seconds. In the model the slow loading steps were furthermore divided in 10 loading increments.

The elastic modulus was calibrated to match the laboratory curve in the elastic region (i.e. where the SRS begins at about 165 MPa). As in the adjacent triaxial tests, a Young's modulus of 70 GPa and a Poisson's ratio of 0.24 gave the best fit for the SRS model in the elastic regime. Figure 7-8 illustrates the stress-strain response of the S3529 test and the corresponding FRACOD model (SM3529).

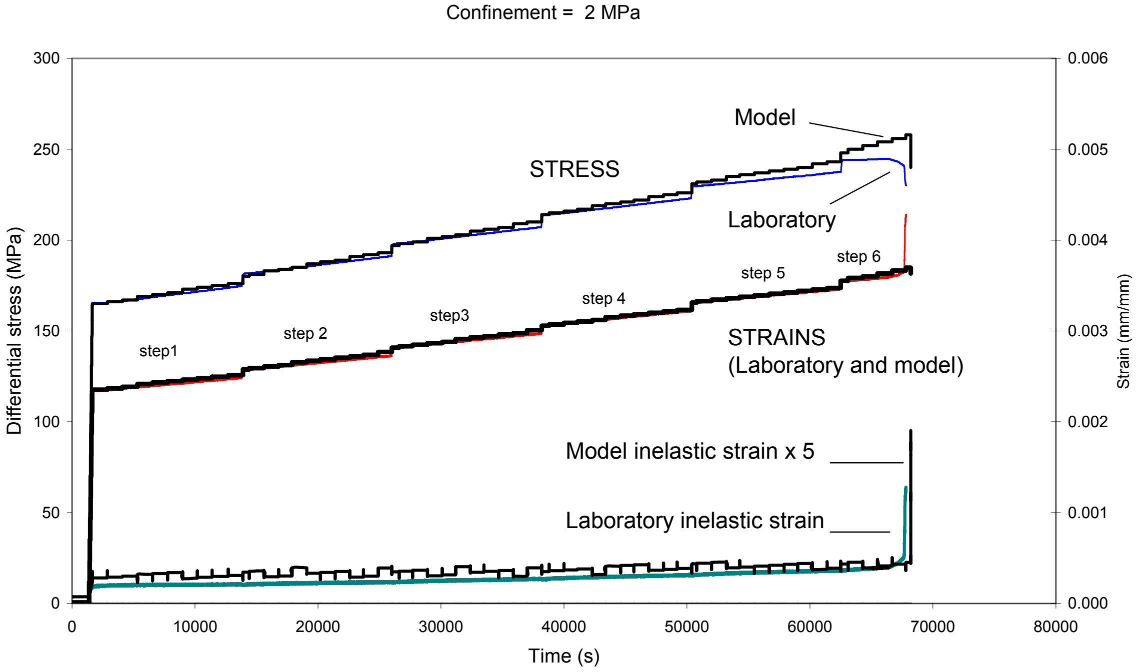

__Figure 7-8.__ Stress and strain as a function of time for SRS test S3529 and the corresponding FRACOD model (SM3529).

The cumulative SCG was calculated during every loading step. In the laboratory, the specimen failed after 66280 s at 246 MPa. The modelled failure occurred at 66840 s, corresponding to a 258 MPa applied stress (Fig. 7-8).

The specimen after failure and the modelled failure pattern are presented in Fig. 7-9. The global failure observed in the laboratory suggests shear behaviour, but also a tendency for axial splitting is indicated (Fig. 7-9a, b). The model shows dominant fracture propagation in Mode II (Fig. 7-9c).

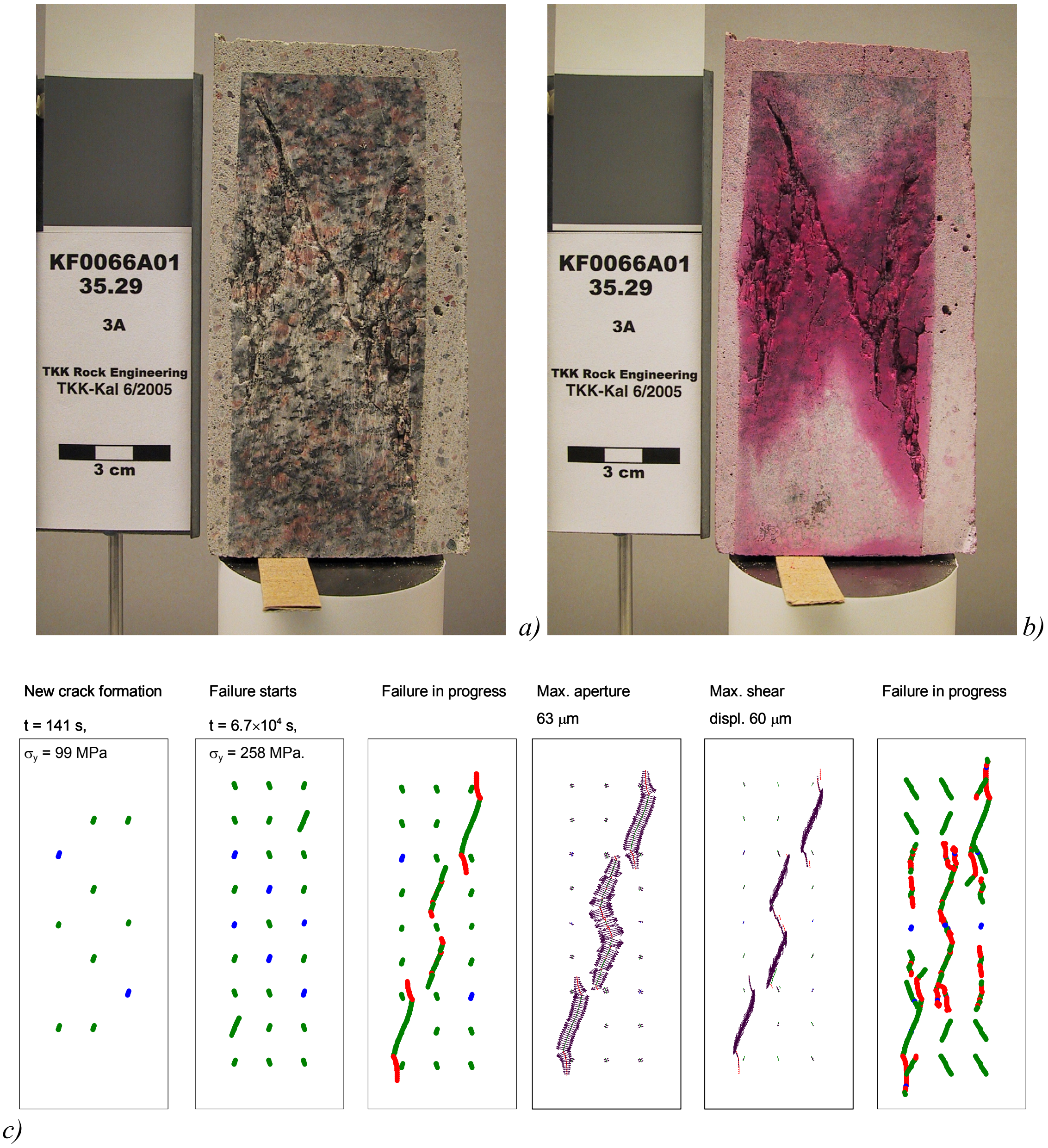

Figure 7-9. *a) SRS specimen S3529 after test; b) ink-impregnated specimen; c) modelled fracture pattern (SM3529).*

7.2.4 Triaxial model (TM3838) with confining stress = 7 MPa

The third sample pair (triaxial T3838 and SRS test S3851, see Table 5-1) with a confining stress of 7 MPa shows consistent behaviour in the laboratory (Figs 7-3 and 7-4). An analogous modelling procedure as in the previous sections was applied. A Young's modulus E of 65 GPa, Poisson's ratio ν of 0.32 and a crack length of 2*a* = 1 mm gave the best fit for stress-strain behaviour and for the TTF calculation (Figs. 7-10c and 7-11).

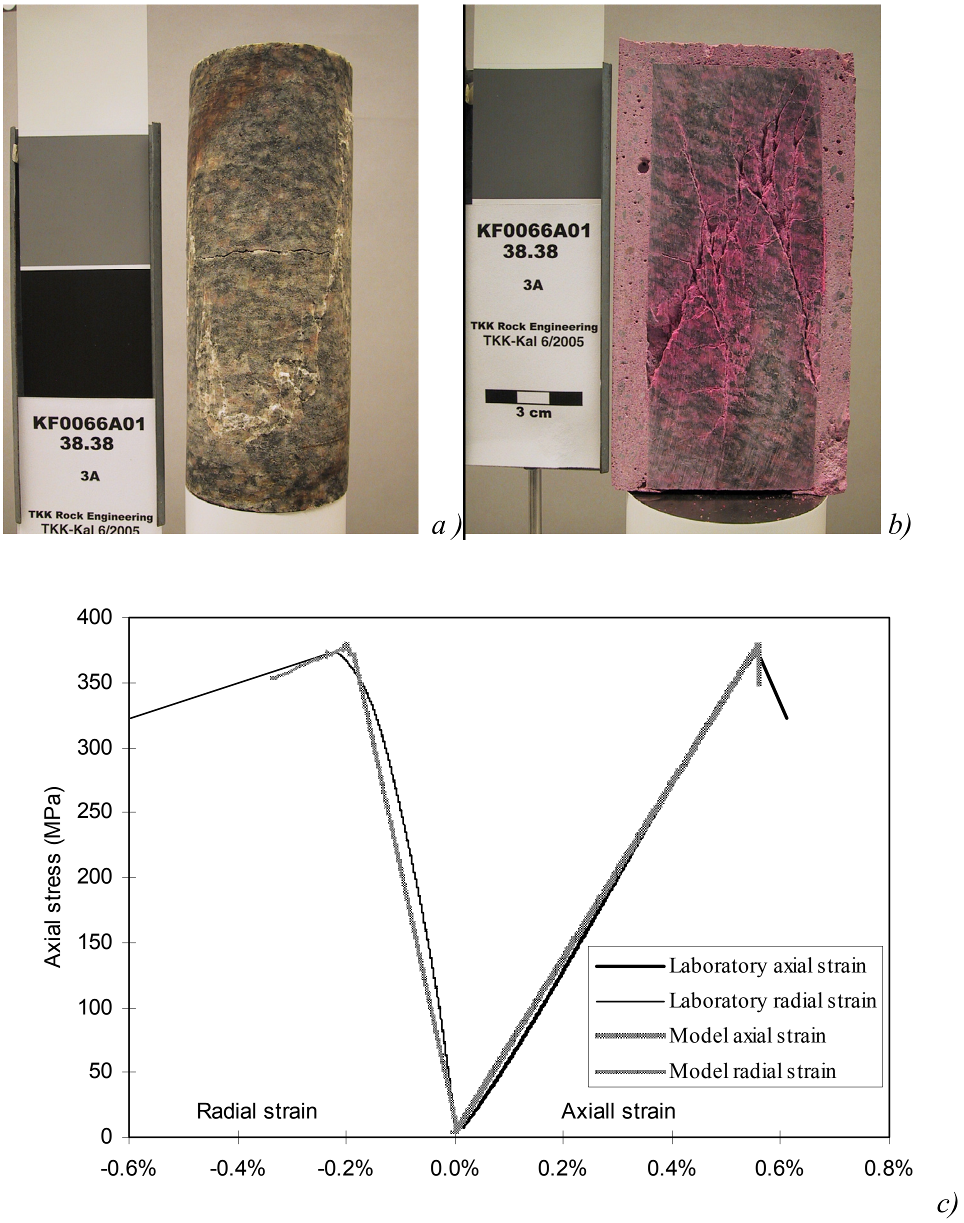

Figure 7-10. *a) Triaxial test specimen T3838 after failure; b) saw- cut and ink treatment; c) stress and strain curves for specimen T3838 and from FRACOD simulation.*

The failure mode of the laboratory test is unclear, indicating to some extent shear behaviour. The modelled failure pattern is comparable to the failure presented for the SRS test S3851 in Fig. 7-13c.

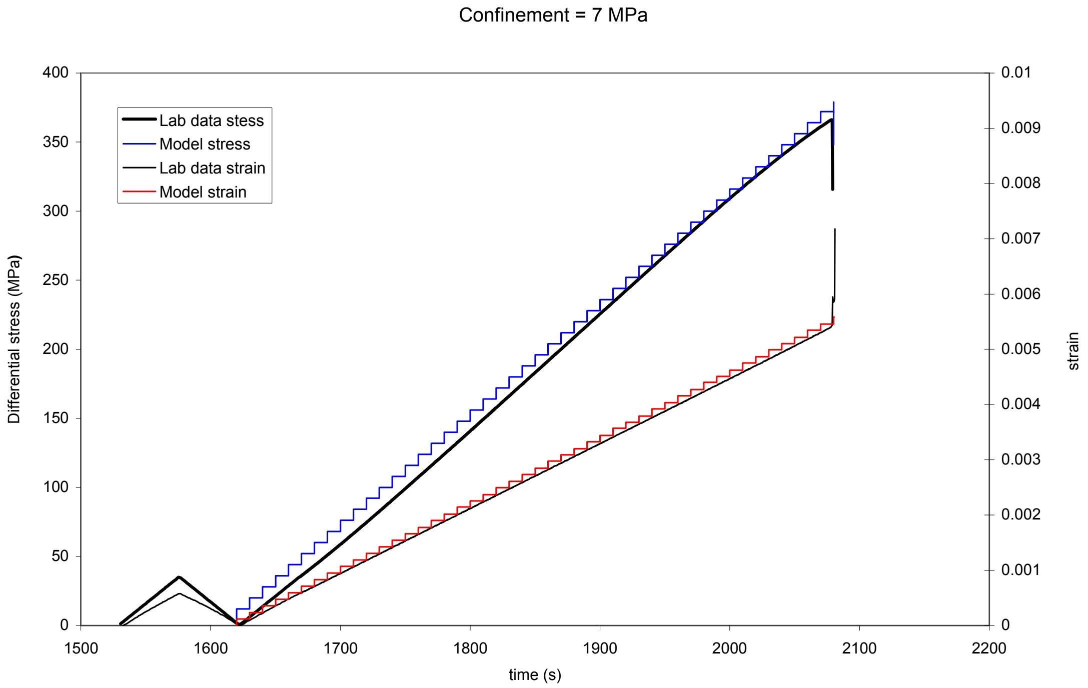

Figure 7-11. *Stress and strain versus time for the triaxial test. Laboratory behaviour (T3838) and FRACOD model (TM3838).*

7.2.5 SRS model (SM3851) with confining stress = 7 MPa

The SRS model for test number S3851 was set up as presented for the previous example by recalculating the calibrated triaxial model using the strain step loading history obtained from the laboratory data. The crack length was kept the same (*2a* = 1 mm) as in the triaxial model and the stress was adapted with the strain in the elastic region by using a Young's modulus *E* of 63.4 GPa and a Poisson's ratio ν of 0.31. The laboratory test failed after 1.21899 × 10^5 s at 342 MPa. The FRACOD model suggests failure at about the same time (1.21850 × 10^5 s), showing a somewhat higher level of stress, about 352 MPa (Fig. 7-12). Table 7-2 summarises the laboratory and modelling results.

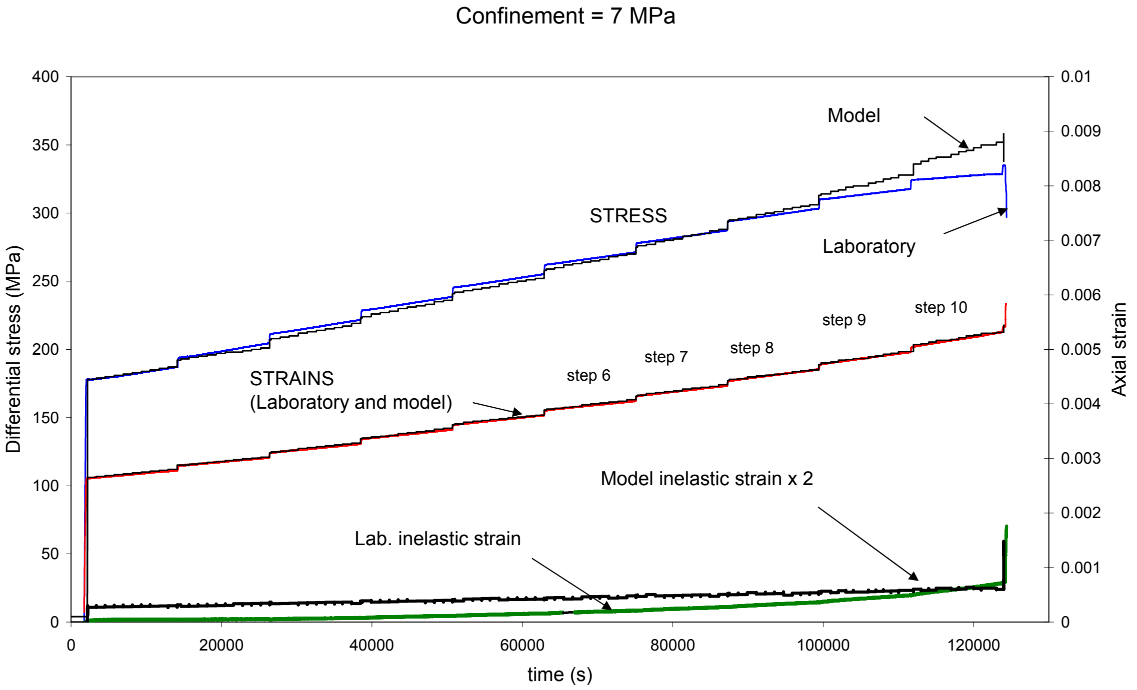
Confinement = 7 MPa

__Figure 7-12.__ Stress-strain envelope versus time for SRS test S3851 and FRACOD model (SM3851).

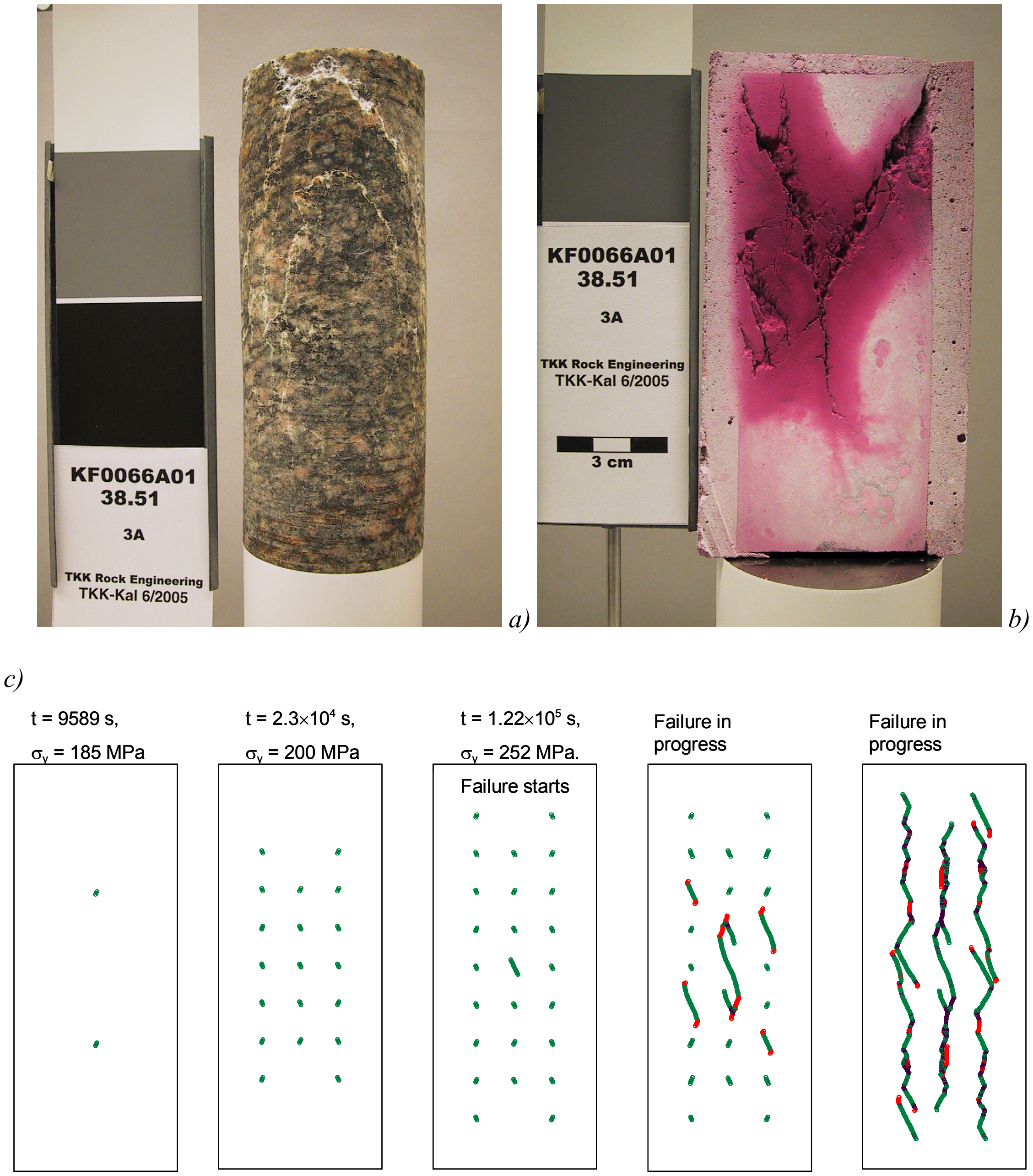

Figure 7-13. *a) SRS specimen S3851 after failure; b) after saw-cut and ink treatment; c) modelled fracture pattern (SM3851).*

7.2.6 Extrapolation of failure

The SCG parameters presented in Table 5-2 have been used in all time-dependent models presented in this chapter. To investigate numerically the effect of SCG in standard triaxial tests, the triaxial models were recalculated using a high value (99) of n and low B values (1×10^{-14}). These values were found to prevent all SCG when model discretisation as presented for the previous models was used. Table 7-2 shows that, comparing the 'no time-dependent model' with the 'time-dependent triaxial model', the calculations suggest only slight time effects for the 'time-dependent triaxial model'. For the time-dependent SRS models, however, the SCG significantly affects the loading time, the peak stress and the strain at failure.

Table 7-2. Laboratory results and models.

Test / model	Time to failure	Stress at failure	Strain at failure
Triax test (2 MPa)	**s**	**MPa**	**mm/mm**
Laboratory test T3516	3.09E+02	269	3.95E-03
Model: time-dependent TM3516	3.06E+02	268	3.84E-03
Model: no time-effects, TM3516	3.11E+02	268	3.84E-03
Strain Rate Stepping test (2 MPa)	**s**	**MPa**	**mm/mm**
Laboratory test S3529	6.63E+04	246	3.68E-03
Model: time-dependent SM3529	6.68E+04	258	3.70E-03
Model: no time-effects, SM3529	8.23E+04	281	4.02E-03
Tiax test (7 MPa)	**s**	**MPa**	**mm/mm**
Laboratory test T3838	4.55E+02	373	5.42E-03
Model: time-dependent TM3838	4.53E+02	372	5.46E-03
Model: no time-effects, TM3838	4.61E+02	372	5.46E-03
Strain Rate Stepping test (7MPa)	**s**	**MPa**	**mm/mm**
Laboratory test S3851	1.22E+05	342	5.41E-03
Model: time-dependent SM3851	1.22E+05	352	5.31E-03
Model: no time-effects, SM3851	1.38E+05	380	5.74E-03

(*)In the diagrams (e.g. Fig. 7-7) the time is not set to zero when the loading is started. In the table the time to failure is given as a net time calculated from the start of the actual test.

It is particularly interesting to evaluate the strength of loaded rock over time periods that are not possible to test in the laboratory. The TTF was predicted by recalculating the SRS test models using several levels of constant strain. The load was increased using similar loading sequences as presented for the SRS models. The constant levels of strain correspond to the strain steps presented for models SM3529 and SM3851 (Figs 7-8 and 7-12). For example, the SRS model SM3529 presented in the previous section failed after 6.68×10^{4} s (18.5 h) when the strain was successively increased to 3.70×10^{-3} mm/mm corresponding to a stress of 258 MPa. When the model was recalculated by increasing the load to a constant level of strain (3.07×10^{-3} mm/mm), corresponding to the start of strain Step 4, and axial stress of 215 MPa, the model failed after 6.45×10^{10} s (2045 years), (Fig. 7-14 and Table 7-3). The model did not show failure within 3.15×10^{13} s (1 Ma) when loaded by a constant strain of 2.83×10^{-3}, corresponding to about 200 MPa axial stress (Step 2).

Triangles in Fig. 7-14 signify the events at which SCG or unstable fracture propagation occurs, i.e. when the crack length is increased by one element. Because unstable failure never occurred at strains corresponding to Step 2 and Step 3 for SM3529, there is no significant stress relaxation at the end of loading. The predicted long-term strength at different levels of strain is presented in Table 7-3.

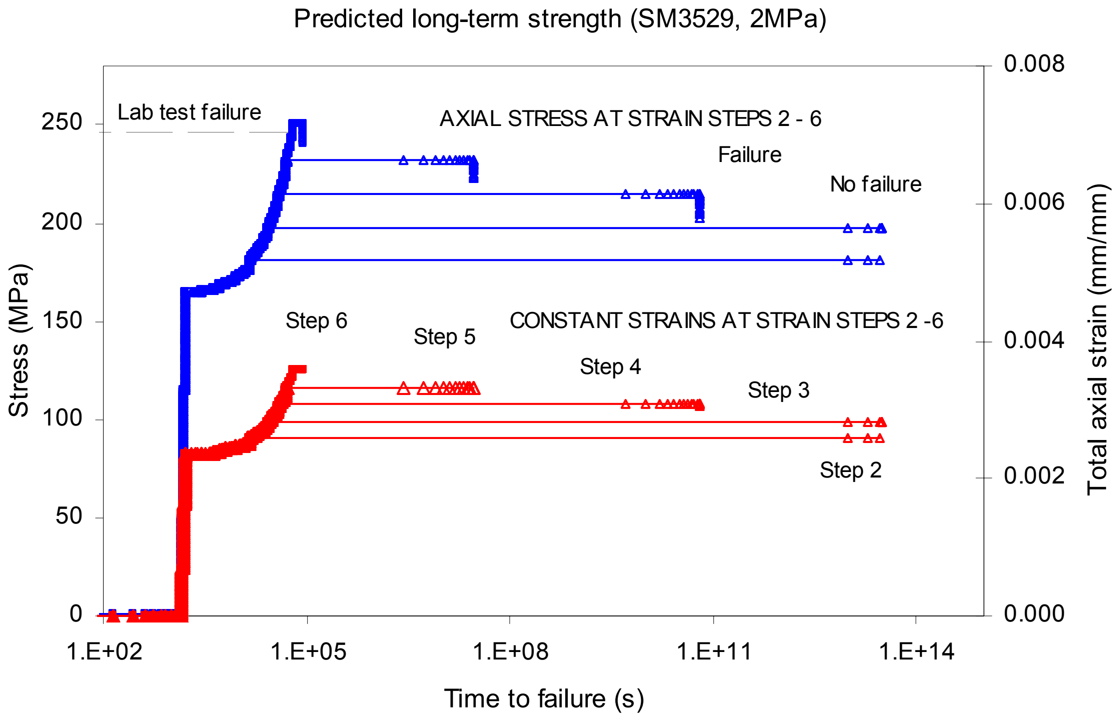

Figure 7-14. *FRACOD model SM3529 with constant long-term strains. The strain increase was stopped at strain levels corresponding to Steps 2, 3, 4, 5 and 6 (see Fig. 7-8). The triangles signify events when a crack element is added into the model. Unstable fracture propagation is indicated by rapid stress relaxation (Steps 4, 5 and 6).*

Similarly the model SM3851 representing the effect of a 7 MPa confining pressure was modified to calculate the long-term strengths at constant strains, corresponding to the strain at the start of strain Steps 7 to 10 (Fig. 7-12). Because the maximum time calculations were set to 3.15×10^{13} s, the specimen loaded to Step 7 or less never failed.

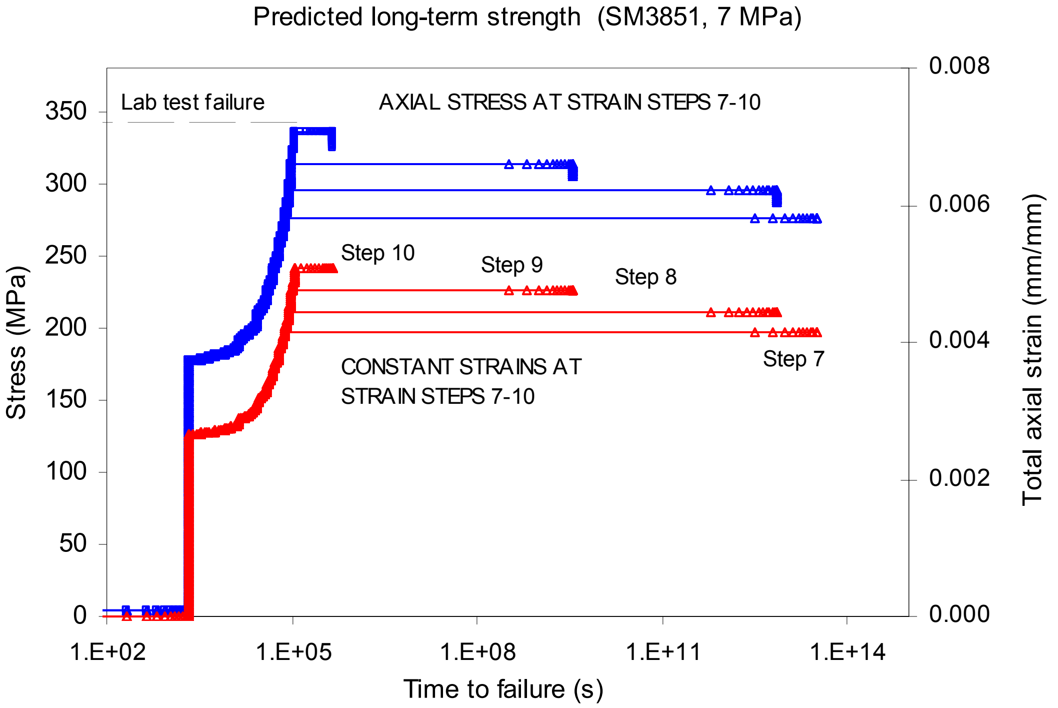

Figure 7-15. *FRACOD model SM3851. The model is calculated with constant long-term strains corresponding to strains at the start of strain Step 7 to Step 10 in Fig. 7-12.*

Table 7-3. Long-term strength according to FRACOD models.

Test	Time to failure	Applied stress	Applied strain
	s	**MPa**	**mm/mm**
Lab S3529 (2 MPa)	**6.63E+04**	**246**	**3.68E-03**
Model SM3529	6.68E+04	258	3.70E-03
Step 6	9.12E+04	250	3.58E-03
Step 5	2.88E+07	232	3.33E-03
Step 4	6.45E+10	215	3.07E-03
Step 3	> 3.15E+13	198	2.83E-03
Lab S3851 (7 MPa)	**1.22E+05**	**342**	**5.41E-03**
Model SM3851	1.22E+05	352	5.31E-03
Step 10	4.67E+05	336	5.09E-03
Step 9	3.66E+09	314	4.75E-03
Step 8	7.28E+12	295	4.45E-03
Step 7	> 3.15E+13	276	4.16E-03

For the SM3529 and SM3851 models, different initial crack lengths were used, as described in Sections 7.2.2 and 7.2.4. To evaluate exclusively the effect of the confinement on the long-term strength, additional numerical simulations were performed by using a 7 MPa confining stress instead of 2 MPa for SM3529 and the triaxial model TM3516. Results from Table 7-3 and the modified SM3529 and TM3516 are presented in Fig. 7-16. In this example, the increase in confining pressure increases the required stress/strain level for failure but does not significantly affect the slope of the TTF curve.

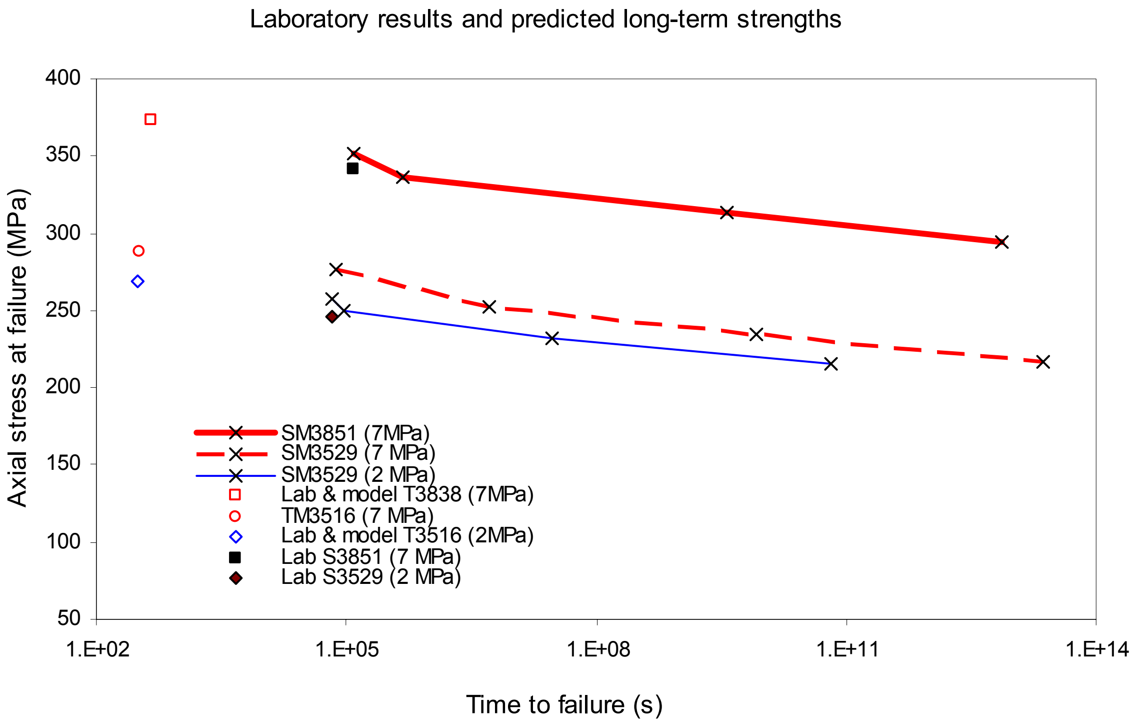

Figure 7-16. *Time to failure predictions and results from the laboratory (see Table 7-3).*

8 DISCUSSIONS ABOUT BRITTLE FAILURE AND FRACOD MODELLING

8.1 Observed and modelled failure

8.1.1 Non-time-dependent models

Under pure tensile loading micro-cracks start to nucleate from the weakest elements or, i.e., from the most critical local stress concentration in the polycrystalline matrix. Crack initiation, propagation and coalescence escalate rapidly in the direction perpendicular to the major tensile stress when the applied load reaches the critical stress level. This process was clearly identified from the tensile test model, as presented in Section 6.4.

The crack growth and failure under compression is more complex process compared with the tensile failure and it is initially a stable process. The cracks are evenly distributed throughout the specimen prior to the stable and unstable crack interaction and the coalescence that leads to the formation of a localised failure plane and sudden specimen rupture. Similarly for FRACOD compressive strength test models, the new cracks are formed successively under increasing load until the specimen is evenly populated with cracks. With increasing load the stable wing-crack propagation occurs prior to the unstable fracture propagation in the shear stress direction, as suggested by, e.g., Wawersik and Fairhurst (1969) and Main et al. (1993). Only the central sections close to the top and bottom boundaries remain ‘intact’. According to laboratory observations (Wawersik and Fairhurst 1969), crack density decreases continuously in the axial direction, from the centre toward the loaded ends of the specimens due to frictional restraints at the specimen-loading platen interfaces. For the FRACOD specimen models, the shear displacement in the lateral direction at the top and bottom boundaries was prevented. This was found to effectively reduce the crack initiation and fracture propagation at the loaded ends.

Laboratory studies show that only minor permanent deformation occurs in rock prior to rupture in short-term UCS tests, especially for Class II types of brittle rocks. Growth of a macroscopic fracture generally takes place rapidly when the applied stress becomes equal to the compressive strength and faulting takes place as the predominant failure mode (Wawersik and Fairhurst 1969). This behaviour has been reproduced successfully by the FRACOD models. The models suggest that some stable ‘wing-crack propagation’ occurs prior to the formation of the shear fault, when parameters determined for the Äspö diorite are used.

Wawersik and Fairhurst (1969) further argue that because the stress field remains sensibly uniform throughout the sample in the absence of axial fracturing, the faulting is equally likely to be initiated at the boundary or in the interior of the specimens and that the fault angles will be the same in both cases. The models suggest that failure may start in the middle part of the model specimen or close to the model boundaries (e.g. Figs 7-9c and 7-13c). The angle of the propagating crack (about $\alpha = 20°$ from the major load in UCS models) depends on the mode of failure and confining pressure, but not significantly on the location of the crack in the specimen.

It has been experimentally observed (e.g. Bobet and Einstein 1998a, Backers 2005) that wing-crack propagation is suppressed above a certain level of confining pressure. This observation is reproduced by calculations; as the confinement increases the wing-crack growth and adjacent crack dilation is suppressed (e.g. Figs 6-1, 6-6 and 6.39). For some models, fractures were found to propagate in a stable manner also in the shear stress direction prior to an unstable rupture.

This was more frequent for models with high confining pressure (>30 MPa) and it might be a consequence of the interaction of closely located cracks and crack coalescence. The stable Mode II crack propagation may start several tens of megapascals below the peak strength for models with high confining pressure.

The natural heterogeneity of rock can produce shear stresses at the front of a propagating fracture, resulting in tilted and twisted fracture paths (Pollard and Aydin 1988). The complexity of rock fracture surfaces also indicates that the local stress directions can vary considerably. In the FRACOD models, the newly formed cracks present weakness planes (for example weak contacts of mineral grain boundaries) resulting in a rough zigzag path as the failure extends. A rough fracture path is also produced due to changes in the failure mode, as presented in Fig. 6-2.

The modelled shear movement at the fracture surfaces is small, in order of tens of micrometers. This is consistent with the microstructural observation in the laboratory (Backers 2005), where only small shear displacements could be found related to Mode II fracture propagation. More significant dilation of the major shear fractures was found to occur in the late post-peak stage of failure, especially for those models subjected to low confinement. Modelling the block separation in the final phase of post-failure is limited with FRACOD software. When a piece of rock is totally detached from the host, large displacements are introduced into the model and numerical instability may occur. This kind of instability was discovered in models with no confinement, such as UCS models.

For the FRACOD models with several cracks, the loading history affects the level of strain (or stress) required for fracture propagation and the subsequent failure process. For an initially intact rock model, the onset of new crack formation is not dependent on the loading path. However, further development of the newly formed cracks depends on the size of the applied load increments. Several small loading steps to reach a certain level of strain yield less new crack formation compared with a few large loading steps to reach the same level of strain. This is because small load increments reduce the ‘shock’ stress associated with a sudden stress increase which may lead to enhanced new crack formation. Fracture stiffness, slipping and opening of new cracks alter the stress distribution and hence influence the development of further new crack formation. As a consequence, the size of the loading steps also affects the critical strain for fracture initiation and propagation and the subsequent post-peak behaviour and failure pattern. Small loading steps seem to favour large separately propagating fractures. By using small loading increments the critical stress intensity is achieved only in the most critical crack tips. Generally, the stress intensity factor for a long crack is higher compared with a similarly loaded short crack. In addition, a propagating crack may alter the stress field in such a way that it shadows another crack for further propagation.

An important aspect of the presented model is its ability to model realistically the brittle axial and lateral responses during the failure process. Class II behaviour of the post-peak failure was successfully modelled and the phenomenon is explained by the Griffith locus. Initial FRACOD modelling indicates that Class I and Class II post-peak failure behaviour is controlled by the fracture and intact rock properties, the rock volume considered and the boundary conditions (Rinne and Shen 2005). The effect of material parameters and sample size on the shape of the Griffith locus (and Class I and Class II post-peak behaviour) is, however, beyond the scope of this thesis, and will be studied further in the future.

8.1.2 The macro-scale failure and fracture pattern

All laboratory specimens for intact rock tests (Section 5.2) were photographed before and after testing. Visual inspection was performed to observe the failure mode of the tested specimens on a macro-scale. The fracture pattern from the Brazilian tests (six specimens) regularly suggests axial splitting (Fig. 5-7).

For the compressive strength tests, the failure mode and the fracture pattern are more indistinct. In the UCS tests (six tests), chip formation was observed and axial splitting occurred at least close to the unconfined surfaces. However, the dominant macro-fracture causing the final specimen rupture remains unclear. The UCS tests were performed using radial strain controlled loading (Section 5.2.2) to detect the post-peak stress-strain behaviour. This results in a controlled rupture and the specimen is usually in one section after the (internal) structural breakdown. The Triax and SRS tests were performed using monotonically stepwise increasing axial strain over the peak stress. The post-peak failure was not controlled and rapid rupture of the specimens occurred. Hence the fracture patterns in both Triax and SRS tests are most likely affected by the excess energy released in the unstable post-peak failure phase compared with the radial strain controlled UCS test.

For the confined Triax (six tests) and SRS (six tests) tests, the axial fracturing is considerably reduced and the individual and inclined shear planes ($\alpha = 20°\text{-}35°$ from the major load) are common. The fracture pattern of the low loading rate SRS tests is somewhat more indistinct compared with fracture patterns of the standard loading rate triaxial tests. The somewhat more indistinct fracture pattern of the SRS test specimens compared with Triax tests might be due to subcritically growing cracks and more evenly distributed fracturing in the SRS tests. The applied resolution of the FRACOD models was, however, not sufficient to capture the above-mentioned phenomenon.

To improve the visibility of the fracture pattern, five specimens were encased in concrete grouting, cut longitudinally and photographed. The cut surfaces were impregnated with red ink to reveal the cracks (Antikainen 2007). Examples of ink-treated specimens are presented in Figs 7-9, 7-10 and 7-13. This treatment gives a better representation of the fracture traces compared with an untreated specimen. However, a more rigorous analysis, including microscopy studies of the tested specimens, is required to draw more robust conclusions on the failure mechanisms. Also, new techniques must be developed to improve tracking of the failure process. X-ray tomography (Timonen et al. in Rasilainen 2006) and characterisation of the failure in real time from thin slices of rock (Backers 2005) are promising new techniques.

It seems to be a difficult task to compare the modelled fracture pattern with the fracture pattern of tested specimens. The fracture pattern in the tested specimen varies considerably and only a few conclusions can be drawn from visual inspection. In addition to extend the laboratory data base, a statistical approach in the modelling procedure with varying material parameters and several model realisations might help to make a more robust evaluation of the real and modelled fracture pattern. However, both visual evaluation of the failed specimens and the model results suggest that the state between axial failure and an inclined fault type of failure is delicate, especially for low confining pressure tests.

In particular, samples with a tendency towards axial failure show an asymmetric fracture pattern. The symmetrical shape of the modelled fracture pattern, as presented for most of the UCS, Triax and SRS test models, is a consequence of a symmetric model set-up. Asymmetric models give stress-strain behaviour consistent with that of a symmetrical model and more realistic asymmetric crack pattern. Asymmetric models are presented in Figs. 6-1 to 6-6.

Numerical studies and laboratory analysis of fracture interaction and fracture traces for simple loading configurations can be found in the literature. Shen et al. (1995) studied the interaction of fractures by analysing the failure of the rock bridge between two inclined cracks under compression in a laboratory experiment with gypsum samples and compared the results with DDM fracture models. Numerical modelling of fracture coalescence in a rock-like material is also reported by Bobet and Einstein (1998b) and by Vásárhelyi and Bobet (2000). The results presented in these studies are in good agreement with the results presented in this thesis.

8.1.3 Time-dependent models

The specimen-specific triaxial strength test models were set up and calibrated with an initial crack length to match the failure observed in the laboratory. These short-term strength test models were modified to follow the loading history applied in SRS tests in the laboratory. The predicted TTF of the modelled SRS tests agrees reasonably well with the SRS test results from the laboratory (Table 7-2) considering the heterogeneity of tested material and the resolution of the modelled loading steps, as explained in Sections 7.2.2 and 7.2.3.

Because the axial strain measured in the laboratory was used as a boundary value, the strain in all models follows the laboratory value within the applied strain step resolution. The slight difference in strain at failure between the triaxial laboratory value and the numerical model could be adjusted by defining more accurately the initial crack length and the strain increments. Also the stress curve for the triaxial models could be fine-tuned by more accurately calibrating the elastic parameters.

The modelled stress-strain behaviour of the SRS tests agrees well with the laboratory results in the elastic region, but overestimates the stresses, especially close to the failure (Figs 7-8 and 7-12). In other words, the model underestimates the stress relaxation and the laboratory results show an inelastic deformation several times higher compared with the numerical model. To be able to simulate more realistically the inelastic strain and stress relaxation caused by SCG the number of cracks and the number of elements along the cracks should be increased considerably. In the presented models, the newly formed cracks are defined by two elements.

When the accumulated length of SCG meets the predefined length of a crack element, a new tip element is added. When a crack is discretised with only a few elements, a sudden increase in the crack length significantly alters the stress distribution around the crack. This usually results in unstable crack propagation for those models loaded closed to the peak already after the first subcritically grown crack element has been added into the model. A better crack resolution, however, requires more calculation capacity than a standard desktop computer can offer today. Developments in computing techniques will solve this bottleneck and make more realistic calculations possible with a standard desktop computer in the future. The tensile test model (Fig. 7-1) with only one pre-existing crack represents a better model discretisation and description of the stress relaxation compared with the Triax and SRS test models. The SRS test models modified to predict the failure at low levels of stress, however, allows SCG elements to be introduced at the crack tip without instant failure. In Fig. 7-14 and Fig. 7-15 the triangles signify events when a SCG element is added into the model during the long-term constant load. However, now significant stress relaxation is detected for the modified SRS test models, until the unstable failure takes place.

Ambiguity may also be present in the laboratory determination of inelastic strain. The inelastic strain, as presented in Table 5-1 and in the SRS laboratory test curves (Fig. 7-8 and Fig. 7-12), is zeroed by subtracting the apparent strain from the crack closure at the stress level where the elastic behaviour starts, usually below 100 MPa. It is not always unambiguous to define accurately the elastic modulus from a stress-strain curve. The determined magnitude of inelastic strain is sensitive to the selected value of the elastic modulus, which is assumed to be constant. The specimen might exhibit pre-damage that might contribute to the inelastic strain even at high levels of stress.

To evaluate numerically the effect of SCG on standard compressive strength tests, the Triax and SRS models were recalculated using a high SCG growth index to prevent the time-dependent slow crack growth that might occur during the loading. From Table 7-2, we can note that the models suggest only a minor time effect on standard triaxial tests, while for the SRS models the time has a significant effect in terms of loading time, capacity to sustain load and on the strain at failure.

8.1.4 Predicted long-term strength

The predicted long-term strength does not seem to decrease very severely over long time periods. When the applied stress was less than 80% of the predicted short-term peak strength, models with a confinement of 2 MPa and 7 MPa suggested stable behaviour over 1 million years. This was expected considering Fig. 5-15. There the crack velocity decreases fast as the applied stress is decreased due to the high SCG index n, especially for Mode II loading. The effect of confinement increases the required stress/strain level at failure but does not affect the slope of the TTF curve for the modelled loading conditions (Fig. 7-16).

The model in this study yields less strength reduction in the long-term strength as suggested by the model presented by Lajtai and Bielus (1986). They evaluated the time-dependent strength from creep tests. The rate of cracking was defined by finding a relationship between the rate of crack growth, expressed as the rate of crack volume strain, and the uniaxial compressive stress. The crack volume strain rate versus the stress function curve was integrated to obtain a lifetime estimate for the Lac du Bonnet granite. After 1000 years of loading at room temperature and 100% humidity, the calculated strength of this granite could reduce by 55-60%.

8.1.5 Uncertainties related to long-term strength predictions

Extrapolation of tests to low applied stresses for long periods of time involves many uncertainties. These uncertainties can be related to the form of the fundamental equations (Section 2.9), to the accuracy of numerical approximation (Section 8.2), to material parameters (Section 8.3) and to the uncertainties related to boundary conditions.

The time-dependent model presented in this thesis utilises velocities of subcritically growing cracks, as detected under varying loading conditions. It is assumed that the crack velocity is always the same under similar thermo-hydro-mechanical and chemical boundary conditions. The SCG parameters used in the modelling were defined for a constant temperature, pressure and chemical environment. Even small changes in these conditions influence the crack velocity, resulting in a major change in the predicted long-term strength. Extending the use of laboratory-determined parameters to real geophysical environments further increases the uncertainty of the predictions. For example, in the laboratory tests the crack tip was supplied with a sufficient amount of reactants from the salty water to keep the chemical reaction in progress at the crack tip. In the rock mass, the crack can be isolated in a hydraulic sense and no transport of the reactants and reaction products occurs. Also, micro-mechanisms competing with stress corrosion may occur in the earth's crust. Precipitation and crack healing are also likely processes not considered in the presented model. The longer the time spans considered, the more reservations are involved in the prediction. This important issue is more thoroughly discussed in the literature (e.g. Atkinson 1984; Lockner 1993; Kemeny 2002).

It is not clear if there exists a stress corrosion limit for rocks and, if there is such limit, at which level of applied stress the crack stops to grow subcritically. The modelling presented in this thesis assumes that no stress corrosion limit exists. The crack velocities (v_1 and v_2) versus the stress intensity factors (K_I and K_{II}) as observed in the laboratory under saturated conditions (Backers 2006a) are illustrated in Fig. 8-1. The stress intensity factor is normalised with the fracture toughness. The lowest crack velocity in the laboratory test (Section 5.3.2) is estimated for the slowest experiment performed at about $K_I / K_{IC} = 0.73$, corresponding to a crack velocity of about $v_1 = 4.29\times10^{-10}$ m/s. If a constant velocity is assumed, this corresponds to about 14 mm crack growth per year. Similarly for Mode II loading, the intercept along the K-axis as derived from the slowest experiment at $K_I / K_{IIC} = 0.87$ corresponds to a crack velocity of about $v_2 = 1.25\times10^{-9}$ m/s or 40 mm/year.

The much lower n_1 (Mode I loading) compared with n_2 (Mode II loading) suggests that SCG is more pronounced for Mode I failure in Mixed-mode I-II loading conditions at low levels of applied load. It must be noted, however, that for Mode I wing-crack propagation (under compressive loading conditions) the stress intensity decreases as the wing crack extends towards the major principal load. Hence the SCG of a wing crack is a self-stabilising process. SCG in Mode II (shear failure direction) becomes more important close to the critical stress for unstable fracture propagation. On the other hand, compressive shear cracks are closed and the hydraulic conductivity is reduced, therefore the transport of the reactants and the reaction products at the crack tip is reduced.

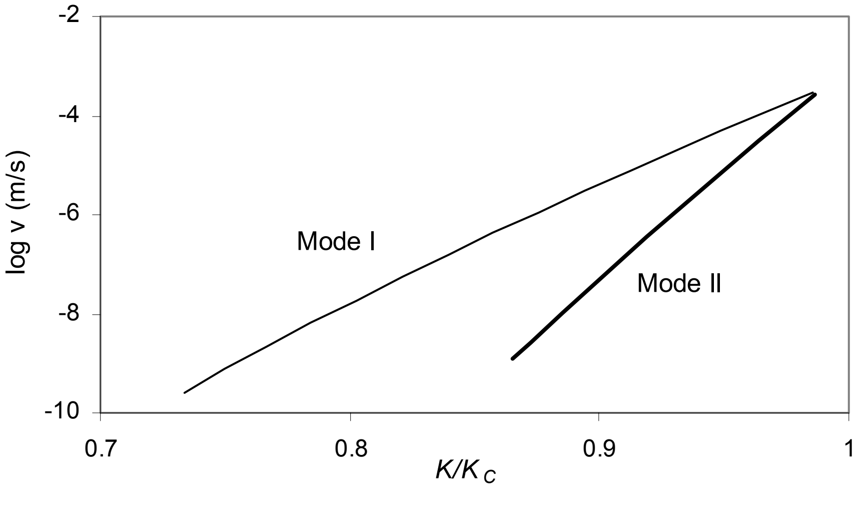

Figure 8-1. *Normalised stress intensity factor (K/K_C) versus crack velocity log(v) plot for Mode I and Mode II subcritical crack growth. Data from Backers et al. 2006a.*

8.2 Model accuracy

8.2.1 Accuracy of the numerical approximation

A model is a simplified indication of reality and it has limitations to express the real rock behaviour, no matter what approach or numerical method is used. A model always involves assumptions, generalisations, inaccuracies and uncertainties. A comprehensive review of different numerical techniques, their advantages and disadvantages are discussed in Jing (2003). Common to all numerical approximations is that the more elements that are used to define the model, the more accurate are the stress and strain results obtained. Computed and exact stresses in a compressed circular disk and around a circular hole using the fictitious stress method and the DDM are reported by Crouch and Starfield (1983). The numerical solutions were found by using two element approximations ($N = 25$ and $N = 50$) to one-quarter of the circular boundary. The numerical results are in good agreement with the exact solution. It was indicated that the DDM achieves about the same level of accuracy as the fictitious method. For the fictitious stress method, it is noted that the numerical solution is unreliable at points within a circle of radius equal to one element length centred at the midpoint of a boundary element (except at the midpoint itself).

Increasing the number of elements increases the calculation time. Hence, the applied element size is a compromise between accuracy and practical issues such as calculation capacity and calculation time. The number of elements must be sufficient, especially when studying in detail the behaviour of a fracture close to a boundary or another fracture. The current version of FRACOD software is set to be capable of handling up to 400 elements in the model. This limit does not, however, in practice impact upon the calculations, because the computing capacity is in most cases the limiting factor. The initial model size depends on the geometry of the finite boundaries, the number of cracks and model discretisation. As the fractures extend, the number of elements increases and the calculations become more time consuming. A model with less than 100-150 elements at the start is a practical upper limit for calculations using a standard desktop computer. The calculation time for the most complex models (UCS and SRS test models) in this thesis using a standard PC is up to 24 h, while calculations for the simple loading configurations (far-field models with one or two cracks) takes only a few seconds or minutes.

8.2.2 Element size

The accuracy of the numerical approximation is evaluated using a simple tensile crack model as presented in Fig. 8-2a. An isolated crack ($2a$ = 1 mm) with a varying number of elements is subjected to a tensile stress perpendicular to the crack. The far-field stress is increased until the critical magnitude of the stress for fracture initiation is reached. The analytical solution (Eq. 3-14) yields an 81-MPa stress at the critical stress state (K_{IC} = 3.21 MPam$^{1/2}$).

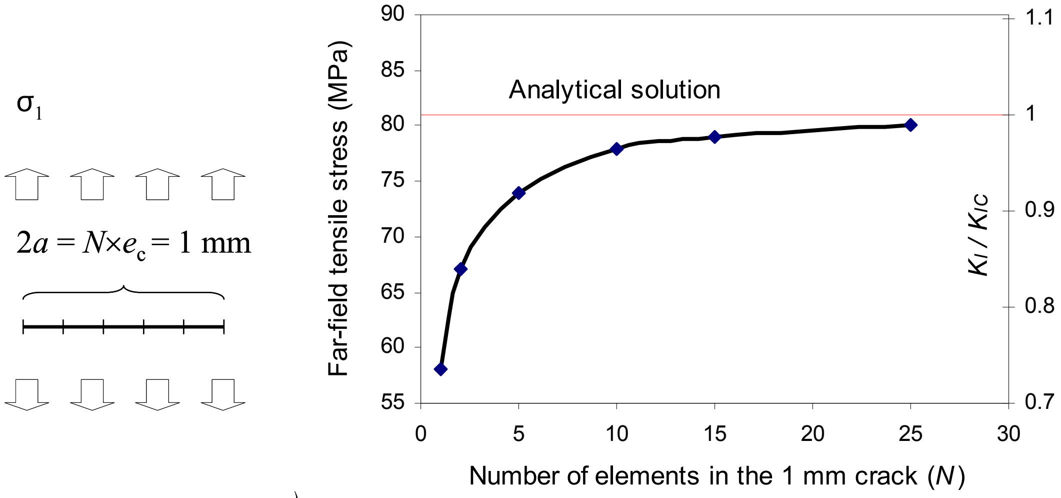

a) *b)*

Figure 8-2. *FRACOD model accuracy. a) Loading configuration; b) far-field stress required for fracture initiation. The element size varies, the crack length is constant.*

Figure 8-2b shows the applied far-field stress required for fracture initiation versus the number of elements along the crack. For example, an approximation of the crack by five elements (e_c = 0.2 mm) yields about an 8.6% error and an approximation by 15 elements (e_c = 0.067 mm) yields about a 2.5% error compared with the analytical solution. A coarse model indicates overestimating of the strain energy release rate (or stress intensity factor) at the crack tip. Comparable results are reported in Shen (1993).

The newly formed cracks in the FRACOD models are defined by two displacement discontinuity elements. The newly formed crack starts to propagate at about 17.3% below the analytically calculated far-field stress.

8.2.3 Model boundaries

Together with the complex microstructure of rocks, the specimen geometry and boundary conditions affect the stress distribution that dictates the failure process. In the previous chapter, numerical rock specimens with finite boundaries were investigated. To evaluate the possible inaccuracy caused by the numerical stress and/or the displacement boundaries, a block model with dimensions 0.125 m × 0.125 m was set up (Fig. 8-3a). Each edge of the block is defined by 20 elements (e_b = 6.25 mm). Calculations are made for different crack lengths, but the crack element size is kept constant (e_c = 0.2 mm).

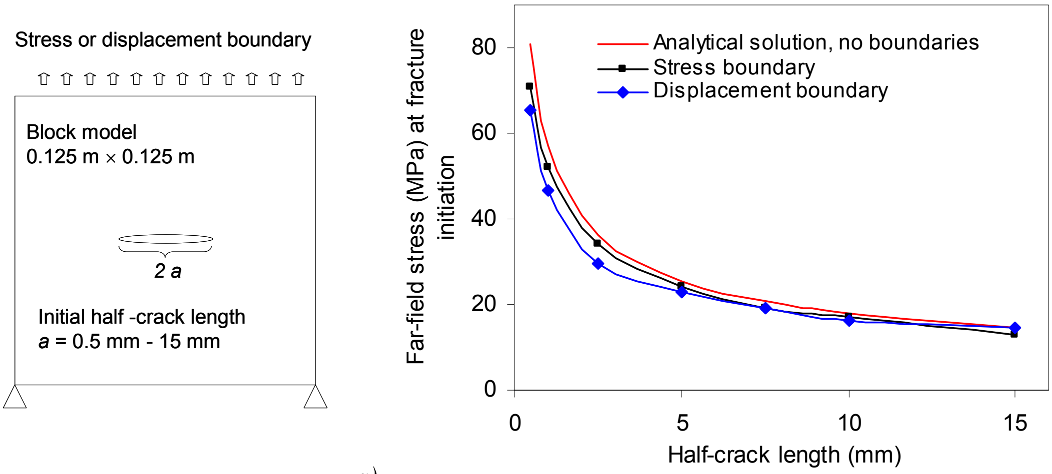

a) *b)*

Figure 8-3. *a) FRACOD block model. b) The initial crack length versus critical applied stress for fracture initiation (K_{IC} = 3.21 MPam$^{1/2}$) for the block model.*

From Fig. 8-3b, it can be seen that the numerical stress boundaries will not introduce a significant difference compared with the infinite analytical case. The slight difference is mainly caused by model discretisation. For the displacement boundary model, horizontal movement at the top and bottom boundaries was prevented (dx = 0) as explained for the rock specimen models presented in Chapter 6. This creates shear stresses at the top and the bottom of the model and might explain somewhat deviating results compared with the stress boundary calculations. From Fig. 8-3b it can also be noted that the failure stress for a crack of 2a = 30 mm is not significantly affected by the finite specimen size (125 m x 125 mm).

It can be concluded that both the stress and displacement boundaries can be used to analyse the critical stress for crack propagation, assuming that the crack tip is not in the vicinity of the model boundary.

8.2.4 Accuracy of the subcritical crack growth approximation

To evaluate the accuracy of the SCG function, a simple problem of crack growth under tension is solved as shown in Fig. 8-4a. The following parameters are used: Far-field stress: $\sigma_x = 0$, $\sigma_y = 10$ MPa; initial crack length: $2a_o = 10$ mm; and fracture toughness: $K_{IC} = 3.8$ MPa $m^{1/2}$. The SCG parameters are as follows: $B_I = 500$ and $n_I = 30$.

Initially, the crack grows slowly and after 6 years it has extended only 2 mm. After this slow-growth phase, the crack velocity increases rapidly. After 6.4 years the crack has exceeded the critical state for unstable fracture propagation ($K_I / K_{IC} \geq 1.0$, when $a > 46$ mm) and will cause failure.

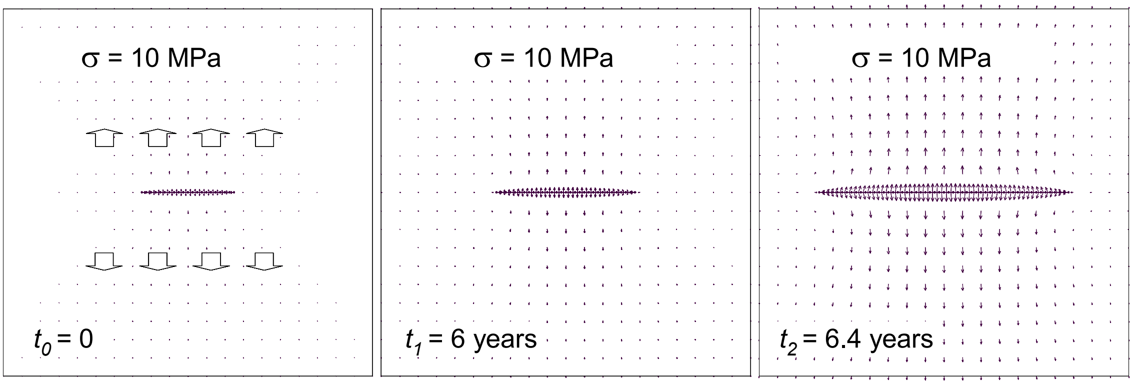

a) *b)* *c)*

Figure 8-4. *Subcritical crack growth in tension according to the FRACOD model. (a) Initial stage (t = 0) with a crack length of 10 mm and a uniaxial tension of 10 MPa. (b) After 6 years the crack has extended by 2 mm. (c) After 6.4 years the crack has reached the state of unstable fracture propagation.*

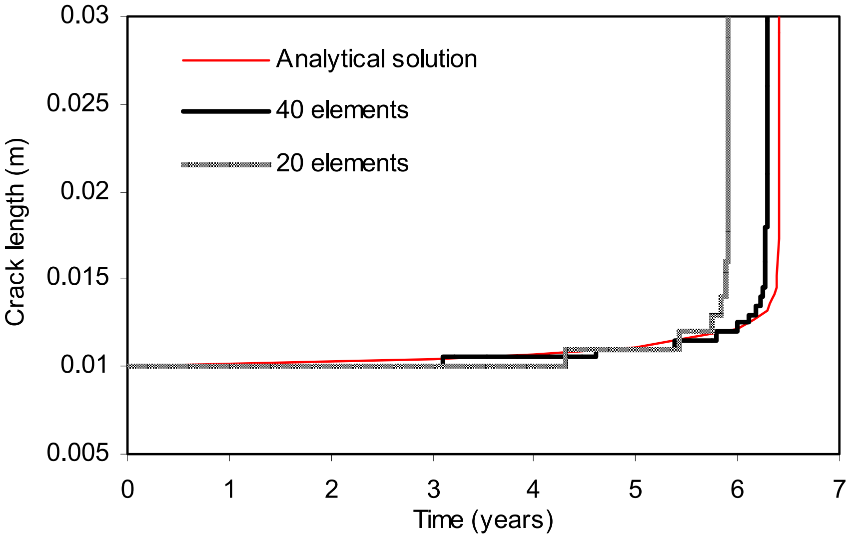

Figure 8-5. *Accuracy of FRACOD to model subcritical crack growth.*

Figure 8-5 presents the modelled crack length at different times. The model is calculated by two approximations, $N = 20$ elements and $N = 40$ elements, respectively. The analytical results using Eq. (3-12) are presented for comparison. The model resolution has a significant effect on the assessed failure time. Minor errors in the initial stress intensity factor at the crack tip lead to a major change of failure time when long time spans are considered. The assigned minimum and maximum time steps also affect the calculated time for SCG and delayed failure, but the effect is not as remarkable as the element size.

8.3 Material parameters and related uncertainties

The inherent rock structure dictates whether the failure process starts or not under a given loading condition. Hence, reproducing a realistic stress distribution of a loaded rock specimen is important for FRACOD modelling. The new crack formation process as modelled by FRACOD is explained in Section 4.4 and some models aiming to investigate the sensitivity of new cracks to the critical applied stress on failure are presented in Section 6.3.

Besides the geometrical factors of the newly formed cracks, the material properties and the boundary conditions (e.g. confining pressure, etc.) also affect the failure process. Due to the large number of parameters that FRACOD uses, a comprehensive sensitivity analysis of all factors including coupled effects would be a major task. The given loading configuration dictates how sensitive the results are to a certain material parameter. Therefore, general conclusions about the sensitivity of results to a certain parameter cannot be given without defining the loading configuration. Sensitivity analyses of FRACOD model results with respect to the material parameters are described in Rinne (2000), Rinne et al. (2003a, 2004) and Shen and Rinne (2007). The following subsections aim to summarize aspects related to newly formed cracks, input parameters and associated uncertainties. It must be stressed that the modelled appearance of the newly formed cracks does not directly represent the spatial distribution of discontinuities of the real rock and it is by no means a universal solution. The modelled size, angle and density of the newly formed cracks represent a summation of many factors and some of them are, at least to some degree, method dependent.

8.3.1 Crack length

Some researchers have indicated that Griffith cracks in rock are approximately equal to the maximum grain diameter (Whittaker et al. 1992). The critical crack length in the presented compression strength test models is in the range of $2a$ = 1-3 mm. This is in agreement with the average grain diameter (1.28 ± 1.61 mm) reported for the Äspö diorite (Backers 2005).

The average tensile strength of the Äspö diorite is about 15.2 MPa (Table 5-1). If we consider a loading configuration as shown in Fig. 6-7a, the critical crack length for tensile failure is about $2a$ = 28 mm (Fig. 6-7b; K_{IC} = 3.21 MPam$^{1/2}$, dry test conditions). This correlates with the large feldspar grain size of the Äspö diorite. Such large grains or other large discontinuities were avoided in the specimens tested. Even if this first approximation does not take into account the effect of the finite specimen size, the tri-dimensionality of real tests, etc., the large size of the theoretical crack indicates that instead of one isolated discontinuity, many small defects (microcracks, grain boundaries, pores, etc.) in the rock matrix may contribute to a build-up in an appropriate stress concentration leading to the failure process. In a linear elastic material, the stress field is undisturbed away from the crack but near the fracture tip the stress distribution is significantly altered (e.g. Figs 6-8 and 6-10). Since cracks are rarely isolated events, we must consider the presence of all kinds of defects including grain boundaries, pores, etc., affecting the stress distribution around the crack tip.

Determination of the initial crack size is of importance, especially for the laboratory test models. Once the unstable failure starts, it leads to a structural breakdown of the specimen, because the stress in a global sense is relatively homogeneously distributed throughout the specimen. In rock volumes with an uneven global stress distribution, for example around a tunnel, the failure starts from sections with the highest stresses and the cracks extend towards areas with less critical stresses until the propagation ceases. The extent of the area where the fracture propagates is usually of interest, such as the excavation damage zone (EDZ) in tunnelling. If the initial crack size is overestimated in the model, the area where the cracks start to propagate is too large, but the failed section is not radically erroneous, because the macro-fracture will not extend outside the critical stress environment. If the initial crack is too small, few propagating cracks express the extent of the critical section. In the APSE project, the effect of element size on fracture pattern was investigated for the pillar experiment (Rinne et al. 2003a). Varying the element size generally yields consistent models, although the fracture pattern is affected. When large rock volumes around tunnels are modelled, pre-existent macro-fractures are usually implemented in the model, because these pre-existent macro-cracks are likely to dominate the failure. The new crack formation might be of less importance, depending on the pre-existent fracture pattern.

8.3.2 Crack angle

The effect of crack angle between the initial crack and the major compressive stress using FRACOD and the Äspö diorite material parameters has been investigated by Rinne (2000). It was indicated that a fracture angle of about 30° to the applied major principal compressive stress is most favourable for fracture propagation. This holds both for uniaxial and biaxial loading conditions ($k = \sigma_{min}/ \sigma_{max} = 0$ and 0.25). Inclinations of about $\alpha = 15\text{-}45°$ produce dilatational wing cracks under low confinement. Fractures having a small (<15°) or large (≥60°) angle to the load require a higher load to initiate fracture propagation and the cracks extend, alternating between Mode I and Mode II failure. Besides the loading configuration, the K_{IIC}/K_{IC} ratio rules whether the failure occurs in Mode I or Mode II.

For the modelled UCS and Triax tests, the newly formed cracks form an angle of about $\alpha = 20°$ from the major principal compressive stress (Eq. 4-20). This angle is not the most critical angle to initiate fracture propagation. It is likely that real rock matrix involves defects and grain boundaries with a more favourable inclination with respect to the major applied load (α about 30°).

A small crack angle (e.g. $\alpha = 20°$, calculated from the major principal compressive stress) in combination with a low number of elements along the crack seems to incorrectly enhance Mode II failure. Models having higher accuracy suggest more stable wing-crack growth prior to crack coalescence and unstable failure in Mode II. The difference in the failure pattern due to model accuracy can be detected by comparing the fracture patterns resulting from a fine-resolution UCS model (Fig. 6-5) with the more rough resolution UCS specimen model (Fig. 6-26).

8.3.3 Crack interactions

As presented by the models in Section 6.3.2, the stress field associated with a crack affects the closely positioned cracks. For the modelled loading configurations, the far-field stress for fracture initiation is reduced when the spacing between the modelled cracks is small with respect to their dimension. The crack distance in the presented UCS and triaxial test models is about 10 mm and the crack length is between 1 mm and 3 mm. According to the sensitivity analyses, the modelled newly formed cracks do not significantly affect each other prior to fracture initiation. The newly formed cracks are, however, defined by only two displacement discontinuity elements to keep the model size reasonable. Due to the low resolution, the length of the newly formed crack is increased by 50% after the first crack tip element has been introduced. The remarkable increase in the crack length affects significantly the stress distribution in the vicinity of the crack. For the presented UCS and Triax models, the introduction of the first crack tip element usually leads to an escalating failure process. Finer discretisation of the newly formed cracks would describe in more detail the stable wing-crack propagation prior to failure.

8.3.4 Heterogeneity of Äspö diorite

The main goal of the intact rock testing was to provide well-documented laboratory studies that can be used for validation of FRACOD models. It was shown that the problem of unpredictable early failure or excessively long test duration for hard rock creep testing can be overcome with SRS testing. A confining pressure of 2 MPa provided a reasonably stable process to examine the time-dependent behaviour using a slow constant axial strain rate (Antikainen 2007).

The heterogeneity of the Äspö diorite was evaluated by analysing the variation in compressive strength test results. In addition to the UCS and Triax tests described in Section 5.2 (Antikainen 2007), similar tests on the Äspö diorite from APSE have been carried out at HUT. These earlier tests are reported by Särkkä and Eloranta (2003) and by Kuula and Eloranta (2003) and they can be found in Staub et al. (2004). UCS tests on rock samples from the APSE site have also been performed at the SP Swedish National Testing and Research Institute (Jacobsson and Bäckström 2005). Results of these studies are compiled in Fig. 8-6.

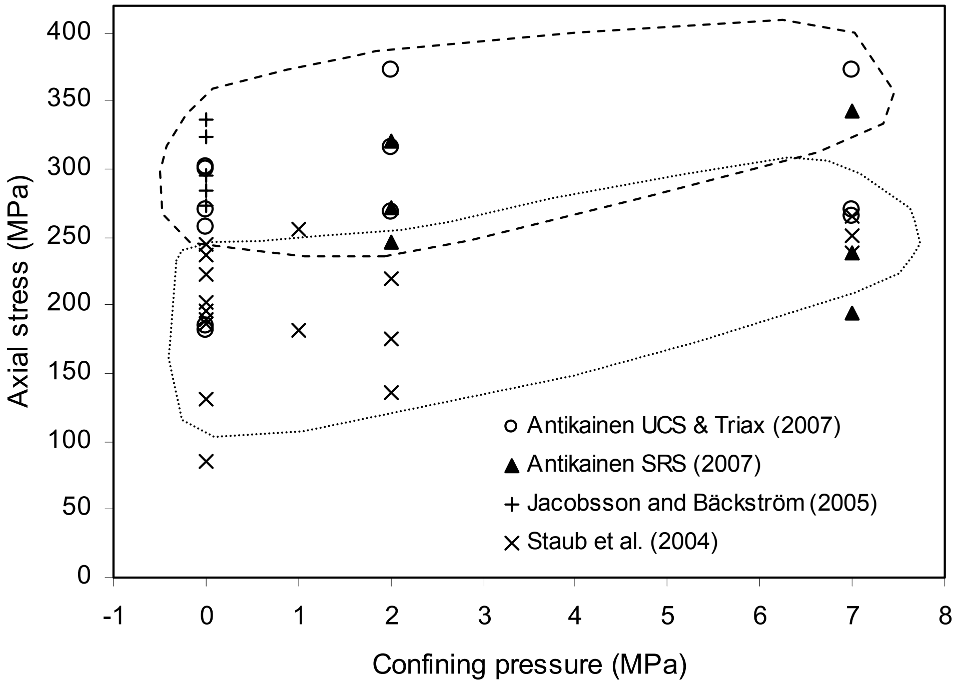

Figure 8-6. *UCS and Triax test on the Äspö diorite, compiled from Staub et al. (2004), Jacobsson and Bäckström (2005) and Antikainen (2007).*

From Fig. 8-6 the large variation in compressive strength test results of rocks from the APSE site can be noted. A large scatter in results is also evident for the test series described in Section 5.2 even if a careful visual inspection was made during the sample selection. The tensile test results range between 11 MPa and 18 MPa and the UCS test results range between 180 and 300 MPa (Table 5-1). The samples presented in Section 5.2 are grouped into domains; the low strength domain (UCS < 250MPa, Samples 1 and 5) and the high strength domain (UCS > 250 MPa, Samples 2, 3, 4 and 6). The grouping in two domains is presented in Fig. 8-6.

As discussed earlier, the Äspö diorite encompasses different varieties of the rock and there is a gradual change between oxidised and unaltered Äspö diorite at the APSE site (Lampinen 2006). The test specimens described in Section 5.2 were not classified into sub-domains, mainly because of uncertainties related to visual classification. To relate the strength to a certain type of

Äspö diorite (or Ävrö granite, see Section 5.1) requires more detailed characterisation of the rock at hand than was made during the sample selection in the current study.

An explanation for the large variation in the compressive strength of rocks from the Oskarshamn including APSE site investigation has been sought in Janson et al. (2007). They investigated connections between the mineral composition and the results from a rock strength test. A clear connection was found between the rock type and the strength. A weak connection was found between the quartz content and the rock strength, i.e. a low strength value corresponds to a low quartz content, but not always. No connection was however found between density and rock strength. Even if the number of tests presented in Table 5-1 is small, the density and Young's modulus seem to correlate clearly with the strength, i.e. high density correlates with low strength and a high Young's modulus correlates with high strength. The inconsistency in the results for the rock density might depend on the fact that analysis by Janson et al. (2007) involves a variety of rock types from a larger rock volume compared with tests reported by Antikainen (2007).

8.3.5 Intact rock parameters

In the FRACOD model, the intact rock material between cracks is assumed to be homogeneous, isotropic and linearly elastic, and the elasticity parameters, Young's modulus, E and Poisson's ratio, ν, dictate the deformation behaviour of the continuum material. The stress level where the new cracks are formed is controlled by the intact rock tensile strength (σ_t), the intact rock friction angle (ϕ_i) and cohesion (c_i), as described in Section 4.4. High strength values obviously mean that a high level of applied stress is required to initiate new cracks. It must be noted that these intact rock strength properties only identify locations and the level of stress where new crack formation occurs. The fracture strength properties (fracture friction angle, fracture cohesion, dilation angle, fracture stiffness and fracture toughness) and the F-criterion control the process leading to structural breakdown.

The results from a number of sensitivity tests with an angled crack ($\alpha = 30°$) under a compressive load indicate that the elastic properties slightly affect the critical applied stress for fracture initiation, but do not affect the mode of fracture propagation (Rinne 2000). The effect of E and ν on stress-strain behaviour and on fracture initiation can be assessed from equations presented in the Section 6.5.6 (e.g. Eq. 6-9). The role of material parameters in the post-peak failure process has not been studied thoroughly.

8.3.6 Properties of newly formed cracks

Uncertainties exist related to the mechanical properties of all small-scale structures of rock matrix (at a millimetre scale or less), because there are no appropriate techniques available yet to directly define these properties. Numerical sensitivity analyses have been performed to evaluate the values of these material parameters. The fracture friction angle (ϕ_f) and fracture cohesion (c_f) define the state of the fracture surface, i.e. they control whether the fracture is in an elastic state or whether it undergoes failure in terms of opening or sliding. When the local stress exceeds the strength of such a crack plane, it will slip or open and its cohesion drops to zero. Failure of the crack surface is a requirement for fracture initiation. Hence, too high fracture strength properties overestimate the far-field stress required to fracture initiation.

Usually, the fracture friction angle and the fracture cohesion of the newly formed cracks are set to be equal or below the respective values of intact rock (ϕ_i and c_i). In practise it must be checked that the crack strength is exceeded below the critical level of applied stress for fracture initiation. When the fracture friction angle and the fracture cohesion are defined experimentally, as might be the case for pre-existent (macro-scale) fractures, they should be used instead of the intact rock values.

8.3.7 Fracture toughness

The critical strain energy release rates (G_{IC} and G_{IIC}), together with the crack geometry and the loading conditions, define whether the fracture propagation takes place or not and the G_{IC} / G_{IIC} ratio determines the mode and direction of fracture propagation according to the F-criterion, as described in Chapter 4. The critical stress energy release rates are calculated from the fracture toughness using the relationship between K and G, as discussed in Section 2.5. The determination of fracture toughness K_{IC} and K_{IIC} are discussed more thoroughly in Section 5.3.1.

Generally, increasing the fracture toughness (K_{IC} or K_{IIC}) increases the required applied load for fracture initiation. The sensitivity of K_{IC} or K_{IIC} on strength depends on the loading configuration and the ratio between K_{IIC} and K_{IC}. An increase of K_{IIC} in biaxial compressive loading conditions increases the threshold value of fracture propagation, while the effect of K_{IC} is less evident. Naturally, the effect of K_{IC} is more pronounced in loading conditions where a Mode I loading component is dominant.

8.3.8 Fracture stiffness

In the FRACOD model, the fracture normal stiffness (K_N) only has an effect on contact cracks, not on open cracks. Fracture shear stiffness (K_S) controls the shear displacements along the crack surface when the crack is in an elastic state. For sliding cracks the friction controls the movement in shear direction and the shear stiffness is not relevant, as presented in Sections 4.2 and 4.3.

Fracture stiffness, particularly normal stiffness, is highly stress-dependent. The higher the normal load applied to a fracture, the higher the stiffness. According to Bandis et al. (1983) fracture stiffness depends on the size of the specimen tested.
Staub et al. (2003) report the normal stiffness for old natural joints at Äspö to be about $K_N = 60$ GPa/m at a normal stress of 23 MPa. Backers (2003) reports the average fracture normal stiffness of about 30000 GPa/m at a loading between 12 and 25 MPa for short specimen-scale fresh cracks.

Low contact stiffness leads to large deformations and low fracture stiffness is reported to reduce the fracture initiation in FRACOD models (Rinne et al. 2004). The effect of K_S and K_N was reported to be less pronounced when the fracture stiffness is more than 5000GPa/m.
Modelled newly formed cracks in this study have a size ($2a$) of about 1 to 3 mm and they appear at a high level of stress. It is assumed that the crack surfaces match almost perfectly for such newly formed cracks; hence the stiffness is assumed to be high and the fracture stiffness suggested by Backers (2003) can be more realistically applied to these fresh cracks compared with the stiffness of old joints reported in Staub et al. (2003).

For shear stiffness, the same high stiffness value is used as applied for the normal stiffness. In practical terms, the shear deformation is restricted for newly formed cracks that have not undergone failure. Fracture sliding controlled by the fracture friction angle will cause shear deformation after failure of the crack plane.

Sensitivity analyses were made using a number of combinations of K_S, K_N and (ϕ_f) in models presented in Chapter 7 ($\phi_f = 20°, 25°, 30°, 35°$ and $49°$; $K_S/K_N = 1/2$ (GPa/m), 200/ 2000

(GPa/m) and 200/30000 (GPa/m)). The fracture cohesion was set to zero for all cases and the cracks slide below the applied load detected critical for SCG or fracture initiation. Similar results were found for calculation with varying combinations of fracture properties. The models presented in Chapter 7 have low fracture stiffness (K_S = 1 GP/m, K_N = 2 GPa/m) and high fracture friction angle (ϕ_f = 49°). For example, recalculation of the model SM3529 using high fracture stiffness (K_S /K_N = 200/ 30 000 GPa/) and low fracture friction angle (ϕ_f = 30°) resulted in almost identical behaviour.

8.3.9 Dilation angle and aperture

In FRACOD, the dilation angle of the newly formed cracks can be specified separately for the shear and the tensile cracks. The Barton-Bandis model has been used to estimate the dilation angle for the Äspö diorite (Shen in Rinne et al. 2003a). This analysis suggested ϕ_d = 2.3° for shear cracks and ϕ_{dil} = 12.1° for tensile cracks. In this thesis, a fracture dilation angle of ϕ_d = 5° was used for both newly formed shear and tensile cracks. Some of the models were calculated using the dilation angle as suggested by the Barton-Bandis model or by using a dilation angle of ϕ_d = 0° for both shear and tensile cracks. The effect of the dilation angle on the failure was not significant for the modelled cases.

FRACOD modelling also takes into account the initial and residual fracture apertures (A_{ini}, A_{res}). In Rutqvist et al. (2007) initial hydraulic fracture aperture of ≤ 10 µm and a residual aperture ≤ 3 µm were suggested for Äspö diorite models. In this study, these parameters have been assumed to be zero or close to zero (1 µm) for newly formed cracks.

9 CONCLUSIONS

The aim of this study was to improve the understanding of brittle failure of rocks, especially the time-dependent behaviour of loaded rocks, by means of laboratory experiments and numerical modelling. The effect of time on the load-bearing capacity of the Äspö diorite has been investigated by slow-rate loading experiments (Strain Rate Stepping (SRS) test). A conceptual model for time-dependent crack growth is developed and incorporated in the fracture mechanics code FRACOD. The failure mechanisms have been investigated both using non-time-dependent and time-dependent models to evaluate mechanical effects including delayed failure and stress relaxation of loaded brittle rock.

There exists a large scatter in the results from laboratory testing, especially concerning the peak strength and the subsequent axial and radial stress-strain response associated with the radial strain controlled loading. However, in general the modelled stress-strain behaviour and the failure process are in good agreement with observations made in the laboratory.

9.1 FRACOD modelling of brittle rock failure

Models describing the rock response to an applied load in short-term strength tests as observed in the laboratory were set up by FRACOD software. It has been shown that the fracture mechanics principles, together with a numerical calculation procedure, can provide a reasonable description of the structural breakdown of a loaded rock specimen. Many general observations from laboratory experiments have been supported by results from FRACOD calculations. The rock failure is described as a process involving new crack formation, fracture initiation and propagation, fracture interaction and coalescence, leading to successive failure of the modelled rock volume, in this case a laboratory specimen. As a result of the calculations, the peak strength, stress-strain response (both axial and lateral) and fracture pattern were reasonably well reproduced.

The ability to model Class II post-peak failure behaviour is a significant validation that the presented method captures the widely observed mechanisms involved in brittle rock failure. By considering the energy balance associated with crack initiation, the stress-strain behaviour can be described by the Griffith locus (Berry 1960). The failure locus, as suggested by the FRACOD model agrees well with the analytical solution for Griffith locus. Class II post-peak stress-strain behaviour in FRACOD model is explained by the Griffith locus.

Simulations of strength tests using the average material parameters of the Äspö diorite suggest that both wing-crack propagation and crack propagation in the shear direction are involved in uniaxial compressive failure. Stable wing-crack propagation takes place prior to unstable specimen failure in shear. When a confining pressure is applied, wing-crack growth is prevented above a certain level of confinement. The shear movement at the fracture surfaces is in order of tens of micrometers prior to the final rupture of the specimen. Significant dilation of developed large fractures in the late post-peak failure stage was detected, especially for those models subjected to low confining pressures. However, large displacement of a detached rock block is not possible to model with the current code.

Model results indicate that instead of one discontinuity (micro-crack, grain boundary, etc.) many small defects may contribute to build up an appropriate stress concentration in a visually intact rock specimen leading to crack initiation and failure of the specimen.

9.2 Time-dependent failure simulations

A conceptual model for time-dependent failure was developed. It utilises the description for Subcritical Crack Growth SCG by Charles (1958) and the energy balance approach to fracture initiation, originally presented by Griffith (1920). The model makes use of a mathematical relation between the applied stress and the velocity of the subcritically growing crack. This correlation has been coupled with fracture mechanics principles to consider the changes in the local stress field associated with the subcritically growing crack. The model enables one to calculate the time-dependent crack length or the time it takes for a crack to grow subcritically before it reaches the critical state for unstable fracture propagation. This concept was successfully implemented in the fracture mechanics software FRACOD. The numerical approximation of the time-dependent failure shows good agreement with the analytical solution. The triaxial compressive strength test models were set up and calibrated to match the failure observed in the laboratory. These models were recalculated using a similar loading history as was applied in the laboratory for the SRS tests. The modelled time to failure (TTF) agrees well with the SRS test results, when considering the resolution of the models and the heterogeneity of the tested material. The simulations also mirror well the underlying failure mechanisms, i.e. when a brittle rock specimen is loaded close to its short-term strength, flaws start to extend slowly. Growing cracks increase the stress concentrations resulting in accelerating crack velocities. When a subcritically growing crack reaches its critical length, fast unstable fracture propagation takes place and an escalating failure occurs.

The time-dependent modelling suggests that only minor SCG takes place in standard triaxial tests, while for the slow-loading rate SRS tests the SCG affects the capacity to sustain a load, i.e. the long-term strength.

The modelled stress-strain curves for the time-dependent failure models agree well with the laboratory data in the elastic region, but overestimate the stresses close to the peak stress. The laboratory tests suggest more inelastic strain and hence more stress relaxation compared with the modelling results. Better model discretisation is needed to be able to simulate more realistically the evolution of inelastic strains. This, however, requires a greater calculation capacity than was used in this study.

Extrapolation of tests to low stresses and long periods of time involves many uncertainties related to the form of equation used, the input parameters and the boundary conditions. The parameters related to this study were defined for a constant temperature, pressure and chemical environment. Even small changes in these conditions influence the parameters, resulting in big changes in the predicted long-term strength. Only a few laboratory tests were available and the results presented are given merely as a method description. A significantly larger database is needed for reliable predictions. However, some indicative conclusions are made based on laboratory results and calculations. The modelled long-term strength is not reduced severely when the applied load is below a certain fraction of the short-term peak strength. When the applied stress is less than 80% of the predicted short-term peak strength, the presented models suggested stable behaviour over 1 million years. An increase in confining pressure increases the required stress/strain level to failure but does not affect the shape of the TTF curve.

10 RECOMMENDATIONS AND FURTHER WORK

10.1 Fundamental research

Because a fracture mechanics approach to modelling rock mass behaviour is based on sound physical processes, it has great potential to shed light on many phenomena related to practical rock engineering. The fracture mechanics principles accurately describe the brittle fracture behaviour on a macro-scale. To improve understanding of micro-scale processes that lead to macro-crack formation, both laboratory investigations and modelling of stress evolution in a polycrystalline rock matrix are needed. X-ray tomography studies of rock specimens under loading might provide valuable information on fracture processes, including SCG.

Mode III loading conditions have received only modest attention in rock mechanics because tearing loading does not seem to be apparent in most rock engineering problems. However, Mode III might occur on a micro-scale when mineral grains rotate and micro-cracks coalesce in the vicinity of the failure plane. Mode III loading and displacements to the adjacent crack must also be considered in 3D modelling. Hence, a deeper understanding of Mode III loading and the corresponding fracture displacement and fracture toughness are study topics of great interest.

10.2 Model and code improvement

In laboratory tests, the stress-strain curve is often non-linear at the start of loading (see Fig. 7-10c). This is usually explained as a consequence of closure of pre-existing cracks. Moreover, fracture stiffness is highly stress dependent. The current code is not capable of modelling this non-linearity in the stress-strain curve because it uses constant fracture stiffness value. To describe more realistically the deformation of fractures under load, a non-linear fracture stiffness-stress relation should be incorporated into FRACOD.

The SCG function presented in this thesis has been tested for tunnel-scale modelling related to the DECOVALEX D-THMC project (Fig. 10-1a). The time-dependent model presents reasonable results at tunnel scale with parameters defined by laboratory tests. The outcomes of EDZ evolution models will be reported in SKI's report series (Rinne et al. 2007a; Rutqvist et al. 2007). Because FRACOD deals with distinct fractures, the changes in hydraulic conductivity due to fracture closing, opening, sliding or propagation can be assessed. Development of this option has started and a preliminary tunnel model has been investigated in the aforementioned D-THMC project (Fig. 10-1b). Further development and verification of the hydraulic function will continue.

The SCG theory is closely related to chemical reactions at the crack tip and the crack velocity correlates with the chemical reaction rates. The model has good potential to be improved to capture the thermo-hydro-mechanical (THM) effects involved in stress corrosion. The SCG model presented in this thesis has been used to study the long-term effects of brine on a stressed rock sample (Rinne et al. 2007b). Subcritical crack growth rates were determined by laboratory experiments for specimens subjected to deionised water and salty water saturated environments. The effect of the chemical environment on uniaxial tensile and compression tests was simulated by adapting crack velocity data obtained from laboratory tests. The effect of brine on the peak strength of the Äspö diorite for different loading rates was clearly captured by the numerical models. The FRACOD software describes so far only the mechanical response to load. The code development to consider the coupled THM effects on rock mass response to load has started in co-operation with CSIRO (Australia).

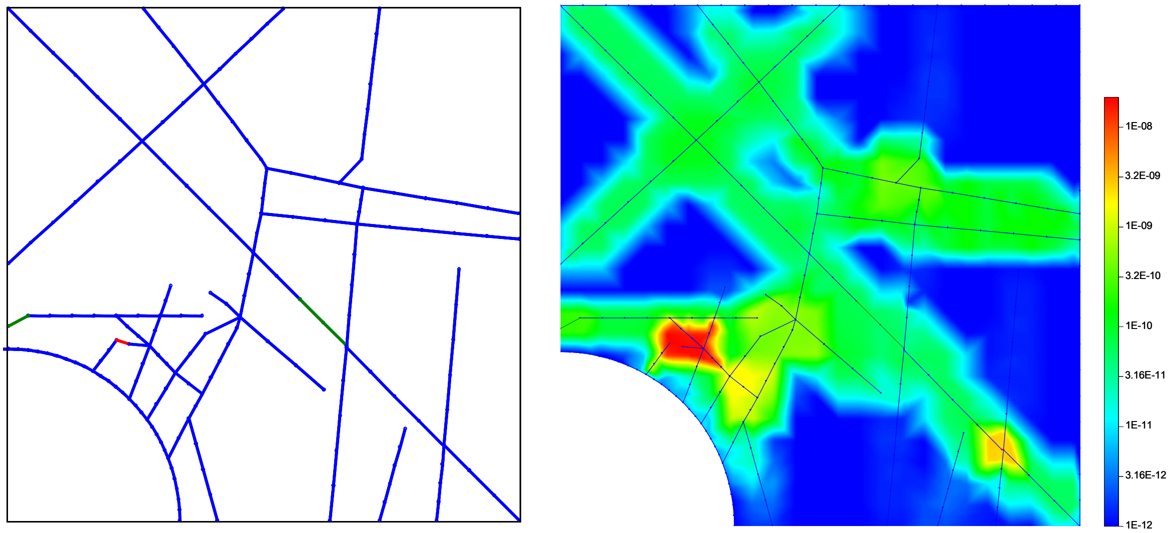

a)

b)

Figure 10-1. *FRACOD tunnel model (3.4 m × 3.4 m); a) fracture pattern after 0.1 million years; b) Predicted hydraulic conductivity (m/s) of rock mass after 0.1 million years (Rinne et al. 2007a).*

From the presented analysis it can be concluded that the numerical inaccuracy can be dealt with by sufficient model discretisation. The models presented in this thesis have been calculated with a standard desktop computer. By increasing the calculation capacity more accurate and more detailed models can be set up. With sufficient calculation capacity the new crack formation process can be described in more detail. Also new features can be added into the model. The code has readiness to deal with multi-region problems, for example, to include mineral grains with varying elastic properties in the model (Shen et al. 2006).

In reality, crack response to load is always a tri-dimensional issue and assumptions have to be made when using two-dimensional models. Code development to improve the method presented in this thesis to deal with tri-dimensionality has been initiated. The preliminary version of FRACOD^{3D} code has demonstrated its ability to model simple cases of tri-dimensional fracture propagations (Shi et al. 2007). For example, Fig. 10-2a shows a circular crack under tension and the profile of the displacement on the crack surface. In Fig. 10-2b, an inclined circular crack under tension after several steps of fracture propagation is presented. The code has established a solid foundation for further developments to create a practical tool for rock engineering.

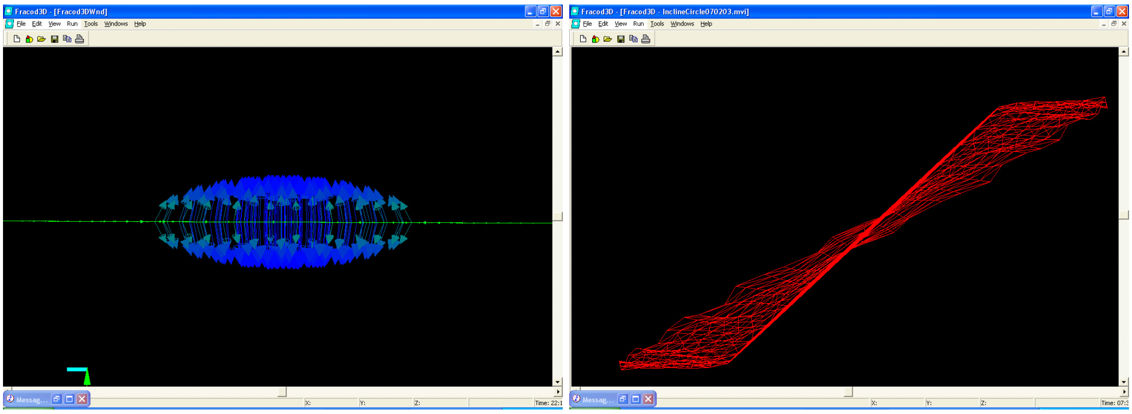

a) *b)*

Figure 10-2. *Tri-dimensional FRACOD3D models. a) Aperture of a crack surface. b) Propagation of an inclined crack under tension (Shi et al. 2007).*

For the 3D simulations, more computing capacity than a desktop computer can offer is required even for relatively simple loading configurations. To take advantage of high-capacity computing hardware some software engineering of FRACOD (both 2D and 3D code versions) is needed. Such plans have been made to be able to further improve the tools required to understand and better predict rock mass behaviour.

11 REFERENCES

Andersson C, 2004. Summary of preparatory work and predictive modelling. Äspö Pillar Stability Experiment. Technical Report R-03-02. The Swedish Nuclear Fuel and Waste Management Co (SKB), Stockholm, Sweden.

Andersson C, 2007. Rock Mass Response to Coupled Mechanical Thermal Loading. Äspö Pillar Stability Experiment. Doctoral Thesis in Soil and Rock Mechanics. Royal Institute of Technology, Stockholm Sweden 2007. TRITA-JOB PHD 1008. ISSN 1650-9501.

Andersson C, Rinne M, Staub I, Wanne T, 2003. The on-going pillar stability experiment at the Äspö Hard Rock Laboratory, Sweden. In the proceedings of GeoProc 2003, International conference on coupled T-H-M-C processes in Geo-systems: Fundamentals, Modelling, Experiments & Applications. Eds. Stephansson O, Hudson J A, Jing L. Stockholm, Sweden, p. 385–390.

Andreev G E, 1995. Brittle failure of rock materials. Test Results and Constitutive models. A. A. Balkema, Rotterdam, Netherlands.

Antikainen J, 2006. Experimental study of creep in hard rock. Preliminary results for the CREEP project. Helsinki University of Technology Rock Engineering. February 2006, p.13.

Antikainen J, 2007. Experimental study of creep in hard rock. Preliminary results for the CREEP project. Helsinki University of Technology Rock Engineering. February 2007, p.14.

Atkinson B K, 1984. Subcritical crack growth in geological materials. J. Geophys. Res., 89: p. 4077-4114.

Atkinson B K, 1987. Fracture Mechanics of Rock. Contributions ed. by Atkinson. Academic Press, Geology Series, London.

Atkinson B K, Meredith P G, 1987. The theory of subcritical crack growth with applications to minerals and rocks. In: Atkinson (1987) Fracture Mechanics of Rock. Academic press, London, p.111-162, p. 477-526.

Backers T, 2003. Determination of Mode I and Mode II Fracture Toughness and Fracture Normal Stiffness of Äspö diorite. Technical Report GFZ Potsdam, 2003. In Staub et al. 2003.

Backers T, 2005. Fracture Toughness Determination and Micromechanics of Rock under Mode I and Mode II Loading. Doctoral Thesis, University of Potsdam, p. 95.

Backers T, 2006. Experimental Determination of Subcritical Crack Growth Parameters. CREEP-project report. GeoFrames, Potsdam Germany. February 2006.

Backers T, Antikainen J, Rinne M, 2006a. Time dependent fracture growth in intact crystalline rock. Laboratory procedures and results. In the proceedings of GeoProc 2006 Editor Xu W. 2nd International conference on coupled T-H-M-C processes in Geo-systems. Nanjng, China, p. 261-266.

Backers T, Stephansson O, Moeck I, Holl H-G, Huenges E, 2006b. Numerical borehole breakout analysis using FRACOD2D. EUROCK 2006-Multiphysics Coupling and Long Term Behaviour in Rock Mechanics. Taylor & Francis Group, London.

Backers T, Stephansson O, 2007. Time Dependent Fracture Growth in Intact Crystalline Rock: New laboratory procedures. Accepted paper to ISRM 11th International Congress on Rock Mechanics, Lisboa Portugal.

Bandis S C, Lumsden A C, Barton N R, 1983. Fundamentals of Rock Joint Deformation. Int. J. Rock Mech. Sci. & Geomech. Abstr. 1983; 20(6): p. 249-268.

Berry J P, 1960. Some kinetic considerations of the Griffith criterion for fracture-I: equations of motion at constant force, J. Mech. Phys. Solids, 8, p. 194-206.

Bieniawski Z T, 1967. Mechanics of brittle fracture of rock. Part I, II and III. Int. J. Rock Mech. Min. Sci. Vol. 4, 3 p. 95-430.

Bobet A, Einstein H, 1998a. Fracture Coalescence in Rock-type Materials under Uniaxial and Biaxial Compression. Int. J. Rock Mech. Min. Sci. 35: p. 863-888.

Bobet A, Einstein H, 1998b. Numerical modeling of fracture coalescence in a model rock material. Int. J. of Fracture 92: p. 221–25.

Charles R J, 1958. Static fatigue of glass. J. Appl. Phys., 1958 (29): p. 1549-1560.

Costin L S, 1987. Time-dependent deformation and failure. In: Atkinson (1987) Fracture Mechanics of Rock. Academic press, London, pp. 167-215.

Cook N G W, 1965. The failure of rock. Int. J. Rock Mech. Min. Sci., Vol. 2, p. 389-403.

Crouch S L, 1976. Solution of plane elasticity problems by the displacement discontinuity method. Int. J. Num. Methods Engng. Vol. (10): p. 301-343.

Crouch S L, Starfield A M, 1983. Boundary element methods in solid mechanics. George Allen and Unwin (Publishers). ISBN 0 04 620010 X.

DECOVALEX–THMC 2004 - 2008. International co-operative project. WWW document. (www.decovalex.com).

Fakhimi A, Fairhurst C, 1994. A model for the time-dependent behaviour of rock. Int. J. Rock Mech. Min. Sci., 31: p. 117-126.

Griffith A A, 1920. The phenomena of rupture and flow in solids. Phil. Trans. Royal Soc. London; Series A, 221, p. 163-198.

Hakala M, Heikkilä, E, 1997. Development of laboratory tests and the stress-strain behaviour of Olkiluoto mica gneiss. Summary report. Posiva Oy, Helsinki. ISBN 951-652-029-4.

Hakala M, Kuula H, Hudson J, 2005. Strength and strain anisotropy of Olkiluoto mica gneiss. Working Report 2005-61. Posiva Oy, Olkiluoto.

Helal H, Homand-Etienne F, Josien J-P, 1988. Validity of uniaxial compression tests for indirect determination of long-term strength of rocks. Int. Journal Min. Geol. Eng. 6, 3: p. 249-257.

Hudson J A, Crouch S L, Fairhurst C, 1972. Soft, stiff and servo-controlled testing machines: a review with references to rock failure. Eng. Geol., 6: p. 155-189.

Hudson J A, Jing L, 2007. Understanding and characterizing of the Excavation Disturbed Zone (EDZ). D-THMC, Task B Phase 2 report. Contributions from modelling teams. Eds. Hudson and Jing. DECOVALEX SKI Report 2007:08.

Hudson J A, Bäckström A, Rutqvist J, Jing L, 2007. Characterising and Modelling the Excavation Damaged Zone (EDZ) in Crystalline Rock in the Context of Radioactive Waste Disposal. D-THMC, Task B Phase 6 report. Contributions from modelling teams. Eds. Hudson, Bäckström, Rutqvist and Jing. DECOVALEX SKI Draft Report November 2007.

Inglis C E, 1913. Stresses in a plate due to the presence of cracks and sharp corners. Trans. Inst. Naval Architects, p. 219-230.

ISRM (1981). Rock Characterization Testing and Monitoring, ISRM Suggested Methods. Brown, E.T. (ed.) Pergamon Press, Oxford.

Irwin G R, 1957. Analysis of stresses and strains near the end of a crack, J. Appl. Mech., 24, p. 361-364.

Jaeger J C, Cook N G W, Zimmerman R W, 2007. Fundamentals of Rock Mechanics. 4th edition. Blackwell Publishing.

Jacobsson L, Bäckström A, 2005. Uniaxial compression test of intact rock specimens at dry condition and at saturation by three different liquids: distilled, saline and formation water. IPR-05-33. The Swedish Nuclear Fuel and Waste Management Co (SKB), Stockholm, Sweden.

Janson T, Ljunggren B, Bergman T, 2007. Modal analyses on rock mechanical specimens. Specimens from borehole KLX03, KLX04, KQ0064G, KQ0065G, KF0066A and KF0069A. P-07-03. The Swedish Nuclear Fuel and Waste Management Co (SKB), Stockholm, Sweden.

Jing L, 2003. A review of techniques, advances and outstanding issues in numerical modelling for rock mechanics and rock engineering. Int. J. Rock Mech. Min. Sci Vol. 40, p. 283-353.

Kemeny J M, 1993. The Micromechanics of deformation and failure in rocks. In: Proc., Int. Symposium on Assessment and Prevention of Failure of phenomena in Rock Engineering, Istanbul, Turkey. A.A. Balkema, Rotterdam, pp. 23-33.

Kemeny J M, 2002. The Time-Dependent Reduction of Sliding Cohesion due to Rock Bridges Along Discontinuities: A Fracture Mechanics Approach. Rock Mech. Rock Engng. (2003) 36 (1), p. 27-38.

Kodama J, Satoh H, Goto T, Yoshida Y, 2001. Creep deformation and creep life of Inada granite under tension. Proceedings of the ISRM regional symposium Eurock 2001. Espoo, Finland 4-7. June 2001, p. 115-120.

Kuula H, Eloranta P, 2003. Mechanical testing on samples from KQ0064G01, KQ0064G07 and KQ0065G01. Helsinki University of Technology October 2003 (Appendix in Staub et al. 2004). The Swedish Nuclear Fuel and Waste Management Co (SKB), Stockholm, Sweden.

KYT. Finnish Research Programme on Nuclear Waste Management: 2006-2010. (www.ydinjatetutkimus.fi).

Lajtai E, Bielus L, 1986. Stress corrosion cracking of Lac du Bonnet Granite in Tension and Compression. Rock Mechanics and Rock Engineering 19: p. 71-87.

Lampinen H, 2006. Detailed geological mapping of the pillar blocks. Äspö Pillar Stability Experiment. Äspö Hard Rock laboratory. IPR-05-024. The Swedish Nuclear Fuel and Waste Management Co (SKB), Stockholm, Sweden.

Lawn B, 1993. Fracture of brittle solids. Second edition. Cambridge University Press, Cambridge.

Lee H-S, Jing L, Shen S, Rinne M, 2003. Modelling brittle fracture and damage between deposition holes by excavation and thermal loading with a stress reconstruction technique. Proceedings of European Commission CLUSTER Conference. Luxembourg, 3-5 November 2003, p. 151-154.

Lee H-S, Rinne M, Shen B, 2006. Modelling discrete fracturing of wall blocks on a deposition hole by THM loading. In the proceedings of GeoProc 2006. Editor Xu W. 2nd International conference on coupled T-H-M-C processes in Geo-systems. Nanjng, China, p. 332-337.

Lockner D, 1993. Room temperature creep in saturated granite. Journal of Geophysical Research, Vol. 98, p. 474-487.

Lockner D, 1998. A generalized law for brittle deformation of Westerley granite. Journal of Geophysical Research, Vol. 103, p. 5107-5123.

Magnor B, 2004. Geological mapping of tunnel TASQ. Äspö Pillar Stability Experiment. Äspö Hard Rock Laboratory. IPR-04-03. The Swedish Nuclear Fuel and Waste Management Co (SKB), Stockholm, Sweden.

Main I G, 2000. A damage mechanics model for power-law creep and earthquake aftershocks and foreshock sequences. Geophys. J. Int., 142, p. 151-161.

Main I G, Sammonds P R, Meredith P G, 1993. Application of a modified Griffith criterion to the evolution of fractal damage during compressional rock failure. Geophys. J. Int. 115, p. 367-380.

Malan D F, Drescher K, 2000. Modelling the post-failure relaxation behaviour of hard rock. Proceedings of 4th North American Rock Mechanics Symposium, Seattle, USA, p. 909-917.

Martin C D, 1997. The effect of cohesion loss and stress path on brittle rock strength. Can. Geotech. J. Vol. 34: p. 698-725.

Martin C D, Chandler N A, 1994.The progressive fracture of Lac du Bonnet granite. Int. J. Rock Mech. Min. Sci. & Geomech. Abstr. 31 (6): p. 643-659.

Napier J A L, 1999. Numerical Studies of time-dependent failure and implications for the prediction of time to failure. Proc. 37th U.S. Rock Mechanics Symposium, Vail, USA, p. 911-917.

Napier J A L, Malan D F, 1997. A Viscoplastic Discontinuum Model of Time-dependent Fracture and Seismicity Effects in Brittle Rock. Int. J Rock Mech. Min. Sci. Vol. 34, No. 7, p. 1075-1089.

Nara Y, Kaneko K, 2003. Dependence of subcritical crack growth in rocks on water vapor pressure. Japan. GeoProc 2003 Proceedings. Eds. Stephansson, Hudson and Jing. Stockholm, Sweden, p. 526-531.

Nara Y, Kaneko K, 2005 a. Study of subcritical crack growth in andesite using the Double Torsion Test. Int. J. Rock Mech. Min. Sci. Vol. 42, p. 521-530.

Nara Y, Kaneko K, 2005 b. Subcritical crack growth in anisotropic rock. Graduate School of Engineering, Hokkaido University, Sapporo 060-8628, Japan. Accepted 31 July 2005. Int. J. Rock Mech. Min. Sci. Vol. 43, p. 437-453.

Ngwenya B T, Main I G, Elphick S C, 2001. A constitutive law for low-temperature creep of water-saturated sandstones. J. Geophys. Res. Vol. 106, p. 21811-21826.

Nguyen T S, Jing L, 2007. Influence of near-field coupled THM phenomena on the performance of a spent fuel repository. D-THMC Task A2 report. Contributions from modelling teams. Ed. Nguyen and Jing. DECOVALEX SKI report. In print. December 2007.

Nguyen T S, 2005. DECOVALEX Task B. Workshop presentation, Kunming, China. www.decovalex.com.

Nordlund E, Li C, Carlsson B, 1999. Mechanical Properties of the Diorite in Äspö HRL. Äspö HRL. Prototype Repository. IPR-99-25. The Swedish Nuclear Fuel and Waste Management Co (SKB), Stockholm, Sweden.

Ojala I, Backers T, Stephansson O, 2004. Experimental determination of subcritical crack growth parameters. Preliminary work plan for the CREEP project. Report A101-1B04-001.

Okubo S, Nishimatsu Y, 1985.Uniaxial Compression Testing Using a Linear Combination of Stress and Strain as the Control Variable. Int. J. Rock Mech. Min. Sci. & Geomech Abstr. Vol 22, No 5, p. 323-330.

Olson J E, 1993. Joint pattern development: Effect of Subcritical Crack Growth and Mechanical Crack Interaction. J. of Geophysical Research, Vol. 98. No. B7, p.12251-12265.

Ouchterlony F, 1988. Suggested methods for determining the fracture toughness of rock. Int. J. Rock Mech. Min. Sci. & Geomech. Abstr.; 25: p. 71-96.

Pollard D, Aydin A, 1988. Progress in understanding jointing over the past century. Bull. Geol. Soc. of America. Vol. 100, p. 1181-1204.

Rao Q, 1998. Determination of Mode II Fracture Toughness for Rock Materials. Luleå University of technology. Licentiate thesis. Sweden.

Rao Q, 1999. Pure shear fracture of brittle rock. A theoretical and laboratory study. Luleå University of technology. Doctoral thesis. Sweden.

Rasilainen K, 2006. The Finnish Research Programme on Nuclear Waste Management (KYT) 2002-2005. Final Report. VTT research notes 2337. ISBN 951-38-6786-2. Technical Research Centre of Finland, Espoo.

Rinne M, 2000. Propagation of rock fractures in the vicinity of a canister hole for spent nuclear fuel. Licentiate Thesis. Royal Institute of Technology, Engineering Geology. Stockholm, Sweden. ISBN 91-7170-617-8.

Rinne M, 2003.Time-dependent fracturing of rock mass and modelling of long-term stability of a repository for spent nuclear fuel. Phases 1, 2 & 3. Research plan 30. Oct. 2003. Fracom ltd, Nick Barton & Associates and Helsinki University of Technology. Fracom ltd, Finland.

Rinne M, 2005. Time-dependent fracturing of rock mass and modelling of EDZ of a repository for spent nuclear fuel (CREEP). Phase 1 (1.1. 2004- 31.1.2005). Annual Project Report. Fracom Ltd, Finland.

Rinne M, 2006. Time-dependent fracturing of rock mass. The Finnish Research Programme on Nuclear Waste Management (KYT) 2002-2005. In Rasilainen (2006).

Rinne M, Shen B, Lee H-S, 2003a. Modelling of fracture stability by FRACOD. Preliminary results. Äspö Pillar Stability Experiment. R-03-05. The Swedish Nuclear Fuel and Waste Management Co (SKB), Stockholm, Sweden.

Rinne M, Shen B, Lee H-S, Jing L, 2003b. Thermo-mechanical simulations of pillar spalling in SKB APSE test by FRACOD. In the proceedings of GeoProc 2003, International conference on coupled T-H-M-C processes in Geo-systems: Fundamentals, Modelling, Experiments & Applications. Editors: Stephansson O, Hudson J A, Jing L. KTH, October 13–15, 2003, Stockholm, Sweden, p. 421-426.

Rinne M, Shen B, Stephansson O, Lee H-S, 2003c. Failure simulation of rock structures. Finnish Symposium on Rock Mechanics. The Finnish National Group of ISRM. Finnish Society of Rock Engineering Geology. In Finnish.

Rinne M, Shen B, Lee H-S, 2004. Modelling of fracture development of APSE by FRACOD. Äspö Pillar Stability Experiment. R-04-04. The Swedish Nuclear Fuel and Waste Management Co (SKB), Stockholm, Sweden.

Rinne M, Jussila P, Eloranta E, 2005. DECOVALEX THMC – Finnish contribution for international modelling project on coupled processes. Finnish Symposium on Rock Mechanics. The Finnish National Group of ISRM. Finnish Society of Rock Engineering Geology. In Finnish.

Rinne M, Shen B, 2005. Understanding of Griffith locus and Class II behaviour. DECOVALEX Task B. Workshop presentation, Kunming, China. www.decovalex.com.

Rinne M, Shen B, Stephansson O, 2006. Numerical analysis of microstructural breakdown of compressed rock samples. EUROCK 2006-Multiphysics Coupling and Long Term Behaviour in Rock Mechanics. Taylor & Francis Group, London. ISBN 0 415 41001 0, p. 701-705.

Rinne M, Shen B, 2007. Numerical simulation of core tests using FRACOD in Understanding and characterizing of the Excavation Disturbed Zone (EDZ). DECOVALEX Task B Phase 2 report. In Hudson and Jing 2007. SKI Report 2007:08. Swedish Nuclear Power Inspectorate, www.ski.se.

Rinne M, Lee H-S, Shen B, Backers T, 2007a. FRACOD modelling of the EDZ evolution and experimental determination of subcritical crack growth parameters. Task B Phase 3 report. Appendix in Rutqvist et al. 2007. DECOVALEX SKI Report series (in print).

Rinne M, Shen B, Backers T, 2007b. Time and chemical effects on rock sample failure. Results from laboratory tests and numerical modelling. Submitted to GeoProc 2008, International conference on coupled T-H-M-C processes in Geo-systems. Polytech Lille, France.

Rutqvist J, Bäckström A, Jing L, Hudson J A, 2007. A benchmark simulation study of coupled THMC processes in the excavation disturbed zone associated with geological nuclear waste repositories. D-THMC, Task B Phase 3 report. Contributions from modelling teams. Eds. Rutqvist, Bäckström, Jing and Hudson. DECOVALEX SKI Draft Report November 2007.

Samuelson E, Dahlin P, Lundberg E, 2007. Boremap mapping of telescopic drilled borehole KFM02B. P-07-102. The Swedish Nuclear Fuel and Waste Management Co (SKB), Stockholm, Sweden.

Schmidtke R H, Lajtai E Z, 1985. The long-term strength of Lac du Bonnet granite. Int. J. Rock Mech. Min. Sci. Vol. 22, p. 461-465.

Shen B, 1993. Mechanics of Fractures and Intervening Bridges in Hard Rocks. Doctoral Thesis. Royal Institute of Technology, Engineering Geology. Stockholm, Sweden.

Shen, B, Stephansson O, 1993a. Modification of the G-criterion of crack propagation in compression. Int. J. of Engineering Fracture Mechanics. 1993;47(2), p. 177-189.

Shen B, Stephansson O, 1993b. Numerical Analysis of Mixed Mode I and Mode II Fracture Propagation. Special issue for the 34th U.S. Symposium of rock mechanics. Int. J. Rock Mech. Min. Sci. 1993, Vol. 30, p. 861-867.

Shen B, Stephansson O, Einstein H, Ghareman B, 1995. Coalescence of open and closed cracks. – A laboratory investigation. J. of Geophys. Res. Vol. 100, p. 5975-5990.

Shen B, Stephansson O, 1996a. Near-field Rock Mechanical Modelling for Nuclear Waste Disposal. Swedish Nuclear Power Inspectorate (SKI). Report 96:17.

Shen B, Stephansson O, 1996b. Modelling of Rock Fracture Propagation for Nuclear Waste Disposal. Swedish Nuclear Power Inspectorate (SKI). Report 96:18.

Shen B, Stephansson O, Rinne M, 2002. Simulation of borehole breakouts using FRACOD2D. Geomechanics in reservoir simulation. Int. Workshop. 5 to 7 Dec. 2001. Oil and Gas Science and Technology. Rev. IFP, Vol. 57, No. 5, p. 579-590.

Shen B, Stephansson O, Rinne M, Lee H-S, Jing L, Röshoff K, 2004a. A fracture propagation code and its applications to nuclear waste disposal. Int. J. Rock Mech. Min. 41 (3), p. 448-449.

Shen B, Stephansson O, Rinne M, H-S Lee, Kobayashi A, 2004b. FRACOD for continuum, discontinuum and fracture modelling of rocks. EUROCK 2004 & 53rd Geomechanics Colloquium. (Schubert ed. CD-ROM).

Shen B, Rinne M, Stephansson O, 2006. FRACOD^{2D}. User's Manual ver 2.21, 2006. Fracom Ltd.

Shen B, Rinne M, 2007. A Fracture Mechanics Code for Modelling Sub-critical Crack Growth and Time Dependency. Proceedings of the 1st Canada-US Rock Mechanics Symposium. Ed. Eberhardt, Stead and Morrison, Vancouver B.C, p. 591-598.

Shi J, Shen B, Rinne M, 2007. Developing 3-dimensional displacement discontinuity code with cracks growth -FRACOD^{3D}. Fracom Ltd, Finnish Funding Agency for Technology and Innovation (Tekes) and Hazama corp., Japan. Project report.

Staub I, Jansson T, Fredriksson A, 2003. Äspö Pillar Stability Experiment, Geology and properties of the rock mass around the experiment volume. IPR-03-02. The Swedish Nuclear Fuel and Waste Management Co (SKB), Stockholm, Sweden.

Staub I, Andersson C, Magnor B, 2004. Äspö Pillar Stability Experiment, Geology and mechanical properties of the rock mass in TASQ. R-04-01. The Swedish Nuclear Fuel and Waste Management Co (SKB), Stockholm, Sweden.

Stephansson O, Shen B, Rinne M, Backers T, Koide K, Nakama S, Ishida T, Moro Y, Amemiya K, 2003. Geomechanical evaluation and analysis of research shafts and galleries in MIU Project, Japan. Proceedings of the 1st Kyoto International Symposium on Underground Environment. Ed. Saito T and Murata S. Kyoto University, Japan.

Szczepanik Z, Milne D, Kostakis K, Eberhardt E, 2003. Long term laboratory strength tests in hard rock. ISRM 2003- Technology roadmap for rock mechanics, South African Institute of Mining and Metallurgy.

Särkkä P, Eloranta P, 2003. Mechanical testing on samples from Äspö HRL, Sweden. Core sample KA3376B01. Helsinki University of Technology, Finland. (Appendix in Staub et al. 2004). The Swedish Nuclear Fuel and Waste Management Co (SKB), Stockholm, Sweden.

Tan X, 1996. Modelling of Drill String Buckling and Tool Indentation in Rock Drilling and Fragmentation. Doctoral Thesis. ISSN 0348-8373 / ISRN 1996:197. Luleå University of Technology, Sweden.

Timonen J, Voutilainen M, Turpeinen T, Jäsberg A, Myllys M, 2006. Studies of pore-space geometry and mineral contents with x-ray tomography. In Rasilainen (2006).

Vásárhelyi B, Bobet A, 2000. Modeling of Crack Initiation, Propagation and Coalescence in Uniaxial Compression. Rock Mech. Rock Engng. 33 (2), p. 119-139.

Wawersik W R, Fairhurst C, 1969. A study of brittle rock fracture in laboratory compression experiments. Int. J. Rock Mech. Min. Sci. & Geomech. Abstr., Vol. 7, p. 561-575.

Whittaker B N, Singh R N, Sun G, 1992. Rock Fracture Mechanics. Principles, Design and Applications. Developments in Geotechnical Engineering, 71. Elsevier, Amsterdam.

Wilkins B J S, 1980. Slow crack growth and delayed failure of granite. Int. J. Rock Mech. Min. Sci. Geomech. Abstr., Vol. 17, p. 365-369.

LIST OF FIGURES

LIST OF TABLES

ISBN 978-951-22-9434-3
ISBN 978-951-22-9435-0 (PDF)
ISSN 1795-2239
ISSN 1795-4584 (PDF)